

KOBELCO TECHNOLOGY REVIEW

No. **36** Nov. 2018

Feature- I : Welding and Joining Technology

Feature- II : Machinery - Industrial Machinery and Compressor Technology

Contents

Feature- I Welding and Joining Technology

Flux-cored Wire for HT610 Class Steel Showing Excellent Toughness after PWHT	1
Dr. Yoshihiko KITAGAWA, Shuji SASAKURA, Masahiro INOMOTO, Hidenori NAKO, Yoshitomi OKAZAKI	
Welding Process Using Special Torch for Reducing Diffusible Hydrogen	7
Naoki MUKAI, Dr. Reiichi SUZUKI	
Robotic Welding System for Shipbuilding	17
Kenji SADAHIRO, Shuhei HONDA, Shunsuke MIYATA, Yutaku SHO, Naoya SAWAGUCHI, Kazuyuki KIKUCHI	
Features of New Robot Controller, CB-type Controller, for ARCMAN™ Welding System	23
Takeshi KOIKE, Shuichi INADA, Atsushi FUKUNAGA, Naoki KIDA, Tsutomu ONE	
New Arc-welding Robots	28
Tatsuji MINATO, Taichi IGARASHI, Motoaki MURAKAMI, Takashi WADA	
Formation of Fine Microstructure in Weld Metal Containing Mn-Ti based Oxides	33
Hidenori NAKO, Yoshitomi OKAZAKI, Dr. Hitoshi HATANO, Ken YAMASHITA, Hideaki TAKAUCHI	
Dissimilar Metal Joining Process "Element Arc Spot Welding"	41
Liang CHEN, Dr. Reiichi SUZUKI	

Feature- II Machinery - Industrial Machinery and Compressor Technology

Tire Uniformity Machine, LIBROTA®	50
Shinichiro IKAI, Yasuhiro MATSUSHITA	
Newly Developed Large Size Continuous Mixer (LCM-IM)	55
Kazuo YAMAGUCHI, Yoshinori KURODA, Toru OKADA	
New Technology for Continuous Casting Machine	59
Tomonori NISHIOKA, Fumiki ASANO, Hiroshi KAWAGUCHI	
Horizontal CIP Apparatus for Food	66
Tomoya MINAMINO	
High-pressure Oil-free Screw Compressor	72
Shugo TAKAKI	
Large Integrally-gear Centrifugal Compressor	77
Keiichi SAEKI, Yasuhisa YAMASHIRO, Toshihisa SHIBATA, Atsushi SANO	
Vertical Type Reciprocating Compressor for LNG Boil Off Gas (BOG) Injection	81
Katsuhiko SEYAMA, Satoshi TEZUKA, Takashi OKUNO, Kenji NAGURA, Naoki AKAMO	

Editor-in-chief :

Toshiya MIYAKE

Associate Editors :

Tomokazu NAKAGAWA

Hiroyuki TAKAMATSU

Editorial Committee :

Nobuyuki FUJITSUNA

Takao HARADA

Hiroshi HASHIMOTO

Koichi HONKE

Atsushi INADA

Haruyuki KONISHI

Yasushi MAEDA

Michihiro MATSUZAKI

Hiroki SANARI

Hiroyuki SHIMIZU

Published by

**Technical Development Group
Kobe Steel, Ltd.**

5-5, Takatsukadai 1-chome,
Nishi-ku, Kobe, HYOGO 651-2271, JAPAN
<http://www.kobelco.co.jp>

Editorial Office: **Shinko Research
Co., Ltd.**

2-4, Wakinohama-Kaigandori 2-chome,
Chuo-ku, Kobe, HYOGO 651-8585,
JAPAN

Fax: +81-78-261-7843

E-mail: rd-office@kobelco.com

© Kobe Steel, Ltd. 2018

Flux-cored Wire for HT610 Class Steel Showing Excellent Toughness after PWHT

Dr. Yoshihiko KITAGAWA*¹, Shuji SASAKURA*¹, Masahiro INOMOTO*², Hidenori NAKO*², Yoshitomi OKAZAKI*²

*¹ Welding Process Department, Technical Center, Welding Business

*² Materials Research Laboratory, Technical Development Group

A detailed study has been conducted to improve notch toughness after post weld heat treatment (PWHT) of weld metal made from flux-cored wires for steel with a tensile strength of 610 MPa class. The microstructure and carbide morphology after PWHT at 620°C were examined. The results have revealed that the size of cementite particles precipitating along the prior austenite grain boundaries significantly affects the toughness. Presumably, this was caused by the cementite precipitates acting as the initiation sites of grain boundary fracture. To refine the cementite precipitates on grain boundaries, it has been found to be effective to adjust the content of C, as well as that of Cr and/or Mo, carbide forming elements. This study has resulted in a weld metal with an optimal composition for HT610 class steel, the weld metal having an excellent strength after PWHT and toughness at -40°C.

Introduction

In the construction of spherical tanks and pressure vessels, etc., post weld heat treatment (hereinafter referred to as "PWHT") is performed to reduce the residual stress introduced by welding, thereby to improve the toughness and fatigue characteristics. With the recent increase in energy demand, these structures are becoming larger and used under higher pressures. Therefore, the strength of the steel adopted has been increasing. Along with the increasing strength of steel, welding materials are also required to have higher strength. In addition, there is a demand for rutile-type flux-cored wire (hereinafter referred to as "FCW") having excellent weldability in all positions in order to facilitate welding works. Conventional rutile-type FCW, however, have not yet been practically applied to the welding of steel with a tensile strength of 610 MPa class (hereinafter referred to as "HT610") or higher, due to the problem that the toughness of the weld metal greatly decreases after PWHT.^{1),2)}

The embrittlement after PWHT in the weld metal of steel having a tensile strength of 550 MPa class or below has been considered to be partially

attributable to the fact that the impurity elements, Nb and V, form carbides and cause precipitation hardening.^{3),4)} In the case of the weld metal for steel of HT610 class or higher, however, a mere reduction of these impurities cannot sufficiently improve the toughness after PWHT, and further toughness improvement by microstructure control has been required.

In the present research, weld metals have been prepared using rutile-type FCW for HT610 class steel to examine the relationship between the toughness and microstructure after PWHT. In addition, the effect that each alloying element has on the microstructure has been examined with the aim of finding the composition of weld metal exhibiting favorable toughness even after PWHT.

1. Experimental method

Prototype FCW, each containing various elements, were made for low-alloy, high-tensile strength steel (HT610 class). **Table 1** shows the composition ranges of the weld metal prototypes in the present research. Pairs of test plates, each 20 mm thick, were arranged with a groove angle of 20° and a root opening of 16 mm to be subjected to multilayer welding under a shielding gas consisting of 80% Ar+20% CO₂ to form weld metals. The test plates were made of JIS G 3106SM490A, and a double layer of buttering was formed on each groove surface with the prototype wire so as to prevent dilution by the base material. The average heat input during welding was 1.2 kJ/mm, the preheating temperature was 90 to 110°C, and the inter-pass temperature was 140 to 160°C. After welding, PWHT was performed at 620°C for 8 hours. Each specimen for the tensile test and Charpy impact test was cut out from the center portion of the respective weld metal to evaluate its strength and toughness. The microstructure of each weld metal was observed by an optical microscope and transmission electron microscope (TEM). The samples for TEM observation were prepared by the extraction replica

Table 1 Chemical composition range of deposited metal used for this study (mass%)

C	Si	Mn	Ni	Cr	Mo	Ti	B	Fe
0.03 - 0.06	0.1 - 0.3	1.3 - 2.0	0.9 - 3.0	0.02 - 0.76	0.2 - 0.6	0.05-0.07	≤0.004	Bal.

method.

2. Decrease in toughness due to PWHT

A weld metal (HT690 class; chemical composition, 0.05%C-0.36%Si-1.90%Mn-0.89%Ni-0.42%Mo-0.07%Ti-0.003%B) has been made using a conventional consumable of Kobe Steel. Its mechanical properties in the as-welded state and after PWHT are shown in Fig. 1. The tensile strength satisfies the criteria of 610 MPa or higher even after the PWHT. The Charpy absorbed energy at -40°C , however, declines greatly to 37J after the PWHT from 90J of the as-welded state. Fig. 2. is the scanning electron micrograph (SEM) of the fracture surface of the specimen subjected to the Charpy impact test (-40°C) after the PWHT. The fracture surface exhibits a number of cracks along the prior austenite grain boundaries, indicating the occurrence of grain boundary fracture, which is considered to have decreased the absorbed energy.

Fig. 3 shows the optical micrographs (OM) and TEM micrographs of the weld metal. The optical micrographs show no significant difference between the as-welded and PWHT states. The TEM micrographs, on the other hand, show that the carbides, both on the grain boundaries and in the grains, have been coarsened by the PWHT. In particular, coarse carbides are precipitated in a continuous manner along the prior austenite grain

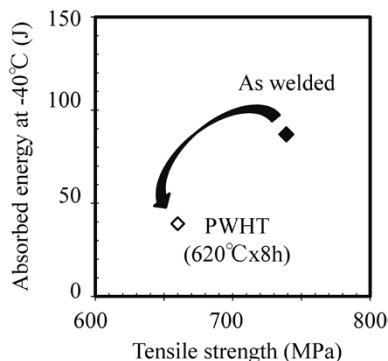


Fig. 1 Mechanical properties of weld metal with conventional wire (HT690 class)

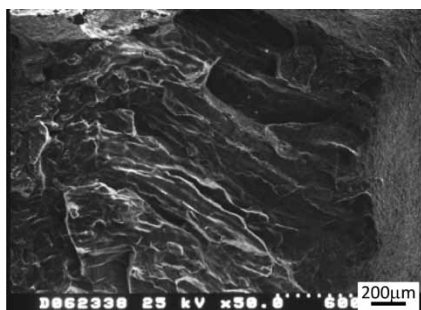


Fig. 2 Fracture surface of Charpy impact test specimen at -40°C after PWHT

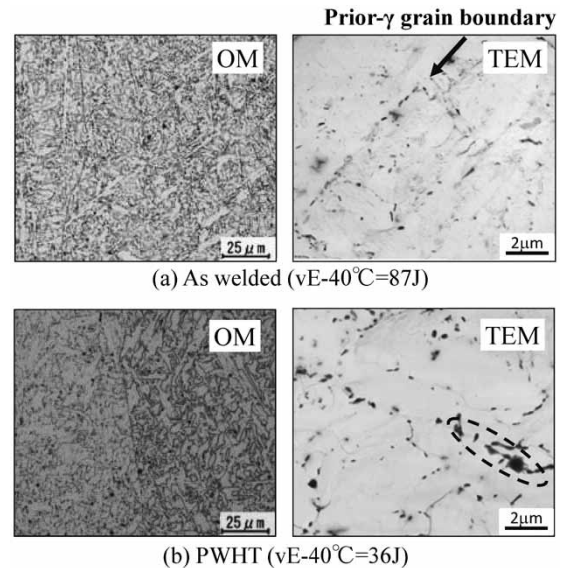


Fig. 3 Microstructures of weld metal

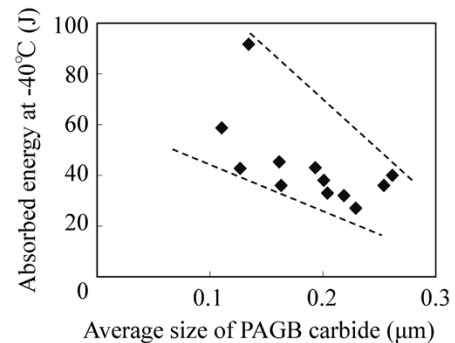


Fig. 4 Relationship between carbides sizes at prior-austenite grain boundary (PAGB) and absorbed energy at -40°C

boundaries, suggesting that they may have acted as the initiation sites of grain boundary fracture and have decreased the toughness.

Fig. 4 shows the relationship between the size of carbides along the prior austenite grain boundaries and the absorbed energy at -40°C for the composition in the range shown in Table 1. The size of carbide particles has been determined as the average value of the equivalent circle diameter corresponding to the area of carbides precipitating along the prior austenite grain boundaries observed in the bright field image of the TEM. As the size of the carbides on the grain boundary increases, the absorbed energy decreases, showing a clear correlation between the size and absorbed energy. It is thought that preventing the coarsening of the carbides on grain boundaries during PWHT is effective in preventing toughness from declining. Hence, we have focused on C and the major carbide forming elements, Mo and Cr, to examine the effect of these elements on the formation of carbide and on toughness.

3. Effect of C, Mo and Cr on carbide formation and toughness after PWHT

3.1 Effect of C

The effect of C was studied. Fig. 5 shows the relationship between the content of C in weld metal and the size of carbides along the prior austenite grain boundaries after the PWHT. The figure shows that the size of carbides tends to increase as the C content increases. An increase in C content simply contributes to an increase in the size of carbide and, hence, the toughness after PWHT is considered to be improved by reducing the content of C. The reduction of C content, however, simultaneously reduces the hardenability of the weld metal, which causes the coarsening of the microstructure. Therefore, its lower limit must also be considered. In the case of the present research, coarse ferrite was formed along the prior austenite grain boundaries when the C content was less than 0.04%, causing a decrease in toughness in the as-welded state. Therefore, a C content of approximately 0.04% is

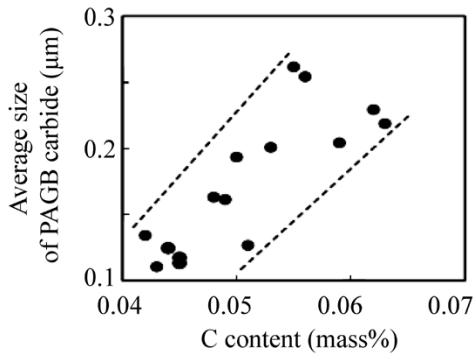


Fig. 5 Relationship between carbon content in weld metal and carbide size at PAGB

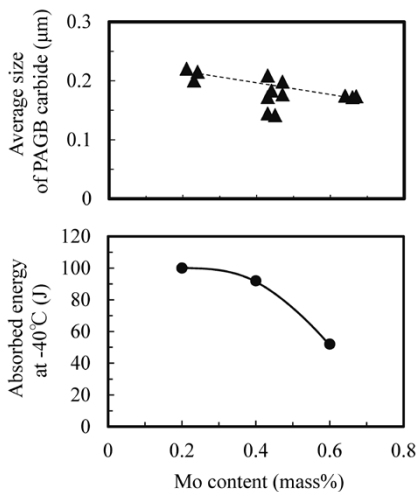


Fig. 6 Relationships among Mo content in weld metal and carbide size at PAGB and absorbed energy at -40°C

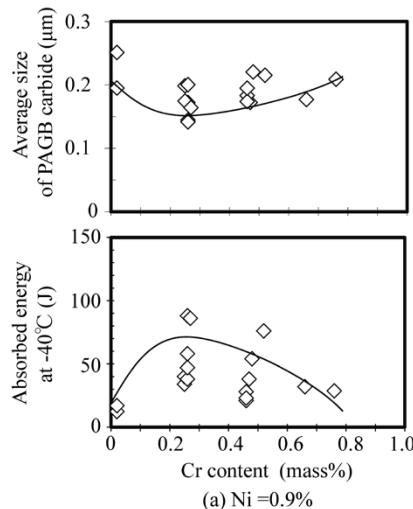
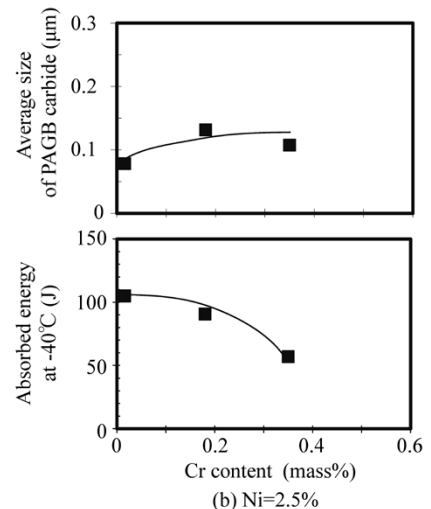


Fig. 8 Relationships among Cr content in weld metal and carbide size at PAGB and absorbed energy at -40°C



considered necessary.

3.2 Effect of Mo

Next, the effect of Mo was examined. Fig. 6 shows the relationships among the content of Mo in the weld metal, the size of carbide on prior austenite grain boundaries after PWHT and the absorbed energy at -40°C. As the Mo content increases, the carbides along the prior austenite grain boundaries become smaller, but the absorbed energy was found to decline. In particular, when the Mo content exceeds 0.4%, there is a significant decline in absorbed energy. Fig. 7 shows the TEM micrographs after the PWHT of the weld metals containing 0.2% and 0.6% of Mo. As the Mo content increases, fine intragranular precipitates are observed to increase. These precipitates are Mo₂C, and the intragranular formation of Mo₂C is considered to suppress the growth of carbides on grain boundaries to some extent. The intragranular precipitation of Mo₂C, however, causes secondary hardening. In other words, the embrittlement due to hardening might have been more pronounced, resulting in the reduction of toughness. In order to secure the

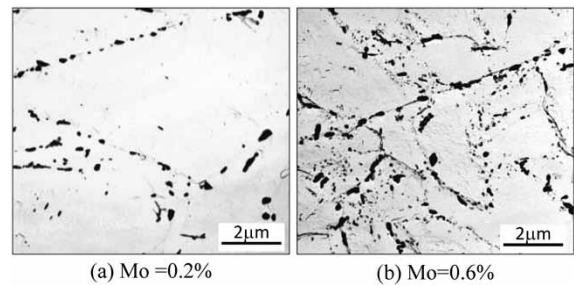


Fig. 7 TEM micrographs of weld metal containing 0.2% Mo and 0.6% Mo

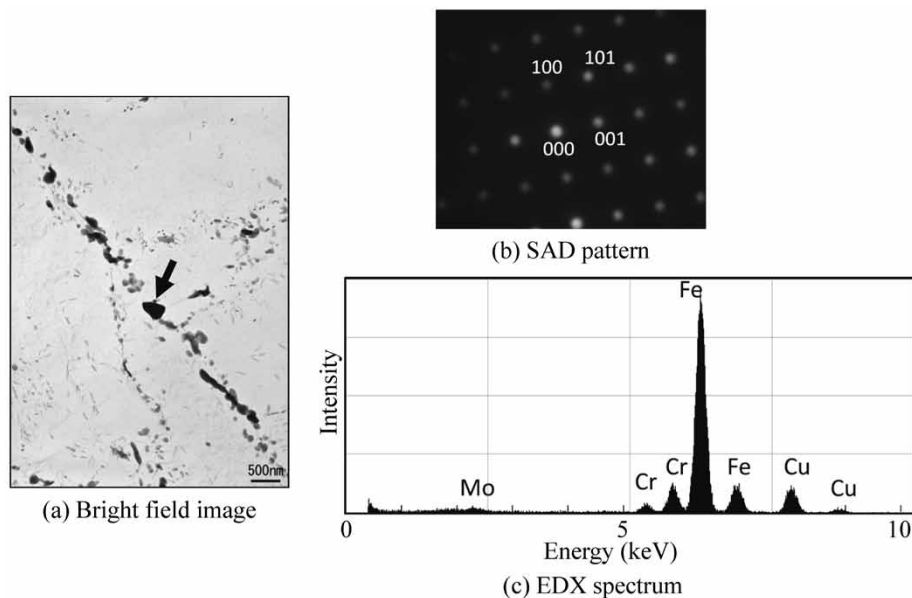


Fig. 9 TEM micrograph of weld metal (0.9%Ni, 0.26%Cr)

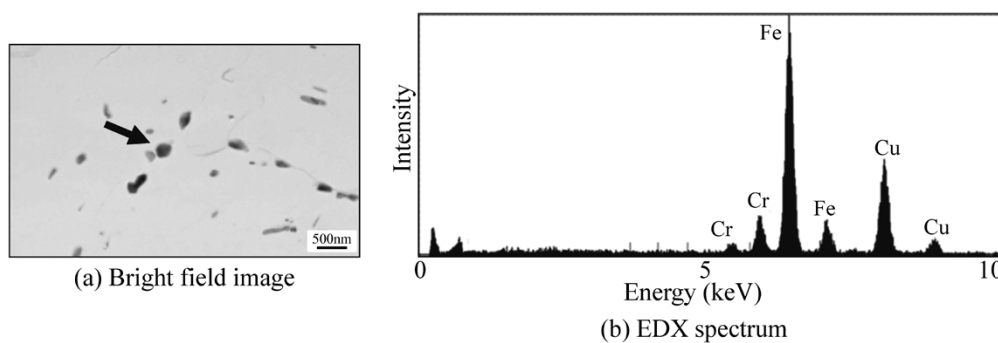


Fig.10 TEM micrograph of weld metal (2.5%Ni, 0.18%Cr)

strength of HT610 class steel while suppressing embrittlement, the amount of added Mo should preferably be set to approximately 0.4%.

3.3 Effect of Cr

Finally, the effect of Cr was studied; the results are as follows. In the case of Cr, different behaviors of carbide precipitation have been observed, depending on the amount of Ni added simultaneously. Fig. 8 shows the relationship of the Cr content in the weld metal, the size of carbide along the prior austenite grain boundaries after PWHT, and the absorbed energy at 40°C for two levels of Ni addition (0.9%, 2.5%). Although the data scatter, the weld metal with Ni content of 0.9% exhibits the minimum carbide size and maximum absorbed energy at a Cr content of approximately 0.25%. On the other hand, in the case of the weld metal containing 2.5% of Ni, the smaller the amount of Cr contained, the smaller the size of carbide becomes, resulting in an increased amount of energy being absorbed.

Fig. 9 shows the TEM micrograph of grain boundary carbides formed in the weld metal containing 0.9% of Ni and 0.26% of Cr. This figure includes the selected area diffraction (SAD) pattern, Fig. 9 (b), and energy dispersive X-ray spectrum (EDX), Fig. 9 (c), both obtained from the coarse carbide shown by the arrow in the bright-field image of Fig. 9 (a). The analysis of the SAD pattern has identified the carbide as cementite, whereas the EDX analysis has confirmed that Cr has dissolved into the cementite, forming a solid solution. It is known that Cr dissolves into cementite to form a solid solution and suppresses the growth of cementite.^{5), 6)} It is considered that the growth of cementite has been suppressed by Cr, which has a low diffusion rate, and, as a result, the size of the cementite has been minimized at a Cr content of approximately 0.25%. Meanwhile, the Cr content exceeding 0.25% is considered to have increased the supply of Cr necessary for the growth of cementite, resulting in the loss of the above suppressing effect and, in turn, increasing the size of cementite.

Fig.10 shows the TEM micrograph of the

grain boundary carbides formed in the weld metal containing 2.5% Ni and 0.18% Cr. The grain boundary carbides in the bright-field image in Fig.10 (a) were formed in an amount smaller than that of the ones in Fig. 9 (a) and are slightly smaller in size. Fig.10 (b) shows the EDX analysis result for the carbide indicated by the arrow in Fig.10 (a). From the fact that Cr is detected as in the case of Fig. 9 (c), this carbide is considered to be cementite with Cr dissolved in the solid solution. In the case of a 2.5% Ni system as well, the dissolved Cr is considered to have the effect of suppressing cementite growth; however, as shown in Fig. 8, the size of the carbides after PWHT increases as the Cr content increases in the 2.5% Ni system. This led to our study on how Cr content affects the amount of cementite formed.

The amount of cementite formed at 620°C in the compositions respectively containing 0.9% and 2.5% of Ni was calculated against the Cr content (Fig.11). The calculation was performed using the

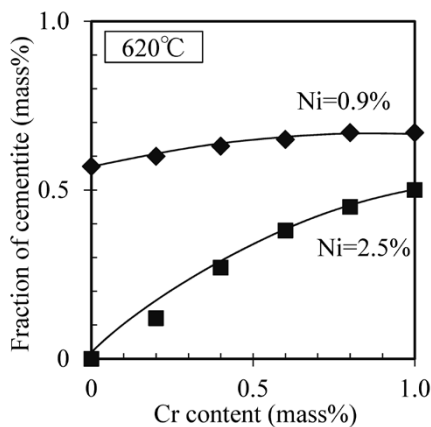


Fig.11 Fraction of cementite at 620°C calculated by Thermo-Calc

thermodynamics calculation software, Thermo-Calc (Thermo-Calc Software AB, Ver. 5, database: TCFE7). When the Ni content is 0.9%, the amount of cementite formed hardly changes with the Cr content; however, when the Ni content is 2.5%, the amount of cementite formed decreases greatly along with the decrease in Cr content. These results indicate that, in the compositions containing 2.5% Ni, the suppression effect on the formation of cementite, an effect due to reduced Cr, had a greater influence on the growth of cementite than did the suppression caused by the addition of Cr, which resulted in the refining of cementite.

4. Mechanical properties of weld metal with optimal composition

From the above, two weld metal systems, containing 0.9% and 2.5% of Ni respectively, have been optimized as shown in Table 2. The mechanical properties of these systems are shown in Fig.12. It has been known that Si and Mn promote the grain boundary segregation of P.^{7,8)} On the basis of this knowledge, and from the consideration of the balance between strength and toughness, the additive amount of Si has been set to 0.15%, and that of Mn to 1.4%. Both of the weld metals of the above composition systems exhibit tensile strengths higher than 610 MPa, a sufficient strength for HT610 class steel, after PWHT at 620°C for 8 hours. Furthermore, the absorbed energy at -40°C after PWHT is greater than that of the conventional material. In particular, the 2.5% Ni-type shows no decline in the value even after PWHT. It should be noted that the weld metals of both compositions exhibit no grain boundary

Table 2 Optimal chemical compositions of weld metal obtained in this study (mass%)

	C	Si	Mn	Ni	Cr	Mo	Ti	B
WM1	0.04	0.16	1.37	0.96	0.42	0.39	0.05	0.002
WM2	0.05	0.15	1.45	2.50	0.02	0.30	0.05	0.002

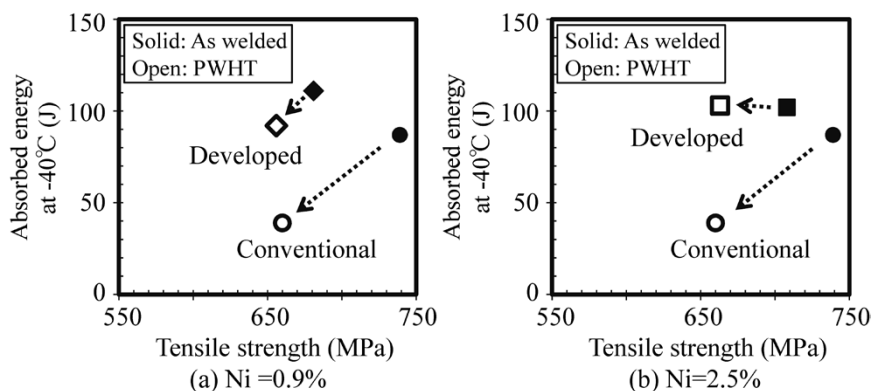


Fig.12 Mechanical properties of weld metal obtained in this study

fracture on the fracture surfaces of the Charpy impact test pieces after PWHT. The 2.5% Ni-type FCW, showing excellent toughness after PWHT, has been commercialized as "TRUSTARC™^{note 1)} DW-A62LSR."

Conclusions

Regarding the weld metal made from FCW for high-tensile strength steel (HT610 class steel), a study was conducted to examine the relationships after PWHT among the microstructure, carbide formation and toughness to pursue the weld metal composition for realizing favorable toughness. The results obtained in the present research are as follows:

- (1) The relationship between the size of carbide on the prior austenite grain boundaries and toughness after PWHT has been examined and, as a result, a clear correlation has been found between them. The decrease in toughness after PWHT is considered to be attributable to the coarsened carbide (cementite) acting as initiation sites of grain boundary fracture.
- (2) The effects of C and of the major carbide forming elements Mo and Cr on carbide formation and toughness were examined. It was found to be desirable to hold the addition of C down to 0.04% and Mo to about 0.4%. It was revealed that the

effect of Cr differed depending on the amount of Ni added.

- (3) The study yielded two weld metal systems, respectively containing 0.9% and 2.5% of Ni, and their mechanical properties after PWHT have been evaluated. Each system exhibits a tensile strength sufficient for HT610 class steel and a toughness more favorable than that of conventional material.
- (4) The 2.5% Ni-type FCW, showing the most excellent toughness after PWHT, has been commercialized as "TRUSTARC™ DW-A62LSR."

References

- 1) K. Suenaga et al. *R&D Kobe Steel Engineering Reports*. 2004. Vol.54, No.2, pp.38-42.
- 2) C. Y. Kang and S. H. Jeong. *Journal of Welding and Joining*. 2014. Vol.32, No.4, pp.75-79.
- 3) K. Hosoi et al. *Quarterly Journal of the Japan Welding Society*. 2016. Vol.34, No.2, pp.81-92.
- 4) T. Suga et al. *IIW Doc. XII-1492-97*. 1997. pp.3-25.
- 5) T. Sakuma. *Bulletin of the Japan Institute of Metals*. 1981, Vol.20, No.4, pp.247-256.
- 6) S. Shimoyama et al. *R&D Kobe Steel Engineering Reports*. 2008. Vol.58, No.1, pp.36-38.
- 7) J. Kameda. *Bulletin of the Japan Institute of Metals*. 1980. Vol.19, No.8, pp.595-603.
- 8) K. Yamanaka. *TETSU-TO-HAGANE*. 1980. Vol.66, No.9, pp.91-98.

^{note 1)} TRUSTARC™ (**TRUSTARC™**) is a registered trademark of Kobe Steel.

Welding Process Using Special Torch for Reducing Diffusible Hydrogen

Naoki MUKAI*¹, Dr. Reiichi SUZUKI*²

*¹ Technical Center, Welding Business

*² Automotive Solution Center, Technical Development Group

Diffusible hydrogen is an important factor in cold cracking, and the lower its content, the better. This study contains a discussion and analysis of the behavior of hydrogen sources in metal active gas (MAG) welding consumables (hereinafter, "welding wires") to devise and develop a new process for reducing diffusible hydrogen, a process for suctioning and discharging the hydrogen sources desorbed from welding wires. Evaluation of the effectiveness of the new process has confirmed that it renders harmless the influence of surface lubricant and moisture absorbed after production and is effective as a new technique for reducing hydrogen. The subject welding wires include both solid wires and flux-cored wires (FCW). In the case of the latter, the moisture initially contained in the flux has been significantly reduced for seamed FCW: the effect, however, is less significant for seamless FCW. The present process has been found to be particularly effective when combined with seamed FCW.

Introduction

In various industries, many structures are becoming increasingly larger in size to meet the demand for higher efficiency. Accordingly, attempts are being made to increase the thickness and tensile strength of steel materials to ensure the strength and rigidity of the members. Such an attempt, however, can increase the cold cracking susceptibility of welding, making it difficult to manage welding works.

The factors causing cold cracking fall roughly into four major categories: (1) factors related to base metal (such as carbon equivalent), (2) factors related to hydrogen, (3) dynamic factors such as residual stress, and (4) the thermal history of welded portions.¹⁾

Several technologies have been known to prevent cold cracking. With regard to the material technology, for example, thermo-mechanical controlled processed (TMCP) high-tensile steel, with suppressed hardening of the microstructure in the heat-affected zone, has been developed and is already in practical use. Other technologies often involve measures against diffusible hydrogen, and the most common technique is to perform preheating and/or postheating to increase the diffusion rate of hydrogen in the steel to facilitate its detachment from the base metal. Managing the

heating involved in preheating and postheating, for example, requires a lot of labor and energy. Moreover, high temperatures can deteriorate the welding work environment, causing serious health and safety issues.

Hence, the focus is centered on the amount of diffusible hydrogen in weld metal. Its reduction can facilitate the management of heating, which is important as a measure for managing the welding work of large structures.

This study relates to the amount of diffusible hydrogen in the weld metals formed by gas metal arc welding (GMAW) and flux-cored arc welding (FCAW) and focuses on the occurrence and entry pathway of moisture and other hydrogen sources in welding wires, a subject area that has not been studied so far. The result has led to the devising of a new welding process for reducing the amount of diffusible hydrogen in weld metals. Furthermore, factors influencing the effectiveness of the process have been studied using an apparatus developed for the practical applications.

1. Past studies on welding methods for reducing diffusible hydrogen

A number of methods have been studied with the aim of reducing diffusible hydrogen in weld metals. Many of these studies are concerned with welding consumables, the oldest being a study on covered electrodes.²⁾ The techniques of hydrogen reduction include technologies for the selection/processing of raw materials to lower the moisture content (hydrated minerals, etc.) in the covered flux and the designing of technologies to reduce the partial pressure of hydrogen in an arc atmosphere by employing a gas forming agent (containing no hydrogen). Regarding the hydrogen reduction technique for flux-cored wires, a production technology that involves wire annealing in the production process has been studied, and there is a report that the amount of diffusible hydrogen was decreased to a level of 0.5 ml/100 g.³⁾

Other than the field of welding consumables, a study was conducted on a welding method for reducing diffusible hydrogen using special shielding gas.⁴⁾ Mixing CF₄ in shielding gas is reported to reduce the amount of diffusible hydrogen in weld

metals. However, there are concerns about the safety of decomposed gas and a problem with deteriorated arc stability. Moreover, CF_4 is a greenhouse gas, and its use is restricted. Thus, there are many problems to be solved before it can be applied.

As described above, research has been conducted on various aspects of the issue to reduce the amount of diffusible hydrogen in weld metals. However, there seem to be no examples of this issue being approached from the aspect of the welding apparatus.

2. Design of process for reducing diffusible hydrogen using special torch

It is obvious that a hydrogen source migrates from a welding consumable to the weld metal via the welding process; however, it is not necessarily clear what route it takes. Hence, the following conjecture has been made:

During welding, the wire between the contact tip and base metal is heated by the Joule heat and arc heat due to the welding current. If a sufficiently high temperature is reached at this time, the hydrogen source is considered to be desorbed from the wire due to thermal energy.⁵⁾ The desorbed gas is carried by the peripheral flow of the shielding gas and transported to the droplet and/or arc generating area. Eventually, it reaches the molten pool, in which hydrogen dissolves into the weld metal. If this conjecture is correct, the amount of hydrogen absorbed into the weld metal should be decreased by somehow discharging from the welding system the hydrogen sources desorbed from the wire along with the surrounding gas, thus decreasing the amount of hydrogen that comes in contact with the droplet and/or molten pool. Hence, a special welding torch has been devised to confirm whether this idea is practical. **Fig. 1** schematically illustrates the special torch. This torch constitutes a double-nozzle torch system comprising an additional nozzle (called a suction nozzle) provided between the contact tip and the shielding nozzle. The negative pressure generated in the space inside the suction nozzle allows the suction of gas near the wire during gas-shielded arc welding.

3. Mechanism of process for reducing diffusible hydrogen and structural design of special torch

In order to verify the effectiveness of the process concept of reducing diffusible hydrogen by using a special torch, and to optimize the structural design of the torch, the temperature of a wire has been calculated and confirmed by an experiment. The

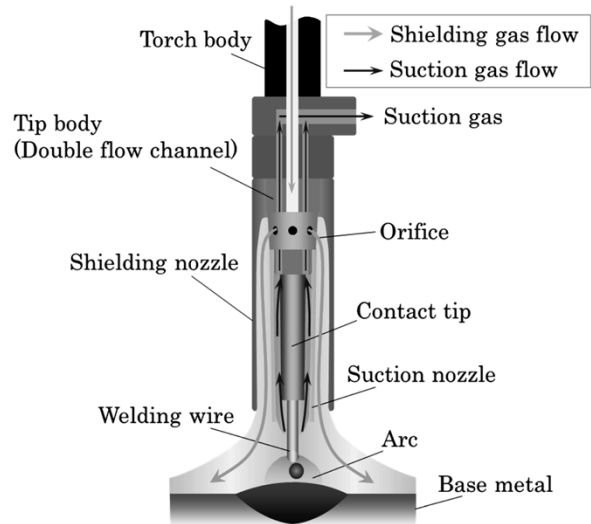


Fig. 1 Schematic illustration of special welding torch

subject welding wire is a flux-cored wire, which contains a larger number of hydrogen sources than a solid wire.

3.1 Estimating temperature distribution of wire during welding

3.1.1 Calculation technique

To verify the hypothesis of hydrogen sources being desorbed due to the temperature rise of the wire during welding, and to optimize the suction position of the gas surrounding the wire (the amount that the suction nozzle protrudes in the longitudinal direction), the temperature distribution of the wire after being fed from contact tip has been estimated.⁶⁾ The calculation has been based on a model simplified as follows:

- (A) It is assumed that the wire is heated only by Joule heat: i.e., heat transfer, radiant heat of arc, etc., are not taken into account.
- (B) It is assumed that the time it takes for the wire protruding from the contact tip to reach the arc region is small enough for thermal conduction to be ignored.
- (C) The Joule heat taken into account is as follows:
 - ① Heat due to the contact resistance between the contact tip and wire, and
 - ② Heat due to the resistance of the welding wire itself.
- (D) For simplicity, the power is assumed to be supplied only from the pointed end of the contact tip, and as for ①, "heat due to the contact resistance," 50% of the heat generated is regarded as the heat input into the wire.

Shimizu et al. have reported that the influence on the temperature rise in wires due to the shunt within the contact tip is small for solid wires without copper plating.⁷⁾ It should be noted that the flux-cored wire that is the object of this calculation is without copper plating. Furthermore, the calculation in this report assumes that 50% of the amount of heat generated by contact resistance is input into the wire; hence, assumption (D) is deemed valid.

On the basis of the above assumptions and assuming the contact tip to be the origin of coordinates, the temperature distribution between the tip and arc is expressed by Equation (1). The second term on the right side indicates the temperature rise due to ① and the third term indicates that due to ②.

$$T(x) = T(0) + \frac{0.5R_c(I)^2}{mv_w c(T(0))} + \int_0^x \frac{R_w(T)I^2}{mv_w c(T)} dx \quad \dots\dots\dots (1)$$

where

- T : wire temperature [°C]
- x : distance in the wire axis direction from the contact tip [m]
- I : welding current [A]
- R_c : contact resistance of wire without copper plating [Ω]
- m : wire mass per unit length [g/m]
- v_w : feed rate of wire [m/s]
- c : specific heat of iron⁸⁾ [J/gK]
- R_w : electrical resistance of wire per unit length [Ω /m].

With regard to the physical properties used for the calculation, the electrical resistance of the wire, R_w , was obtained through the actual measurement of the temperature characteristics in which a flux-cored wire of ϕ 1.2 mm was heated with a constant-current power to measure the voltage drop and temperature of the wire with a fixed length.

The contact resistance of the wire without copper plating, R_c , has been calculated by Equation (2):⁷⁾

$$R_c = 1.2 \times 10^{-2} - 6.0 \times 10^{-5}I + 1.0 \times 10^{-7}I^2 \dots\dots\dots (2)$$

3.1.2 Calculation results

Fig. 2 shows the result of the calculation based on Equation (1) using respective physical properties. The calculation assumes a contact tip-to-work distance of 25 mm; the electric current and wire feed rate, each at two levels of experimental values, have been set to 210A-10.3 m/min and 270A-15.1 m/min, respectively. The wire mass has been set to 6.98 g/m on the basis of the actual measurement. Although there are some differences depending on the electric current, the calculation results show that, in either case, the welding wire reaches 500°C at a position approximately 11 mm from the contact tip and the

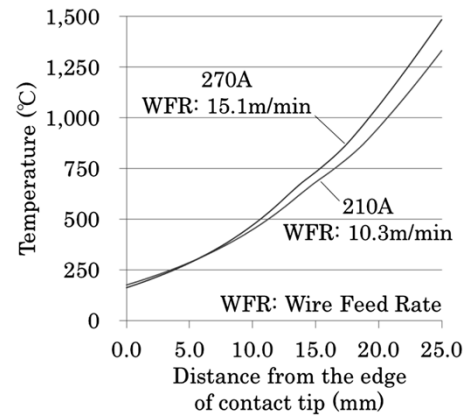


Fig. 2 Calculation results of temperature distribution on welding wire

temperature rises to 1000°C at approximately 20 mm immediately in front of the arc.

3.2 Relationship between welding wire temperature and amount of desorbed gas

3.2.1 Tested material and experimental method

The flux-cored wire was subjected to the desorbed gas analysis under elevating temperature (thermal desorption spectroscopy) to confirm the temperature characteristics of the desorption behavior of hydrogen source when the wire has been heated between the contact tip and the base metal.⁶⁾ The thermal desorption spectroscopy (hereinafter referred to as "TDS") is a technique of heating a sample to raise its temperature in a vacuum container and analyzing the gas desorbed from the sample at each temperature during the heating. The desorbed gas collides with accelerated electrons to be ionized and is separately identified for each mass-to-charge ratio (m/z). The analysis results are obtained as ion electric current, and its magnitude correlates with the desorption amount of the molecule of interest.

In this study, TDS was applied to the flux-cored wire, and the desorption temperature characteristics of water (H₂O: molecular weight, 18) were measured. The heating rate during the analysis was 10°C/min. If the desorption of organic substances and oil could be measured, more accurate behavior would have been obtained. However, the molecular weight of decomposed gas is unknown, and the ion currents, which are the analysis result of the TDS, cannot be used for the absolute comparison of different substances. Hence, this analysis focuses only on water.

Table 1 shows a list of the materials tested. In each case, a prototype seamed flux-cored wire of ϕ 1.2 mm, corresponding to JIS Z 3313 T49J0T1-1,

Table 1 Samples of FCW for TDS

Sample No.	Wire	Applicable standard	Wire diameter (mm)
A	Flux cored wire A	JIS Z 3313 T49J0T1-1 (AWS A5.20 E71T-1C)	1.2
B	Flux cored wire B		
C	Flux cored wire C		

has been selected. For TDS, continuous wires were used, each adjusted to 1.00 g (approximately 140 mm).

3.2.2 Experimental results

The TDS analysis results are shown in Fig. 3. Each sample exhibits a major peak at around 100°C, and subsequently, the desorption amount decreases with increasing temperature. It is shown that the desorption of water is almost completed in the temperature range not exceeding 500°C.

3.3 Design of special torch

The results of the calculation in Section 3.1 show that the temperature of the wire reaches 500°C at a position about 11 mm from the contact tip when the distance between the contact tip and the base metal is 25 mm. Moreover, the results of TDS in Section 3.2 have confirmed that, in the case of the seamed flux-cored wire, the desorption of the moisture contained in the wire is completed before the temperature reaches 500°C.

The above results indicate that, in order to prevent the droplet and molten pool from contacting the hydrogen sources discharged outside the welding wire by evaporation and/or decomposition, it is important to suction the atmospheric gas in the peripheral area of the wire up to a position about 11 mm away from the contact tip. In view of the above, the special torch used for the process of reducing diffusible hydrogen has been designed such that a suction nozzle wraps around the 12 mm portion of the wire protruding from the contact tip (Fig. 4). It should be noted that the heating rate of the wire during welding and the heating rate of TDS are significantly different. Therefore, the actual welding may not exhibit a behavior similar to the one exhibited during the TDS, and experimental verification is required.

On the other hand, the negative pressure is designed to be generated by a mechanism using an ejector. An ejector is a device that can generate negative pressure by the venturi effect, and small general-purpose devices are easily available. Manufacturing plants where welding is performed usually have pipes of compressed air. Hence, there is no problem in obtaining compressed air,

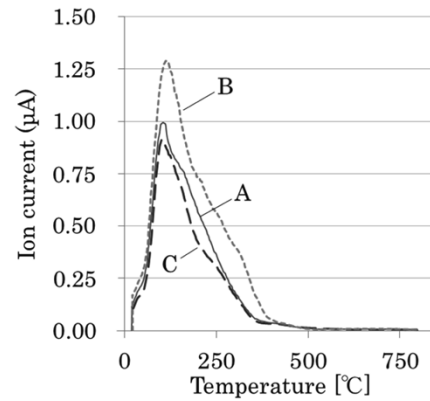


Fig. 3 Analysis results of TDS (H₂O)

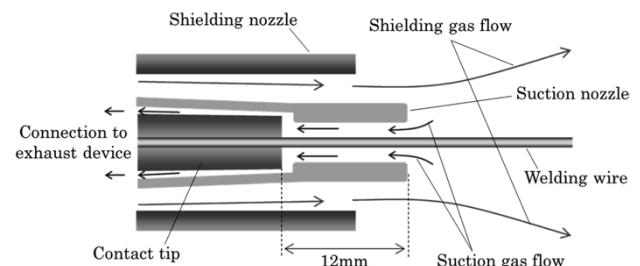


Fig. 4 Structure and dimension of developed welding torch (Longitudinal section)

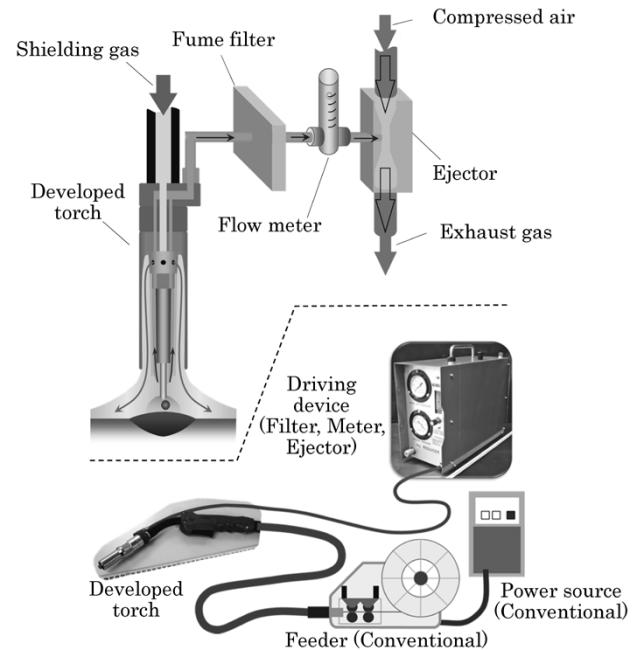


Fig. 5 Prototype torch system

which is advantageous in that the downsizing and simplification of the apparatus are easier than in the cases where pumps are used. A flow meter has also been installed to control the flow of suction gas. In addition, a filter has been installed to protect the flow meter from welding fume (smoke of fine metal). Fig. 5 shows the schematic diagram and appearance of the prototype torch system.

4. Confirmation of effects of special torch developed and influence, on the effects, of factors related to welding wires^{5), 6)}

The newly developed special torch has been used to confirm the effectiveness of the process for reducing diffusible hydrogen.⁶⁾ The sources of diffusible hydrogen contained in the welding wire are classified as shown in **Table 2**.⁵⁾ It has been envisaged that the influence of reducing the amount of diffusible hydrogen depends on these hydrogen sources. Hence, each factor has been verified independently.

4.1 Testing materials and experimental method

4.1.1 Material for testing effectiveness against surface lubricant

Welding wires usually have a surface lubricant applied on their surfaces to secure feedability and prevent the surfaces from rusting. Most lubricants are organic and, therefore, become a hydrogen source. In order to independently confirm the influence of "(a) surface lubricant," which is one of the factors affecting the amount of diffusible hydrogen, prototype solid wires have been prepared with different amounts of lubricant on their surfaces. In the case of solid wires, the influence of factors (b) and (c) is considered to be negligible.

The solid wires used for the test were first subjected to alkaline degreasing. After the degreasing, lubrication oil was applied under various coating conditions so that the wires have different amounts of adhering surface lubricant.

Table 3 shows the list of the wires prepared. The "amount of oil on surface" in the table was determined as follows:

- ① Sampling a certain amount of wire.
- ② Measuring the mass to determine w_1 .
- ③ Degreasing with acetone, followed by drying.
- ④ Remeasuring the mass to determine w_2 .
- ⑤ Calculating the amount of surface oil, A_{sl} , by Equation (3).

$$A_{sl} = \frac{w_1 - w_2}{w_1} \dots\dots\dots (3)$$

4.1.2 Material for testing effectiveness against initial content of moisture in flux

Since flux contained in flux-cored wires is in the form of powder with a large surface area, the adsorption of atmospheric moisture is inevitable, and its complete removal is impossible. For this reason, flux with some amount of moisture is supplied inside welding wires during their production. This moisture becomes a source of diffusible hydrogen.

Prototype flux-cored wires have been made to independently confirm the influence of "(b) the initial moisture content of flux," which is a factor influencing the amount of diffusible hydrogen. Prototype fluxes with a fixed composition have been prepared under different pretreatment conditions such that they have differing moisture content. The term "pretreatment" as herein used includes the presence or absence of material baking, baking conditions, and pulverization methods, such as wet pulverization and dry pulverization.

These fluxes have been used to make flux-cored

Table 2 Welding-wire-related factors affecting the diffusible hydrogen in GMAW and FCAW

Factors of hydrogen source	Solid wire	Seamless flux cored wire	Seamed flux cored wire
(a) Surface lubricant	○	○	○
(b) Initial moisture of flux	-	○	○
(c) Moisture absorbed after production	-	-	○

Note ○: Applicable, ∴ Negligible

Table 3 Trial solid wires for testing the effectiveness of developed welding torch on surface lubricant

Sample No.	Amount of oil on surface (ppm)	Applicable standard	Wire diameter (mm)
a1	0	JIS Z 3312 YGW11 (AWS A5.18 ER70S-G)	1.2
a2	60		
a3	110		
a4	540		

wires, some seamless and others seamed. The amount of surface lubricant has been controlled at low levels (in the range of sample a2 to a3 in Table 3). This is considered to render the effect of factor (a) negligible (reference made to 4.2.1) and, in the case of seamless flux-cored wires, renders the effect of factor (c) negligible. In the case of seamed flux-cored wires, attention has been paid to minimize the influence of factor (c), e.g., storage after production in a low humidity atmosphere. **Table 4** shows the list of wires prepared. The values of "Moisture content of flux" in the table have been measured by Karl Fischer titration (carrier gas, Ar; extraction temperature, 750°C).

4.1.3 Test material for confirming influence of moisture absorbed after production

It is thought that, if unsealed, seamed flux-cored wires absorb moisture from the atmosphere over time. Hence, prototype seamed flux-cored wires have been made to independently confirm the influence of factor (c), "moisture absorbed after production," on the amount of diffusible hydrogen. Each sample has been dried in a constant temperature furnace at 80°C for 3 hours and subsequently moisturized in a thermo-hygrostat at 30°C, 80%RH for a varying time before the amount of diffusible hydrogen has been measured. In this experiment as well, the amount of surface lubricant has been controlled at low levels (in the range of samples a2 to a3 in Table 3), and the influence of factor (a) is considered to be negligible. Moreover, the influence of factor (b) is considered to be sufficiently small, since drying and moisture absorption have been performed after splitting continuous wires. No experiment has been conducted on seamless flux-cored wires, since they are not considered to absorb moisture. Furthermore, this experiment used three-types of flux-cored wires with different applicable standards. The differences are due to the design of the flux compositions. **Table 5** shows a list of sample wires.

The newly developed torch was applied to the prototype wire to be subjected to the mass measurement of diffusible hydrogen. At this time, the flow rate of suction gas was set to 5l/min. A conventional welding torch was also tested to clarify the effectiveness of the process for reducing diffusible hydrogen. Gas chromatography was used for measuring under the conditions of JIS Z 3118, except for the contact-tip-to-work distance. To comply with JIS Z 3118 strictly, the contact-tip-to-work distance should be 20 mm for solid wires; however, the distance was set to 25 mm in this test

Table 4 Trial FCW for testing the effectiveness of developed welding torch on initial moisture of flux

Sample No.	Seam type	Moisture content of flux (ppm)	Applicable standard	Wire diameter (mm)
b1	Seamless	350	JIS Z 3313 T49J0T1-1 (AWS A5.20 E71T-1C)	1.2
b2		1210		
b3	Seamed	350		
b4		1210		

Table 5 Trial seamed FCW for testing the effectiveness of developed welding torch on moisture absorbed after production

Sample No.	Applicable standard	Strength class	Moisture absorption time (hr)	Wire diameter (mm)
c1-1	JIS Z 3313 T49J0T1-1	490 MPa	0	1.2
c1-2			24	
c1-3			288	
c2-1	JIS Z 3313 T556T1-1	550 MPa	0	
c2-2			24	
c2-3			72	
c2-4			232	
c3-1	AWS A5.29 E81T1-K2C	550MPa	0	
c3-2			24	
c3-3			72	
c3-4			232	

Table 6 Welding conditions

Welding current (A)	Arc voltage	Welding speed (mm/min)	Contact tip-to-work distance (mm)	Shielding gas	
				Composition	Flow rate (l/min)
300 (Solid)	Appropriate	350	25	CO ₂	25
270 (FCW)					

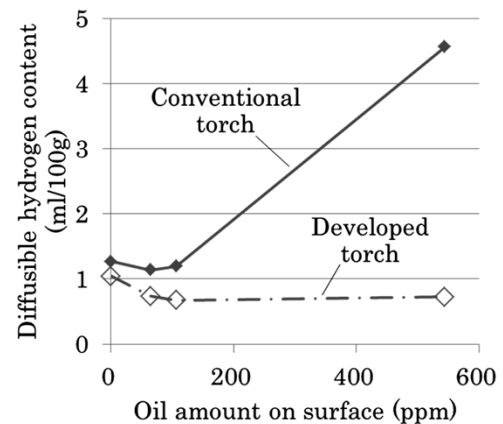


Fig. 6 Effectiveness of developed welding torch on surface lubricant

to be consistent with the tests for flux-cored wires. **Table 6** shows the welding conditions during the sample preparation.

4.2 Experimental results

4.2.1 Effectiveness against surface lubricant

Fig. 6 shows the amounts of diffusible hydrogen measured on the sample wires shown in Table 3 along with the results for the conventional welding torch. The newly developed torch appears to be highly effective against factor (a), rendering it

harmless. In the range where the amount of surface oil is 110ppm or less (samples Nos. a1 to a3 in Table 3), the plots for the newly developed torch are inclined downward to the right. This is considered to be due to measurement errors, and the amount of diffusible hydrogen is regarded as almost constant.

In the case of the conventional welding torch, no significant difference was found in the amount of diffusible hydrogen when the amount of surface oil was 110ppm or less (a1 to a3), and it was found that trace amounts of lubricant had no significant influence.

4.2.2 Effectiveness against initial moisture content of flux

Fig. 7 shows the amounts of diffusible hydrogen measured on the sample wires shown in Table 4 along with the results for the conventional welding torch.

The results of the conventional welding torch will be described first. The seamless flux-cored wire exhibits a large difference in the range of fluctuation for the amount of diffusible hydrogen (circle, solid line), which is due to the initial content of moisture in the flux. On the other hand, the fluctuation range (square, solid line) is relatively small for the seamed flux-cored wire. When the initial content of moisture in the flux is low, the resulting amount of hydrogen becomes higher than that in the seamless wire. Conversely, higher moisture content resulted in a hydrogen amount lower than that of the seamless wire.

Next, the results for the conventional welding torch were compared with those for the newly developed torch (circle, broken line) for the seamless flux-cored wire. The newly developed torch had a minor effect on the reduction of diffusible-hydrogen, as low as 0.5 to 1 ml/100 g. In other words, the reduction effect on the initial moisture content of factor (b) is regarded as small. In the case of the seamed flux-cored wire, on the other hand, the newly developed torch (square, broken line) had a remarkable effect on the reduction of diffusible hydrogen, as much as 3 to 4 ml/100 g. In other words, it is possible to render most initial moisture harmless by using the newly developed torch.

4.2.3 Effectiveness against moisture absorbed after production

Fig. 8 shows the amounts of diffusible hydrogen measured on the wires shown in Table 5 along with the results for the conventional welding torch. In the case of the conventional welding torch, the

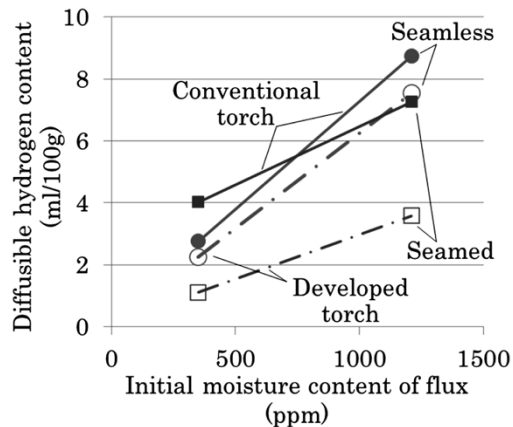


Fig. 7 Effectiveness of developed welding torch on initial moisture of flux

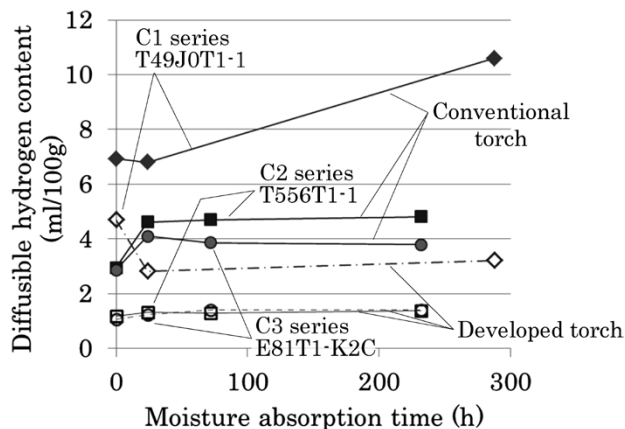


Fig. 8 Effectiveness of developed welding torch on moisture absorbed after production

diffusible hydrogen content tends to increase with the elapsed time of moisture absorption. In the case of the newly developed torch, on the other hand, no such tendency has been observed, and even after the moisture absorption time has elapsed, the diffusible hydrogen content remains almost constant. The moisture absorbed after production is considered to consist mainly of adhering water, which can easily be detached, and it is considered that the newly developed torch works very effectively to reduce diffusible hydrogen.

4.3 Discussion

To confirm the mechanism resulting in the difference in reduction behaviors of diffusible hydrogen in seamed and seamless wires, as described in 4.2.2, TDS tests have been conducted in addition to the ones performed in 3.2.

Two types of wires, seamed flux-cored wire A and a seamless flux-cored wire D, were tested. The seamed flux-cored wire A is as shown in Table 1. The seamless wire D is also a prototype wire of ϕ 1.2 mm corresponding to JIS Z 3313 T49J0T1-1 and

is similar to A. The wire moisture contents measured by Karl Fischer titration (carrier gas, Ar; extraction temperature, 750°C) are 373 ppm for wire A and 48 ppm for wire D.

The sample was adjusted to 1.00 g as described in Section 3.2.1. In addition, in order to evaluate the influence of the wire seam, both seamless and seamed flux-cored wires were sealed by TIG welding at both ends to prevent any disturbance from occurring. The TIG welding at each end was performed by sandwiching with grooved copper plates so that the 10 mm wire end was exposed. The exposed part was put into the TIG arc. **Table 7** lists the samples, and **Fig. 9** shows the results.

Table 7 TDS samples in order to confirm the effect of wire seam

Sample No.	Wire	Wire end sealing
A1	Seamed flux cored wire A	Not applied
A2		Applied
D1	Seamless flux cored wire B	Not applied
D2		Applied

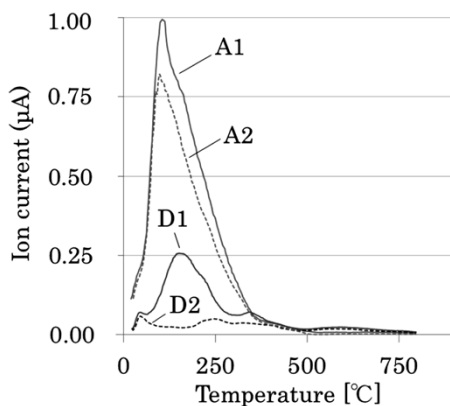


Fig. 9 Analysis results of TDS (H₂O)

A comparison of samples A1 and D1 shows that their main peak appears in the same temperature region, although there is a difference in the amount of water desorbed due to the difference in moisture content. A comparison between samples A1 and A2 shows that the peak height of A2 was decreasing. This is considered to be due to the fact that A2 is fused at each end by the TIG welding in the preliminary treatment.

Comparing D1 and D2, on the other hand, indicates that the peak appearing for D1 disappears for D2. This indicates that, in the case of the seamless wire with both ends sealed, the moisture in the flux continues to be held without being desorbed outside the wire even at a high temperature of 800°C, the upper limit temperature of this test. This result suggests that the moisture and other hydrogen sources inside seamless wires will not be discharged outside the wires even under the influence of Joule heat during welding.

In other words, in the case of the hydrogen reduction process that uses the newly developed torch, the difference in the behavior of diffusible hydrogen reduction due to the presence/absence of a seam can be understood as follows: The seamless flux-cored wire has a sealed structure and, when the wire is Joule-heated between the contact tip and base metal, it cannot release the hydrogen source contained inside, rendering the use of the nozzle to suction gas ineffective. In the case of seamed flux-cored wires, on the other hand, the hydrogen source is easily desorbed outside the wire through the seam and suctioned by the nozzle. As a result, the hydrogen partial pressure in the arc drops efficiently, greatly reducing the diffusible hydrogen. The above difference in behaviors is schematically shown in **Fig. 10**.

It is difficult to directly observe how the moisture

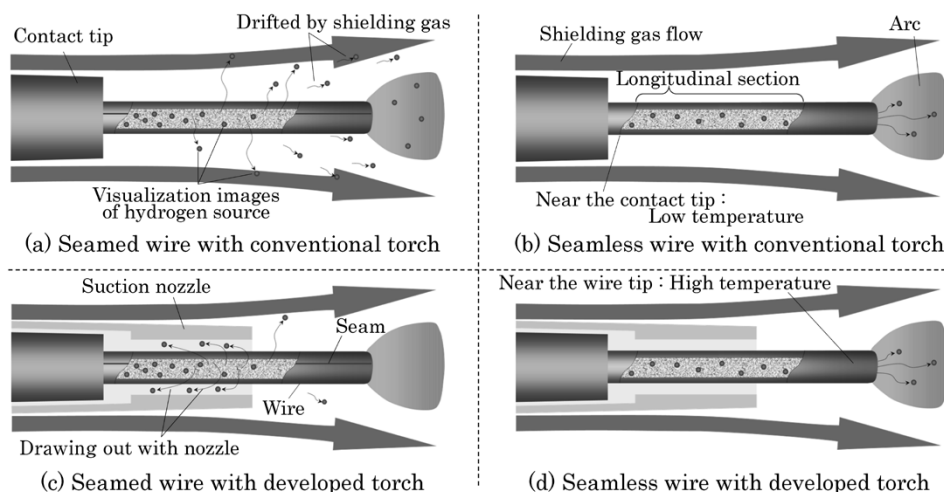


Fig.10 Schematic illustrations of the behavior of moisture in FCW during welding

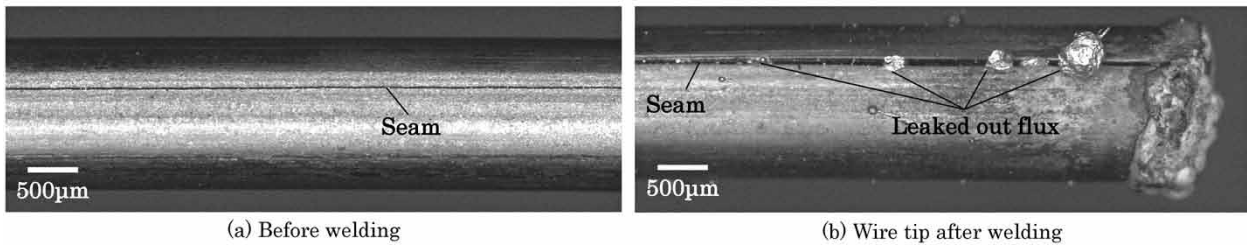


Fig.11 Comparison of wire surface appearance

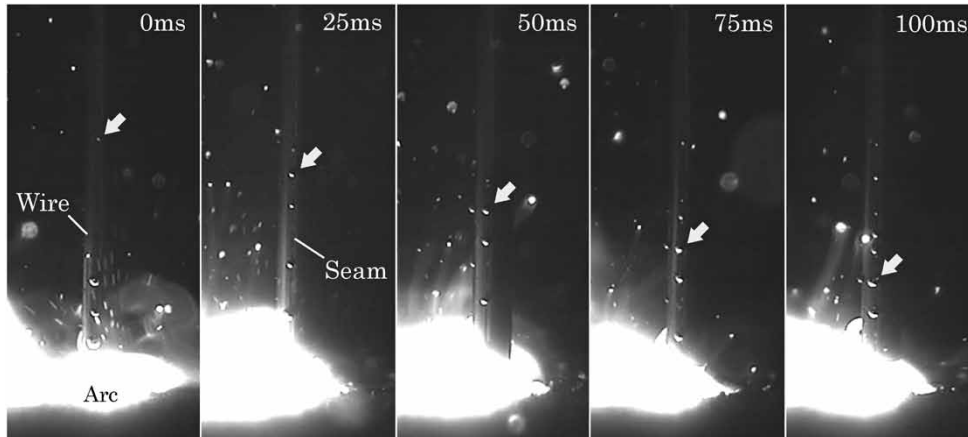


Fig.12 High-speed-video observation result of wire extension part of FCAW

is evaporated and discharged from a seam during welding. There are, however, cases where flux that cannot normally be visually confirmed can be seen leaking from the seam after welding (Fig. 11).⁵⁾ The wire under observation is a wire of ϕ 1.6 mm conforming to AWS A5.20 E71T-14. The wire extension of the same type of wire has been subjected to high-speed imaging during welding as shown in Fig. 12. The arrow in the figure indicates the same droplet descending with the time elapsed. The photos show how a flux-derived droplet that cannot be confirmed by appearance at the top of the image, further from the arc, seeps out from the seam and grows into a larger droplet as it approaches the arc-generating area. The internal pressure of the wire is undoubtedly increased with rising temperature, and it is reasonable to conclude from the above phenomenon that the increased pressure has discharged the moisture from the wire.

5. Possibility of process for reducing diffusible hydrogen

A newly developed special torch that suctions gas near the welding wire has been used to describe the effectiveness of the welding process for reducing the amount of diffusible hydrogen against various welding-wire related factors affecting the amount of diffusible hydrogen. The results obtained so far are summarized in Table 8.

Table 8 Summary of the effectiveness of developed welding torch

Factors of hydrogen source	Solid wire	Seamless flux cored wire	Seamed flux cored wire
(a) Surface lubricant	Total decrease	Total decrease	Total decrease
(b) Initial moisture of flux	-	Slight decrease	Great decrease
(c) Absorbed moisture after production	-	-	Total decrease

The process using the newly developed torch works very effectively against factor (a) and factor (c), rendering these factors harmless. For factor (b), no sufficient effect has been obtained in the case of seamless flux-cored wire. In the case of seamed flux-cored wire, the influence of the initial moisture content of the flux was greatly reduced. This, therefore, verifies the validity of the design reflecting the estimation of the wire temperature distribution during welding and that of the knowledge obtained from the desorption behavior analysis of the hydrogen source.

As described above, it has been shown that the combination of the newly developed torch and seamed flux-cored wire enables welding while rendering harmless many of the sources of diffusible hydrogen arising from welding consumables. In general, the diffusible hydrogen content in weld metal caused by the welding wire must be left to the manufacturers of welding consumables. However, by combining the newly developed torch with seamed flux-cored wires, it is possible that a user

can dominantly control diffusible hydrogen, and the applicability of such a combination is expected to expand. For the manufacturers of welding consumables, there is the possibility that the degree of freedom for flux design will increase, enabling the development of consumables that can produce weld metal with high mechanical performance, less spatter generation, and favorable usability on position welding for thick, high-tensile steel plates.

It should be noted that this technique can also render harmless the influence of surface lubricant in solid wires and seamless flux-cored wires, which can be an effective means for reducing hydrogen.

Conclusions

① A process for reducing diffusible hydrogen has been developed using a special torch that enables welding work to be performed with the suction of gas near wires. ② The temperature distribution of a wire during welding and the results of the analysis of the behavior of hydrogen desorption from the wire have been reflected in the structure design of the special torch. Experimental results have verified the validity of the design. ③ Although the newly developed torch can achieve the reduction of diffusible hydrogen regardless of the type of wire, it is particularly effective for seamed flux-cored wires. ④ It has been confirmed

that the sources of diffusible hydrogen in a wire are desorbed from inside or from the surface as the temperature between the contact tip and the melt/arc generation point rises, transported by shielding gas, and enter into the droplet and molten pool.

We will continue our efforts to demonstrate the possibility of applying this process to reduce the construction management (thermal management) of large structures. It is expected that this process can provide a solution in the field of welding work where thermal management seems to be causing problems.

References

- 1) T. Kasuya. Journal of the Japan Welding Society. 2015, Vol.84, No.1, pp.45-50.
- 2) T. Godai et al. Journal of the Japan Welding Society. 1976, Vol.45, No.7, pp.14-20.
- 3) T. Kasuya et al. Preprints of the National Meeting of JWS. 2009, Vol.84, pp.311-312.
- 4) S. Fiore et al. 2012, IIW Doc.XII-2103-12.
- 5) N. Mukai et al. Quarterly Journal of the Japan Welding Society. 2017, Vol.35, No.2, pp.102-109.
- 6) N. Mukai et al. Quarterly Journal of the Japan Welding Society. "Research and Development on the Welding Process for Reducing Diffusible Hydrogen" (posted, being peer reviewed).
- 7) H. Shimizu et al. Quarterly Journal of the Japan Welding Society. 2005, Vol.23, No.1, p.25-36.
- 8) The Japan Institute of Metals and Materials. Metal Data Book (4th Edition), Maruzen 2004, p.14.

Robotic Welding System for Shipbuilding

Kenji SADAHIRO*¹, Shuhei HONDA*¹, Shunsuke MIYATA*¹, Yutaku SHO*¹, Naoya SAWAGUCHI*², Kazuyuki KIKUCHI*³

*¹ Welding System Department, Technical Center, Welding Business

*² Welding Process Department, Technical Center, Welding Business

*³ Welding Process Department, Technical Center, Welding Business (currently KOBELCO WELDING OF EUROPE B.V.)

As a world-leading welding solution company, Kobe Steel began working on the automation of shipbuilding. A robotic welding system has been developed to be applied to the assembling processes in shipyards. The system includes a robot controller compatible with the small robot that enters hull blocks, a robot carrier for moving within blocks, and robot-program-preparation software allowing offline teaching using 3D models. This paper introduces our robotic welding system offering welding solutions, which integrates all the elements, including the development of optimum welding wires and welding techniques such as gap filling.

Introduction

Kobe Steel, a world-leading welding solution company, is promoting efforts to automate shipbuilding. Like other industries, the shipbuilding industry requires efficiency improvement, including multi-skill development and labor saving, due to the shortage and aging of welders. The lack of skilled workers is increasingly being felt.

This paper introduces a robotic welding system newly developed for ship assembly to improve productivity.

1. Advantage of robotic welding system for assembly

1.1 Robotic welding system

Large ships are built by a method called block building.¹⁾ A shipyard has a block assembly shop, in which blocks of the partial hull are made through the steps of cutting, processing, assembling, etc. These blocks are eventually connected in a dock or on a bench to build a ship (Fig. 1, Fig. 2).

In order to make these blocks, a robotic welding system has been developed with the functions necessary for the assembling process.

In order to perform welding in a block, a robot must be installed in its space surrounded by other parts. The robot must be placed in a limited space, and the welding operation must be performed there smoothly. The robot must be a small one optimized for this purpose (Fig. 3).

The robot body is mounted on a compact, lightweight robot carrier designed for transportation, and in this state, it is suspended from a crane and moved from one block to another.

When the robot carrier is lowered inside a block, the robot is fixed in position by an automatic positioning device. Then the target robot program is selected to start welding (Fig. 4).

Kobe Steel has developed a controller for such welding robots by exploiting its strengths, such as arc sensor technology enabling the tracking of thermally deformed welding surfaces, and vibration control technology. The newly developed controller is a dramatically improved version of

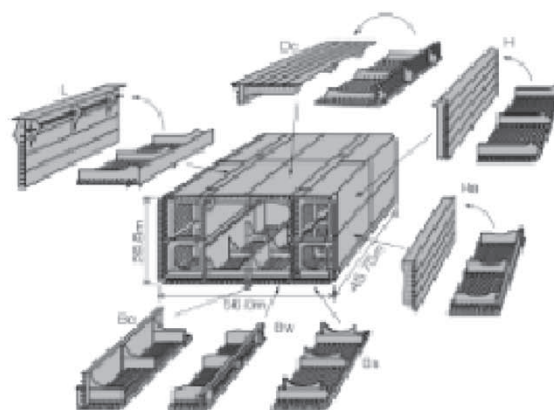


Fig. 1 Hull structure

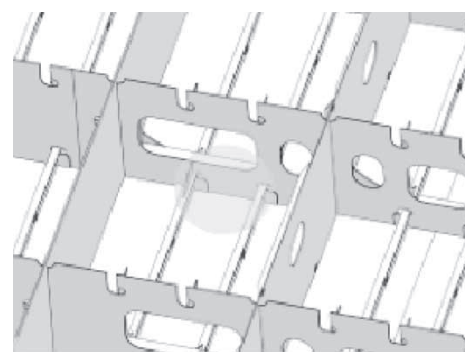


Fig. 2 Welding targets



Fig. 3 Small size welding robot

the conventional CB controller, in terms of (1) upgraded performance, (2) upgraded function, and (3) simplification, taking into consideration safety, maintenance, and system construction.

1.2 Locations where robot applies

A welding robot performs welding at locations between longitudinal elements and transverse elements between the two sides of a hull. Fig. 5 shows the joints that are the targets of robotic welding.

1.3 Teaching software (SMART TEACHING™ note 1)

During the assembling stage, many members with similar linear shapes are arranged in the parallel part; however, it is not efficient to teach robots online using a real machine because the sizes of members vary.

Designing based on 3D models has been used in various fields.²⁾ In the field of shipbuilding it was used early on, as a large number of parts were involved, and 3D design was useful in checking such details as the placement of the parts.

Hence, Kobe Steel has developed an offline teaching system, "SMART TEACHING™," in which 3D models of shipbuilding blocks are used for



Fig. 4 Application of welding robot to ship assembly

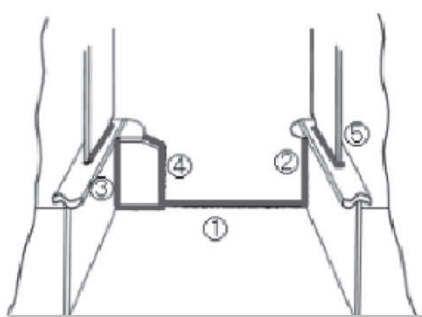


Fig. 5 Robotically welded joints

note 1) SMART TEACHING is a registered trademark of Kobe Steel (No. 05645545).

teaching robots.

1) Reading of 3D model data

The 3D models used for this system are compatible with the general-purpose data format (STEP format). Thanks to this, it is possible to read data from various CADs without depending on any one specific CAD.

2) Automatic extraction of welding lines in blocks

The general-purpose format carries no information unique to a specific CAD (e.g., welding information). Hence, the graphic information included in the model shapes has been used to identify the shapes of the members constituting each shipbuilding block so that the intersections between the members are recognized as the positional information of welded joints. For example, it recognizes horizontal fillet joints where transverse elements and shell plates intersect and vertical fillet joints where longitudinal elements and collar plates intersect.

These coordinate data and the data on member shapes are collected and extracted as welding information data (Fig. 6).

3) Preparation of robot teaching program

The welding information data has been used to recognize the start/end positions of welding lines and to determine the robot motion to perform the welding. Then the motion corresponding to the member shapes, such as sensing, and the welding conditions corresponding to the member shapes and welding position were assigned to prepare the robot teaching program (Fig. 7).

The position matching between the instruction program and the actual work pieces (calibration) is not done by software, but by the positioning device on the robot carrier. Once the teaching program is sent to each robot, welding can begin.

1.4 Welding work

Among the welding stages of shipbuilding, the

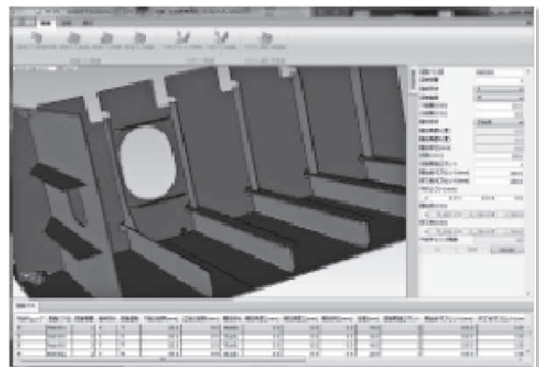


Fig. 6 Software to detect welding lines

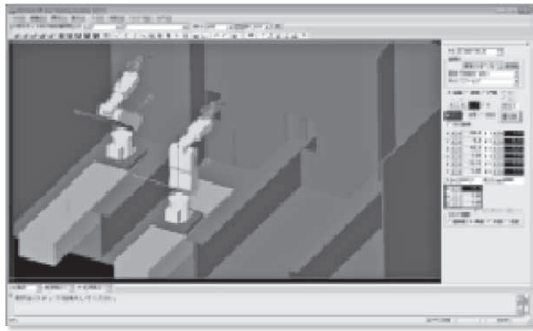


Fig. 7 Robot teaching simulation

Table 1 Wire Evaluation

Welding position	Evaluation item	Wire	
		DW-100	DW-100V
Vertical upward	Bead appearance	○	◎
	Welding speed	○	◎
	Gap tolerance	○	◎
Horizontal fillet	Bead appearance	◎	△
	Welding speed	○	○
	Boxing weld	○	△

*1) Wire evaluation ◎ : excellent ○ : good △ : normal

assembly stage occupies the greatest ratio, using more than half of all the welding consumables. Most of the welding done in assembly employs flux-cored wires (FCW). Typical wires for shipbuilding include FAMILIARC™^{note 2)} DW-100, which can be used in all positions, and FAMILIARC™ DW-100V, which has excellent gap tolerance and enables highly efficient welding in the vertically upward direction.

Welding performance was confirmed by the aspect shown in **Table 1** to find out which wire is more suitable for robotic welding. As a result, FAMILIARC™ DW-100 was adopted; it can be used in all positions.

In order to introduce a robot into the actual production line, preparation must be made for various welding situations. The following describes the three points involved in the preparation for the introduction of a robot into the production line.

1) Welding with gaps in vertical positions

Because of the structure, in which transverse elements are inserted in longitudinal elements, there are inevitable gaps between the transverse elements and longitudinal elements in an assembly. The gaps created are not uniform, ranging from approximately 0 mm to 4 mm.

Hence, the welding conditions corresponding to each gap dimension have been developed as shown in **Fig. 8**. At that time, arc tracking




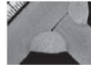
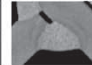
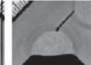
Wire	DW-100		
Welding currents (A)	220	220	200
Welding Speed (cm/min)	16	12	6
GAP (mm)	0	3⇒0 (shift)	5
Bead appearance			
Macrostructure			

Fig. 8 Gap tolerance for vertically upward welding

performance, the basic performance of a robot,³⁾ was also confirmed. This has enabled the tracking of welding lines during vertical position welding even with thermal deformation occurring during the welding and/or when transverse elements are tilted.

2) Welding of collar plates

For each target workpiece, welding conditions must be established not only for vertical position welding and horizontal fillet welding, but also for the oblique welding of collar plates, where the welding switches from a vertical position to that of horizontal fillet welding, and for the corner parts of collar plates of different shapes so as to smooth the appearance of their beads.

This time, the positions at which switching from vertical welding positions to oblique joints or to corner parts takes place are judged by the dimensions of gaps in the teaching software so as to optimize the welding conditions for each joint and to realize a smooth bead appearance as shown in **Fig. 9** and **Fig.10**.

3) Corner filling and intersection between horizontal fillet and vertical position welding

There are gaps opening in the corners before welding, and welding conditions must be established to close these openings. Also, welding conditions must be devised to achieve a favorable appearance at locations where horizontal fillet welding and vertical position welding intersect. The shape of each gap is like a triangle, widest at the bottom and gradually narrowing upwards. Therefore, the weaving width of the welding

note2) FAMILIARC™ (**FAMILIARC™**) is a trademark of Kobe Steel.



Fig. 9 Robotic welding result A



Fig.10 Robotic welding result B

robot has been changed to match the shapes and to fill the gaps. Subsequently, the vertical position welding continues without stopping the arc, so as to eliminate bead connections. In the case of horizontal fillet welding, a backstep operation has been applied so that the gap is overlapped on the bead after filling before applying the main welding conditions. This has enabled a favorable bead appearance to be made at each intersection (Fig.11).

2. Current work

2.1 Development of FCW designed for welding robots

Currently, works are being done to improve the efficiency of robotic welding. One of them is a study being conducted to improve the efficiency from the aspect of welding consumables.

In the target portions of robotic welding, vertical position welding occupies much of the welding time. The efficiency improvement essentially requires the improvements in efficiency and quality of vertical



Fig.11 Intersection of hull member after welding

position welding.

As described in Section 1.4, there is FAMILIARC™ DW-100V, an FCW realizing high efficiency in vertical position welding. This consumable, however, has a slight disadvantage in the horizontal fillet bead shape and welding condition tolerance.

Since horizontal fillet welding and vertical position welding are mixed in a series of tasks, a robot, which cannot distinguish welding consumables, must perform both welding jobs with one welding wire.

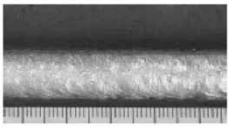
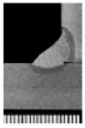
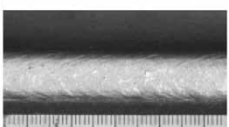
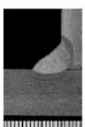
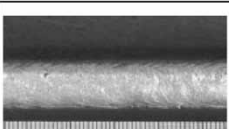
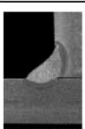
Hence, the wire design has been reexamined on the premise of using the wire with welding robots. An FCW, "FAMILIARC™ DW-100R," designed for robotic welding, has been developed to be used in combination with a robot to realize both horizontal fillet welding and vertical position welding at high efficiency.

FAMILIARC™ DW-100R can produce weld metal with adjusted viscosity and slag generation, etc., and also can be optimally controlled when combined with the CB controller. As a result, the workability in the vertically upward direction has been improved while maintaining the same fillet welding workability as that of FAMILIARC™ DW-100.

Fig.12 shows the bead appearance and cross-sectional macrostructure of horizontal fillets. It is shown that FAMILIARC™ DW-100R has achieved the same bead appearance and shape as that of FAMILIARC™ DW-100 with an undercut smaller than that of FAMILIARC™ DW-100V.

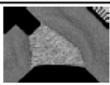
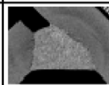
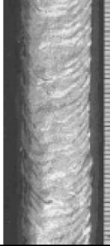

Fig.13 shows the bead appearance and cross-section for vertical position welding. FAMILIARC™ DW-100R is capable of welding with a higher electric current and higher welding speed comparable to those of FAMILIARC™ DW-100 in the vertically upward welding and results in a favorable bead appearance and cross-sectional shape.

Furthermore, it has an improved gap tolerance and enables welding with a small leg length at a

Wire	Bead appearance	Macro structure	Under cut (mm)
DW-100R			0.09
DW-100			0.09
DW-100V			0.14

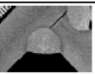
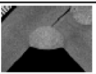
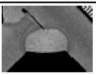
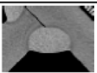




*1) Welding by robot system
 *2) Leg length (Target) : 6mm
 *3) Welding current: 260A Travel speed: 40cm/min
 *4) Wire dia.: 1.2mm

Fig.12 Bead appearance and macrostructure of horizontal fillet welding

Wire	DW-100R	DW-100
Macro structure		
Bead appearance		
Welding current (A)	200	200
Welding speed (cm/min)	8	6
Leg length (mm)	10	13

*1) Welding by robot system
 *2) Wire dia.: 1.2mm

Fig.14 Bead appearance and macrostructure of vertically upward welding (Gap: 5mm)

Leg length (Target) (mm)	6		8	
	Wire	DW-100R	DW-100	DW-100R
Macro structure				
Bead appearance				
Welding current (A)	240	220	240	220
Welding speed (cm/min)	25	23	18	16

*1) Welding by robot system
 *2) Wire dia.: 1.2mm

Fig.13 Bead appearance and macrostructure of vertically upward welding

high welding speed in a wider gap range. Fig.14 shows the bead appearance of vertical position welding at a gap width of 5 mm.

FAMILIARC™ DW-100R is acquiring shipping approval equivalent to that of FAMILIARC™ DW-100, even in semiautomatic welding, besides shipping approval in fully automatic welding, so that it can be used for the rework after robotic welding and areas other than robotic welding.

2.2 Work toward Internet of Things (IoT)

The Internet of Things (IoT) is attracting

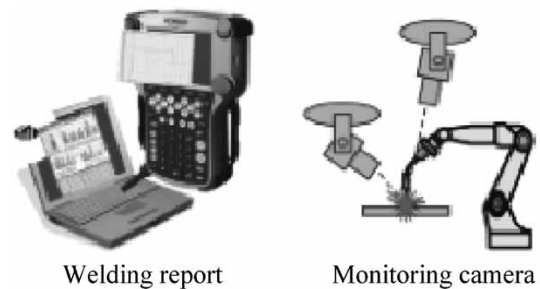


Fig.15 Example of IoT

worldwide attention, including Industry 4.0 proposed by Germany, the Industrial Internet Consortium (IIC) established by five US companies and the IoT Acceleration Consortium in Japan. Sensors are installed in machinery or equipment, and the data is collected via a network to be analyzed for improving the efficiency of operation while reducing the cost of maintenance. Machines are controlled and operated remotely to achieve labor saving. These are a few examples of the developments seen in various organizations.

In Kobe Steel, welding robots are connected to production-support PC software (AP-SUPPORT™) to promote information visualization via the robots. The visualization of the operation data and error status can prevent short time breakdown and improve productivity. In the CB controller, an arc monitor is used to collect welding status data to check any trouble-causing phenomena, and a production monitoring camera is used in parallel for grasping more detailed status (Fig.15).

Conclusions

This paper introduces a welding robot that can enter narrow, limited spaces inside a workpiece to perform welding work and newly developed teaching software incorporating optimum welding conditions and motions. A robotic welding system incorporating the above for the assembly process in shipbuilding is also introduced. This system can be operated by a few workers and contributes to improving the production efficiency of the welding stage.

As a welding solution company, Kobe Steel will continue to strengthen the product lineup for each welding stage in shipbuilding blocks, from single-sided submerged arc welding apparatuses for the

plate splicing processes to robotic systems for the sub-assembling and assembling processes. At the same time, the company will continue to work on the development of automated welding solutions, including strengthening the lineup of welding consumables.

References

- 1) Y. Okumoto. *Shipbuilding Technology & Production System*, SEIZANDO-SHOTEN Publishing Co., Ltd, 2009-2-13, pp.18-19.
- 2) M. Mizuno. *ETOKI DE WAKARU 3-JIGEN CAD NO HON*, Nikkan Kogyo Shimibun, Ltd. 2010-3-1, pp.8-9.
- 3) Y. Inoue et al. R&D Kobe Steel Engineering Report. 2004, Vol.54, No.2, p.91.

Features of New Robot Controller, CB-type Controller, for ARCMAN™ Welding System

Takeshi KOIKE*¹, Shuichi INADA*¹, Atsushi FUKUNAGA*¹, Naoki KIDA*¹, Tsutomu ONE*²

*¹ Welding System Dept., Technical Center, Welding Business

*² Production Systems Research Laboratory, Technical Development Group

Recently, the needs for welding automation have become more diversified and advanced, requiring a robot controller with higher performance and improved functions. Hence, we have developed a new controller, the CB-type controller, which features high performance, highly-sophisticated functions, and ease of use. This paper introduces these three features. In addition, the potential of the CB-type controller is described along with the example of a new arc-sensor control system under development.

Introduction

During the welding of medium and heavy plate, multi-layer welding is performed over a long period of time to overlay multiple layers of weld metal. This results, among other things, in the need for an arc sensor technology for tracking the displacement of welding lines due to thermal strain, etc., and vibration suppression control technology for the sound performance of welding using weaving. In recent years, the requirements of welding automation are becoming more sophisticated due to changes in the structure of welding targets, changes in the steel material used, the lack of skilled welders, and so on. In response to these needs and to support further evolution in the welding of medium and heavy plate, we have pursued performance upgrading, functional upgrading and simplification. It is against this backdrop that the CB-type controller has been developed for delivering solutions in welding automation around the world on the basis of the concept, "Welding from start to finish anywhere in the world." (Fig. 1, Fig. 2)



Fig. 1 CB-type controller and teaching pendant

Welding from start to finish anywhere in the world

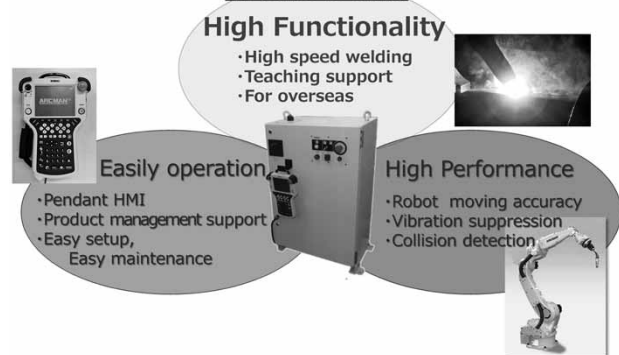


Fig. 2 The concept of CB-type controller

This paper presents an overview of the advantages of the CB-type controller, which has been in the market since April 2016, and takes up the supporting technology, as well as the future potential of this newly developed controller.

1. Advantages of CB-type controller¹⁾

The main advantages of the CB-type controller are (1) high performance, (2) high functionality and (3) ease of use. This section describes these three advantages.

1.1 High performance supporting welding of medium and heavy plate

The CB-type controller has improved CPU performance with a renewed internal architecture, in which the user interface and real-time controller are optimally separated. In addition, EtherCAT® (Registered trademark of Beckhoff Automation GmbH & Co. KG, Germany) has been adopted for the communication with the manipulator, peripheral devices, and welding power source. This has improved the high-speed, high-accuracy synchronous communication performance necessary for a welding robot with upgraded performance and has realized control performance more than three times greater than that of the conventional types.

The "touch-sensing with welding wire" function, used for detecting the displacement of welding targets, requires the robot to stop abruptly at the moment when the welding wire comes in contact with each welding target. Such an abrupt stop,

however, can cause the robot to vibrate, leading to an error in positional detection. One way to reduce this error may be to perform positional detection after the vibration stops; however, the waiting time involved in stopping can cause the problem of increased tact time. Hence, the CB-type controller exploits the advanced model-based control technology²⁾ that has been modified for reducing the vibration and waiting time, thus decreasing the touch-sensing time by 20% compared with the conventional models (Fig. 3, Fig. 4).

1.2 High functionality to meet various welding needs

The improved hardware performance has enabled the provision of many functions that demonstrate strengths in automating the welding of medium and heavy plate. The following introduces some of the newly added functions.

1.2.1 Weaving customization function

An oblique-weaving function, independent voltage setting for vertical and lower plates, and end-stop time setting have enabled horizontal fillet welding with a leg length of 6 mm with neither undercut nor overlap, even at a high electric current of 450A and high-speed welding condition of 70 cm/

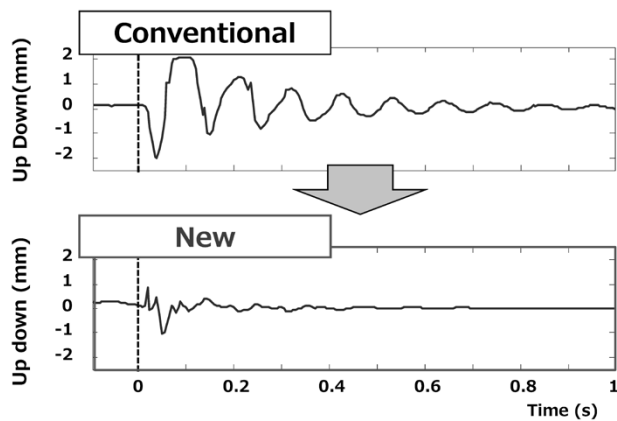


Fig. 3 Vibration duration after wire touch sensing

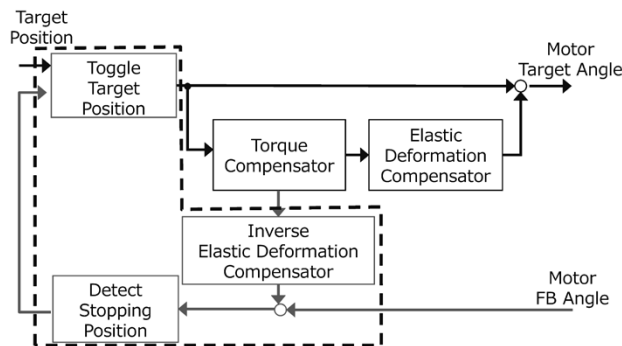


Fig. 4 Example of model-based control

min.³⁾ (Fig. 5, Fig. 6)

This function is also effective in improving the shape of the reinforcement beads of single bevel grooves. Fig. 7 and Fig. 8 show examples in which oblique weaving is applied to the second pass of 2-layer 2-pass welding performed on workpieces with a plate thickness of 8 mm and a groove angle of 45°.

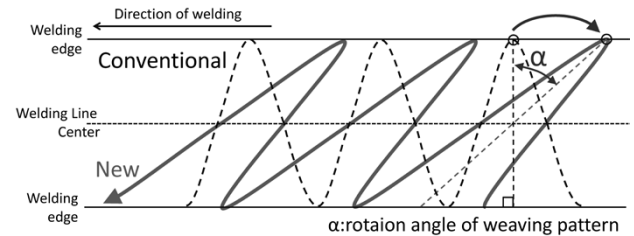


Fig. 5 New back-and-forth weaving pattern

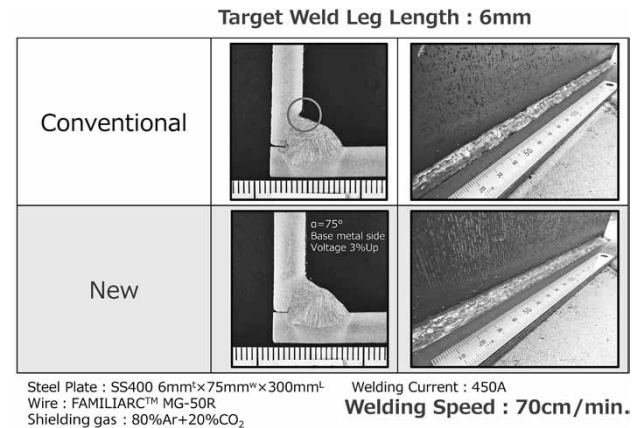


Fig. 6 Weld bead shape and appearance

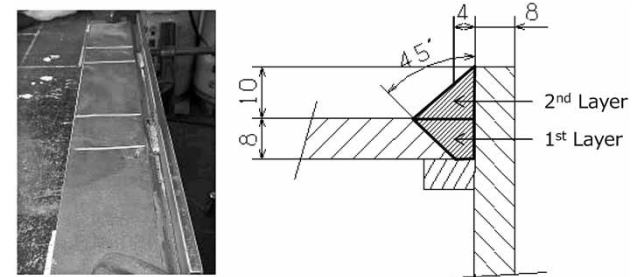


Fig. 7 Groove configuration of test plate

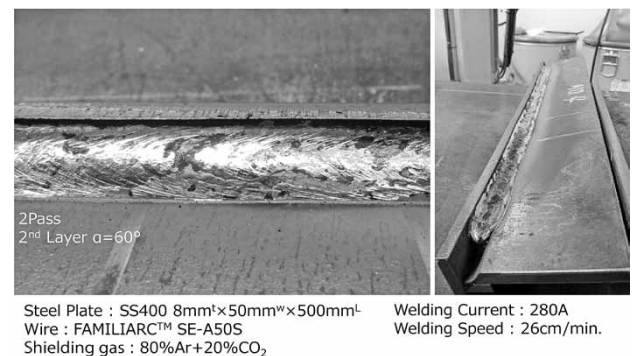


Fig. 8 Weld bead shape with bevel groove

1.2.2 Visual support for production status

If any problem occurs during the operation of a welding system, the accurate and objective acquisition of information before and after its occurrence is the key to early problem solving. In order to acquire this information, a robot-operation log and welding-result log are stored inside the controller. Although this function has been provided in conventional controllers, the CB-type controller has an increased internal memory capacity and has a log saving capacity 20 times that of the conventional controllers, enabling the acquisition of more detailed information.

Furthermore, the visualization of operational data and error occurrence status in cooperation with Kobe Steel's production support PC software (AP-SUPPORT™) can contribute to promoting the improvement of productivity, computerization and visualization at production sites (Fig. 9).

1.3 Simplification realizing favorable operability

A new teaching pendant has been developed, which, while inheriting the operability and high responsiveness responsible for the popularity of the conventional devices, is also light, easy-to-see, and easy-to-touch. Thanks to this pendant, even first-time users of the Kobe Steel's welding robot system can make inputs easily and intuitively (Fig.10). The following describes the advantages of the teaching pendant.

1.3.1 Light Weight

The pendant has not only a body weighing 0.95 kg, the industry's lightest class, but also considerations such as optimum weight balance that have been taken into account in the design. Moreover, a significant reduction in burden has been realized in the teaching/confirmation of welding work, which used to take a long time and impose a heavy burden on operators. More specifically, a

forward switch for the teaching program has been added on the back of the teaching pendant,⁴⁾ and two enabling switches (optional) have been provided so that the teaching pendant can be held by either hand (Fig.11).

1.3.2 Intuitive operation and display

The intuitive input based on icons and touch panel (Fig.12), as well as the robot-teaching commands that are color-coded separately (Fig.13), have realized an operating environment that is user-friendly even for beginners.⁵⁾

Moreover, the cross arrangement of keys,⁶⁾ matching the direction of robot operation, has



Fig.10 New teach pendant for CB-type controller

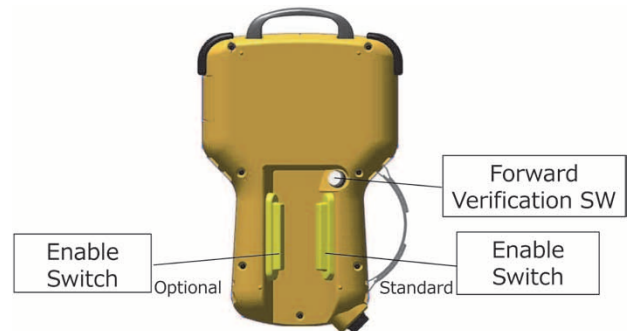


Fig.11 Switch arrangement on rear side

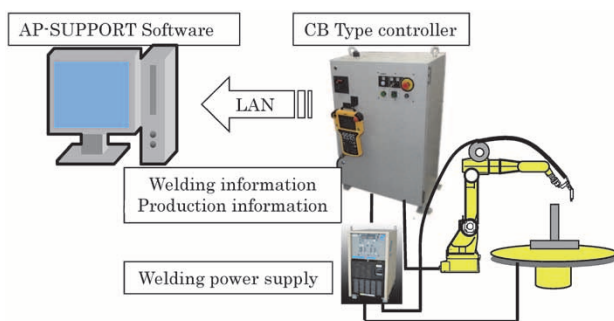


Fig. 9 Cooperation with AP-SUPPORT™

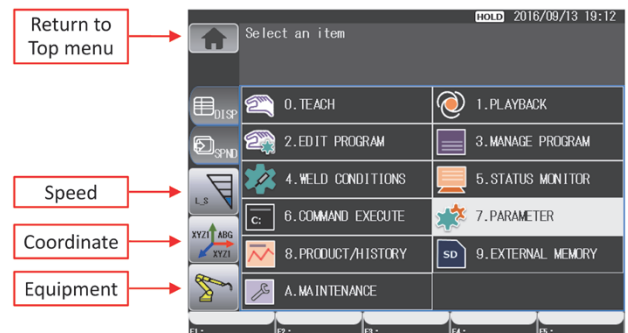


Fig.12 Touch panel screen



Fig.13 Coloring of robot teaching commands

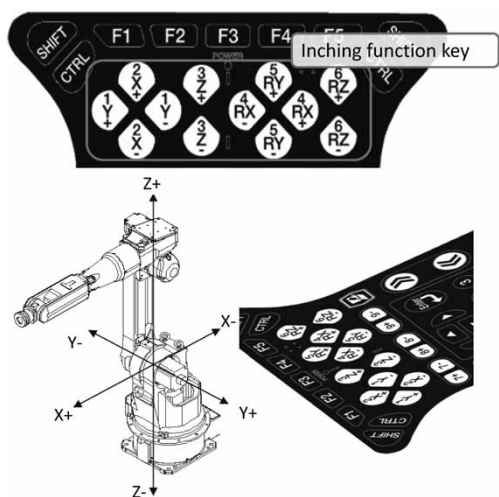


Fig.14 New cross arrangement of inching keys

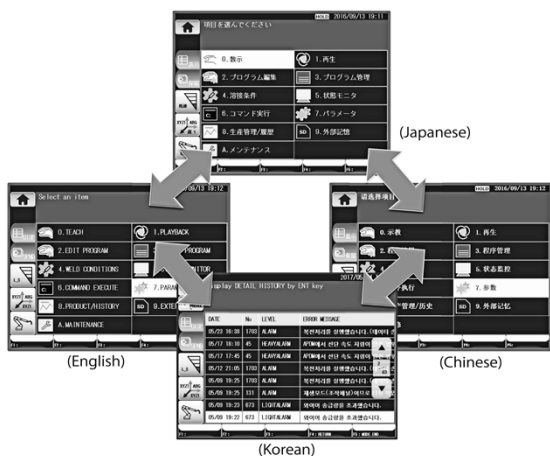


Fig.15 Easy language switching

improved operability during the inching movement of the robot (Fig.14). This feature is expected to reduce operational errors significantly.

1.3.3 Easy language switching

The operational displays are given in Japanese, English, Chinese, as well as in Korean. The languages can be switched instantly on the touch panel (Fig.15). This switchability takes into

account the start-up and maintenance work done by Japanese staff at overseas factories.

2. Future prospects of CB-type controller

The welding of medium and heavy plate essentially requires further improvement in the performance of the arc-sensor function for tracking the weld lines displaced due, for example, to the thermal strain during welding. To this end, the upgraded capacity of the CB-type controller has been fully exploited.

In general, an arc sensor function using the feedback of welding electric current detects the displacement of weld lines on the basis of a difference in the electric current between the left and right ends of weaving. However, the electric current varies widely, limiting the ability to improve the accuracy of an arc sensor based only on the electric current values at the left and right ends.

Hence, the feedback values of continuous electric current during weaving are used to develop a method of obtaining the amount of displacement by regression fitting based on the least-square method. A simplified model, expressed by the following equation (1), has been used:⁷⁾

$$I(t) = p_1 \sin(\omega t) + p_2 \sin\left(2\omega t + \frac{\pi}{2}\right) + p_3 \dots \dots \dots (1)$$

wherein $I(t)$ is an electric current waveform vector for the latest weaving cycle at time t , and the regression coefficient, p_1 , corresponds to the displacement in the left and right directions. This model has been verified for five patterns of horizontal fillet welding; i.e., no displacement, displacements of 2 mm and 5 mm on the vertical plate, and displacements of 2 mm and 5 mm on the lower plate. Fig.16 shows the relationship between the regression coefficient, p_1 , and the displacement amount, confirming that p_1 increases as the amount of displacement increases.

A small standard deviation of the estimated displacement is considered to indicate a stable estimation of displacement. The standard deviation of the estimated displacement can be obtained by dividing the standard deviation of coefficient p_1 in each displacement amount in Fig.16 by the slope of the average value. In comparison with our conventional technique based on the difference in electric current at the left and right ends,⁸⁾ the standard deviation of the estimated displacement has decreased by approximately 8% in the case of Ar-CO₂ gas welding and approximately 40% in the case of CO₂ gas welding.

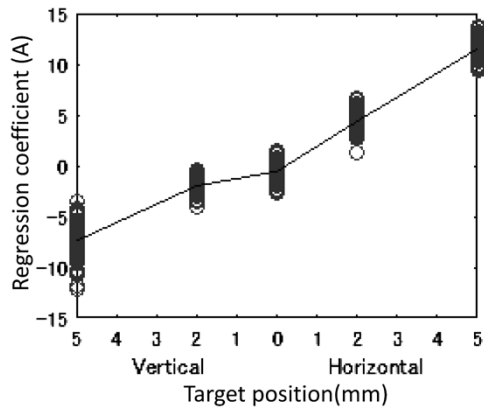


Fig.16 Relationship between regression coefficient and target position

Conclusions

This paper explains the functions and potential of a newly developed robot controller, the CB-type controller. The capabilities of the CB-type controller are being exploited in the control of new manipulators, ARCMANTM note 1) -A30/A30S and ARCMANTM-A80.

In order to solve all welding issues, Kobe Steel will strive to make use of the CB-type controller, pursuing performance upgrading, functional upgrading and simplification to meet user needs and make new proposals to promote easy-to-operate, high-quality welding around the world.

References

- 1) S. Inada. Boudayori technical guide/welding technology, technical report. 2016. 10. <http://www.boudayori-gijutsugaido.com/magazine/vol492/report.html>
- 2) Japanese Patent No. 5897644, 2016.3.11
- 3) Japanese Unexamined Patent Application Publication No. 2016-209890.2016.12.15
- 4) Japanese Unexamined Patent Application Publication No. 2016-97482.2016.05.30
- 5) Japanese Design Registration No. 01559048. 2016.08.19
- 6) Japanese Patent No. 5642304. 2014.11.7
- 7) T. One et al. "Development of Arc Sensor based on a simple model." Preprints of the National Meeting of JWS, Spring 2017. 2017.4.19-21. Japan Welding Society, 2017, pp. 74-75.
- 8) K. Kawakami. Boudayori technical guide/welding technology, technical report. 2000.2 <http://www.kobelco.co.jp/welding/files/200002.pdf>

note 1) ARCMANTM (**ARCMANTM**) is a registered trademark of Kobe Steel.

New Arc-welding Robots

Tatsuji MINATO*1, Taichi IGARASHI*1, Motoaki MURAKAMI*2, Takashi WADA*3

*1 Welding System Dept., Technical Center, Welding Business

*2 Technical Center, Welding Business

*3 Production Systems Research Laboratory, Technical Development Group

A series of arc-welding robots, the ARCMAN™ series, comes in sizes suitable for various welding objects, and many have been adopted by users in the field of medium and heavy plate. This paper introduces the features of a large-sized robot, ARCMAN™ A80, and a small-sized robot, ARCMAN™ A30, both newly developed. ARCMAN™ A80 is a robot suitable for welding large structures, such as construction machinery, and has enhanced features for improving welding applicability, including an expanded approach area around work pieces, while inheriting the features of the conventional ARCMAN™ XL. ARCMAN™ A30 is a small robot aimed at applications in narrow spaces and features an operating speed and arm shape particularly suitable for the assembly process of shipbuilding.

Introduction

Kobe Steel's arc-welding robots have been widely used around the world in the fields of medium and heavy plate (e.g., construction machinery, steel frames, bridges and railway vehicles).

Fig. 1 shows an example of the welding system. In the field of medium and heavy plate, where work pieces (welding objects) tend to have large sizes, it is difficult for a single robot to cover all the welding locations of a work piece within its work envelope. Each Kobe Steel welding system combines a robot that is suitably sized for work pieces, a transfer apparatus upon which the robot is mounted, and a positioner which places each work piece in its optimum welding postures: the equipment is configured to cover the welding locations required. Kobe Steel has an assortment of small to large-sized robots, all of which have the dynamic characteristics necessary for realizing high quality welding.

Fig. 2 shows the lineup of the Kobe Steel robots. Each small-sized robot has a small mass and imposes a minimal burden on its transfer apparatus, making the system lighter and more compact. On the other hand, the maximum reach of each small-sized robot is limited, giving it a small work envelope, which is disadvantageous in application to larger work pieces. The opposite is true for large-sized robots. This is the reason why many welding systems adopt medium-sized robots, each having a maximum reach of 1,300 to 1,800 mm with an excellent balance between the work envelope area and robot mass.

Meanwhile, a large-sized robot that has been

given the maximum reach can simplify the system configuration, since the robots can be applied to the welding locations of each work piece without being mounted on a transfer apparatus. In this respect, the large robots are highly valuable. In the case of shipbuilding, etc., which requires entrance into space-limited members, such as the inside of a work piece, a small-sized robot makes it possible to automate the jobs that have hitherto been done by welders.

This paper introduces the features of a large-sized arc-welding robot, ARCMAN™ note 1) A80, which has been modified from its conventional model, and a newly developed small-sized arc-welding robot, ARCMAN™ A30.

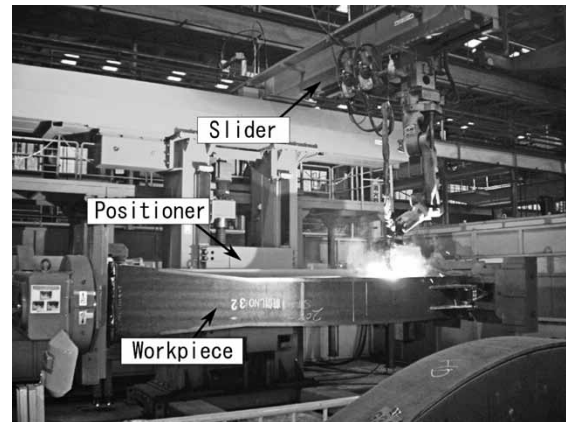


Fig. 1 Welding system

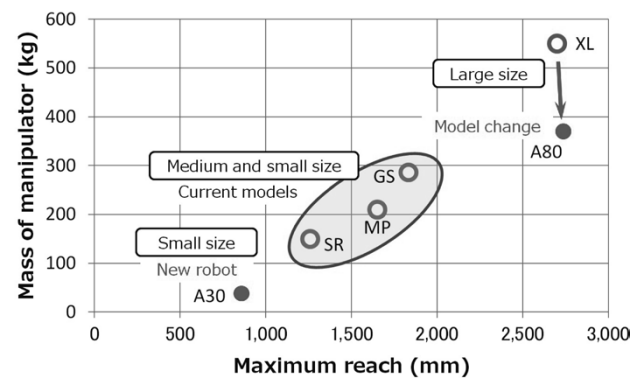


Fig. 2 Lineup by robot size

note 1) ARCMAN™ (ARCMAN™) is a trademark of Kobe Steel.

1. Large-sized arc-welding robot, ARCMAN™ A80

In the past, the largest sized model among the line-up of Kobe Steel's robots was ARCMAN™ XL (Fig. 2, Fig. 3). Its maximum reach is 2,698 mm at point P (the center of the S5 rotation axis), and this feature has been advantageously exploited in applications in industries such as construction machinery and railway vehicles, where large work pieces are handled. ARCMAN™ A80 has been developed as a successor of ARCMAN™ XL and has additional features that make it more suitable for large work pieces.

1.1 Advantages of ARCMAN™ A80

The following describes the main advantages of ARCMAN™ A80:

- Adoption of serial link: Expansion of the area of approach to work pieces

The enlargement of the work envelope and the postures in which the upper robot arm bends to the rear of the robot (reverse posture) have enabled approaching work pieces that have previously been impossible to reach (Fig. 4).

- Cables built into S1 axis: Prevention of interference between cables and work pieces

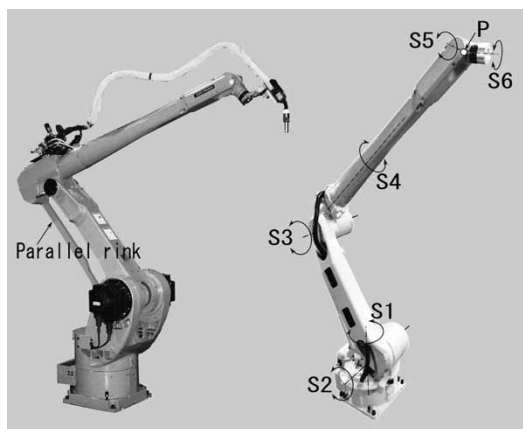


Fig. 3 ARCMAN™ XL (left) & ARCMAN™ A80 (right)

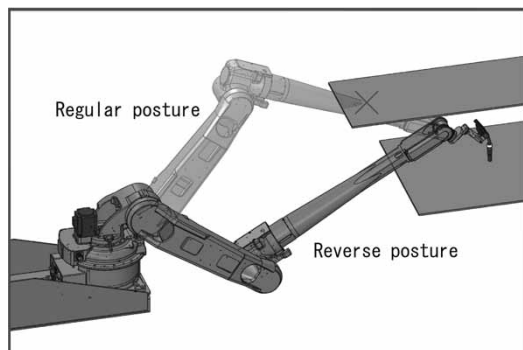


Fig. 4 Reverse posture of ARCMAN™ A80

ARCMAN™ A80 inherits the long arm, the greatest advantage, of ARCMAN™ XL, and has the same arm length as the latter so as to be compatible with already-delivered systems, their replacement being taken into account. In addition, the frame has been optimized by using the latest parts and design/analysis with 3D-CAD. Furthermore, serial linking has been adopted, as described later. These measures have realized a reduction in weight that makes the apparatus approximately 35% lighter than conventional models. In terms of performance, the operational speed has been increased to improve productivity.

1.2 Adoption of serial link

ARCMAN™ XL adopts a parallel link structure, which has enabled a reduction in the capacity of the driving motor of the S3 axis and also has been advantageous in terms of rigidity. There have, however, been drawbacks such as a limited work envelope, limited operational speed, increased robot size and increased number of parts. By adopting a serial link, ARCMAN™ A80 has managed to improve its performance while reducing the number of parts and the weight.

Structurally, it is much more difficult to secure rigidity in a serial-link type robot than in a parallel-link type robot, and the reduction in rigidity leads to the deterioration of weaving accuracy, which is important in the welding of medium-to-heavy gauge plates. In particular, a large-sized robot has a long span from its robot base to its torch; hence, the deterioration in accuracy can be significant, causing serious problems. This problem has therefore been solved from the aspects of both design and control.

In the mechanical design, a high rigidity has been achieved by optimizing the frame shape using 3D-CAD and numerical analysis. Fig. 5 shows a robot posture and its FEM model, whose posture

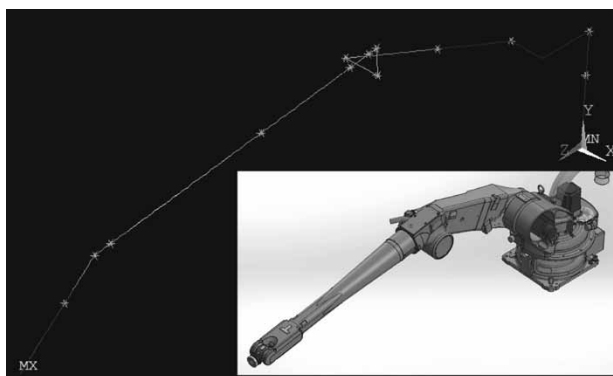


Fig. 5 FEM model of ARCMAN™ A80

during welding requires the greatest strictness in regard to locus accuracy. By expressing the robot postures according to the FEM analysis model, the natural frequency of the robot as a whole has been predicted. In addition, the important reinforcement points that contribute largely to overall rigidity have been identified to attempt an improvement in the rigidity. As a result, a rigidity almost equal to the theoretical value, in which the frame is deemed a rigid body, has been secured successfully.

In terms of control, a numerical model closer to the actual machine has been created to improve the rigidity and the accuracy of locus simulation in prototype design. This model has been used to perform a highly accurate simulation of the resonance phenomena occurring at the tool center position (TCP), especially during weaving. As shown in Fig. 6, the simulator consists of a robot model and a controller model. For the robot model, Simscape Multibody™ (simulation tool made by MathWorks®) has been used to incorporate the design data of the 3D-CAD to create precise models for the link structure of the robot, as well as the mass, the position of the center of gravity, and the inertia of each link. For the controller model, the actual controller source code has been used to

reproduce the control algorithm with Simulink™ (made by MathWorks®). An example of TCP locus during weaving is shown in Fig. 7. It has been confirmed that the simulation well reproduces the robot tip behavior of the experimental machine. It should be noted that, for the purpose of achieving the desired weaving accuracy, the robot control algorithm^{1),2)} comprises not only feedback control, but also a two-degree-of-freedom control according to feedforward control based on a dynamic model, an elastic deformation compensation control for correcting robot deflections by inertial force and/or gravity, and a periodic disturbance observer focusing on periodic disturbance components. Fig. 8

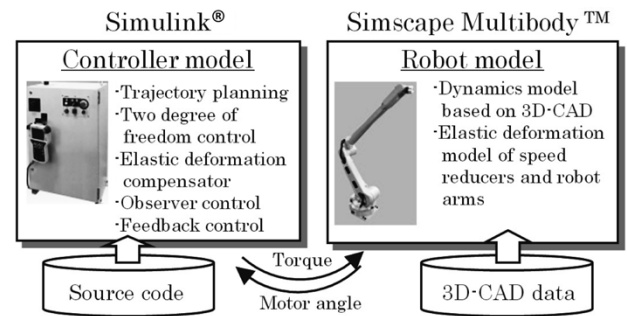


Fig. 6 Simulation collaborating with 3D-CAD

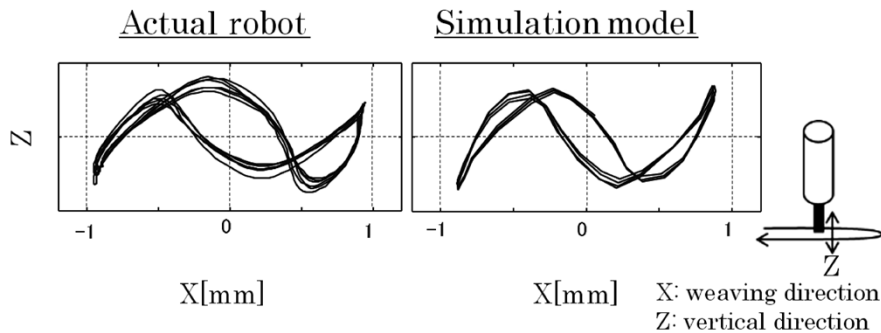


Fig. 7 TCP behavior during weaving action of actual robot and simulation

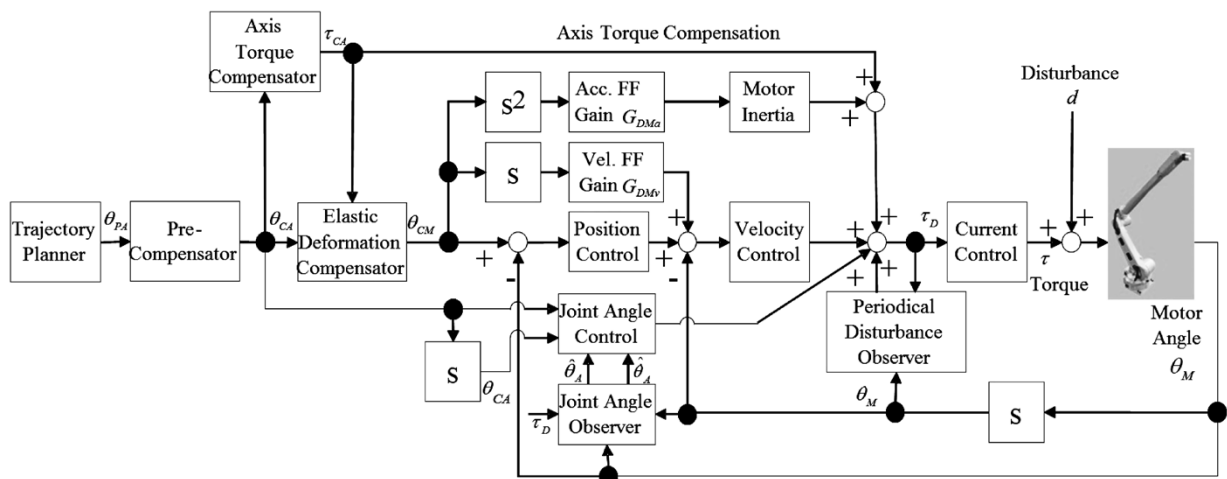


Fig. 8 Block diagram of control system

shows the control block diagram of the robot.

The simulator thus constructed has been exploited to tune the control parameters and brush up the control algorithm, which has solved the problem of the operational accuracy being deteriorated due to robot resonance.

The increased rigidity of the robot along with the new control technology has secured the desired weaving accuracy of the actual ARCMAN™ A80 machine adopting the serial link.

1.3 Built-in cables

In the field of medium and heavy plate, in particular, welding is performed with a current typically exceeding 400A and, hence, requires large-diameter welding cables and torch-cooling water hoses, all of which must withstand the high current. In addition, there are cases where tools are changed, or optional sensors are used together, which tends to increase the number of cables. When these cables follow the motion of the robot and are shaken, they may interfere with the work piece and peripheral devices constituting the welding system. In addition, instruments for holding the massive cables are also required, and addressing these problems can limit the layout design of the system.

For that reason, ARCMAN™ A80 comprises, in particular, a welding power cable with a large diameter and greater mass, and the cable is fitted along the machine frame of the arm part and built into the robot in the base part. Through these measures, the layout design of the welding system has been made more flexible, so as to improve the applicability and welding quality of the system.

2. Advantages of small-sized arc-welding robot, ARCMAN™ A30

The appearance of ARCMAN™ A30 is shown in Fig. 9. This machine comprises a small-sized robot aiming at applications such as the assembly processes of shipbuilding, where welding work must be performed inside the space-limited parts of work pieces.

2.1 Two types of specifications adapted for applications

Japanese Ordinance on Industrial Safety and Health stipulates that "The employer shall, in the case where an industrial robot is operated, and when it is liable to endanger workers due to contact with the said industrial robot, take the necessary measures of providing a railing, an enclosure, etc.,

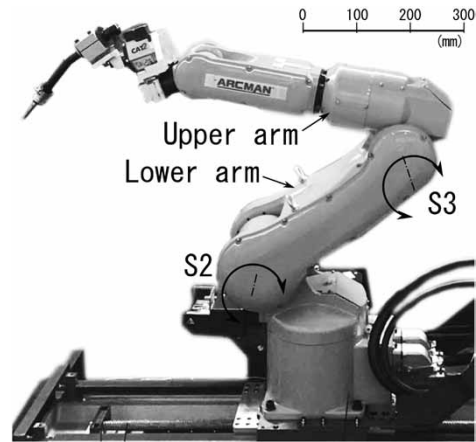


Fig. 9 ARCMAN™ A30

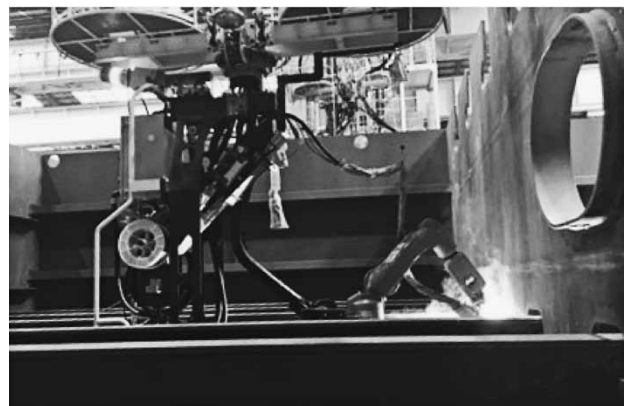


Fig.10 Welding site at shipbuilding yard

to prevent the said dangers (Article 150-4)," for industrial robots, each having a rated power greater than 80W.

Fig.10 shows welding work performed in the shipbuilding assembly process, which is the major target of ARCMAN™ A30. On such a work site, isolating workers and robots with a railing or enclosure (hereinafter referred to as "safety fences") is difficult due to operational constraints, and it is necessary to take measures for the above rules to secure safety. On the other hand, industries and work sites that can install safety fences require increased speed (increased output) of the robot in order to improve their productivity.

To cope with these contradictory problems and needs, two types of servo amplifiers have been provided to limit the motor output on the controller side, enabling the robots to be deployed in a wider range of fields and markets.

2.2 Lower-arm structures for realizing small size

In shipbuilding, the assembly processes require robots to enter narrow spaces inside the hull blocks and to take welding postures for horizontal fillet

welding and vertical position welding. Hence, the robot arms, both lower and upper, must have relatively short link lengths. Therefore, in some welding postures, there is a concern that the torch cable may wrap around a protrusion on the robot, rendering welding impossible. Against this backdrop, ARCMAN™ A30 has been given a structure in which the motors of the S2 axis and the S3 axis are built into the lower arm so as to eliminate protrusions on the robot surface as much as possible. In order to arrange the two motors of the S2 axis and the S3 axis in the limited space inside the lower arm, a belt tension adjuster has been shared by the S2 axis and the S3 axis (**Fig.11**). The resin casing that covers

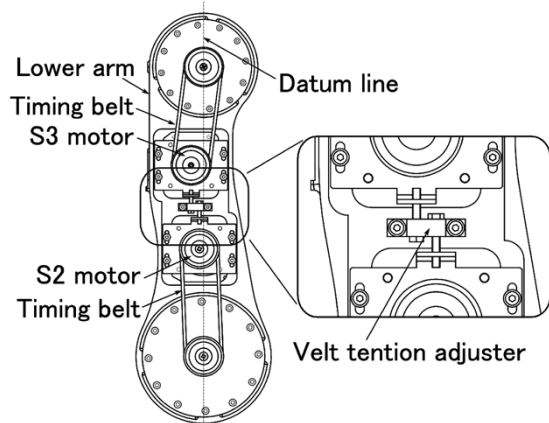


Fig.11 Structure of lower arm

the belts and pulleys also has a rounded design. Thanks to this devising, welding has been made possible without the fear of the cable being caught by the robot body even when welding in narrow spaces.

Conclusions

The lineup of Kobe Steel's arc-welding robots has been explained along with the advantages of the new models. We will strive to provide welding systems best suited to each type of welding job, offering ARCMAN™ A80 for the welding of large-sized structures such as construction machinery, and ARCMAN™ A30 for space-limited members such as those found in the assembly process of shipbuilding.

References

- 1) Y. Nishida et al., Journal of the Society of Instrument and Control Engineers. 2012, Vol.51, No.9, pp.874-879.
- 2) S. Inada et.al. R&D Kobe Steel Engineering Reports. 2013, Vol.63, No.1, pp.89-93.

Formation of Fine Microstructure in Weld Metal Containing Mn-Ti based Oxides

Hidegori NAKO*¹, Yoshitomi OKAZAKI*¹, Dr. Hitoshi HATANNO*¹, Ken YAMASHITA*², Hideaki TAKAUCHI*²

*¹ Materials Research Laboratory, Technical Development Group

*² Welding Process Dept., Technical Center, Welding Business

The formation of fine acicular ferrite microstructure and toughness improvement have been observed in a welding metal in which inclusion particles containing Mn-Ti based oxide are dispersed. The inclusion particles are composed of MnTi₂O₄, TiO₂, amorphous and MnS phases, while the acicular ferrite has been nucleated from the MnTi₂O₄ phase. The Baker-Nutting crystal orientation relationship has been found between MnTi₂O₄ phase and acicular ferrite, whereas the Kurdjumov-Sachs orientation relationship has been found between the prior austenite phase and acicular ferrite. It has been discovered that the favorable lattice matching at the interface between the prior austenite phase and acicular ferrite may possibly have promoted the nucleation and growth of acicular ferrite, as well as the lattice matching at the MnTi₂O₄/acicular ferrite interface.

Introduction

As steel structures such as ships, buildings, and offshore structures become larger and are used in environments at lower temperatures, higher strength and toughness are required for weld metals. In the strengthening mechanism of steel, grain boundary strengthening (grain refinement strengthening) is known to improve strength and toughness simultaneously.¹⁾ Hence, realizing a weld metal that combines high strength and high toughness requires technology to refine the microstructure of weld metal.

Acicular ferrite (hereinafter referred to as "AF") is a microstructure that is generated from inclusion particles, as nucleation sites, in the weld metal of low carbon/low-alloy steel and in the heat-affected zones of welds. This microstructure provides high toughness.²⁾⁻⁴⁾ The inclusions that are known to act as the nucleation sites for AF generation are oxides,⁵⁾ nitrides,⁴⁾ and sulfides.⁶⁾ In particular, Ti oxides such as TiO,⁷⁾⁻⁹⁾ Ti₂O₃,⁹⁾ and TiO₂¹⁰⁾ effectively promote the formation of AF.

The following three theories have been proposed for the generation mechanism of AF from inclusions as a nucleation site.

(1) The decrease in inclusion/AF interface energy: When an interface with favorable lattice matching is formed between an inclusion and AF, the interface energy between the inclusion and AF decreases, facilitating the nucleation of AF on the surface of

the inclusion. This is a concept focusing on the structural energy component of the interface energy and has been studied for a long time.^{8), 11)} In recent years, researches based on chemical energy have also been conducted.¹²⁾

(2) A compositional change of austenite phase around inclusions: This is the theory that the composition of the austenite phase around inclusions changes before the AF is generated such that the driving force for AF generation increases. The Mn-depleted zone is cited as an example.¹³⁾ It has been shown that, when Mn, an austenite stabilizing element, is absorbed by inclusions, a Mn-depleted zone is formed in the vicinity of the inclusions, raising the Ae₃ temperature. Furthermore, Gregg has pointed out the existence of a C-depleted zone in which C is another austenite stabilizing element.¹⁰⁾

(3) The introduction of strain and dislocations to the austenite phase around inclusions: This is the theory that the difference in the coefficient of thermal expansion between inclusions and austenite phase causes strain and dislocations in austenite phase around inclusions, promoting the generation of AF; however, there is little experimental evidence. It has been shown by calculation that the contribution of strain energy to the driving force of ferrite transformation is small.¹⁴⁾ On the other hand, Sumino describes the possibility that the dislocations around inclusions act as the preferred nucleation sites for AF.¹⁵⁾

Dowling et al. have reported that inclusions contribute to the generation of AF as mere heterogeneous nuclei and the influence of inclusion species is small.¹⁶⁾

As described, many studies have been conducted on the inclusions that generate AF and on the mechanism of how these inclusions generate AF; however, most studies have been made on single phase inclusions consisting of simple, pure oxides. On the other hand, a weld metal contains a plurality of deoxidizing elements and highly enriched oxygen; hence, more complex inclusion particles are considered to be formed. In the case of such complex inclusions, the mechanism of AF generation and their relationships with mechanical properties have not sufficiently been clarified. Against this backdrop, Kobe Steel studied the complex inclusion

particles containing Mn-Ti based oxides, including their influence on the AF structure and mechanical properties, and also studied the mechanism of AF generation. An outline follows:

1. Experimental method

1.1 Weld metals

Two types of weld metals were prepared as testing materials: i.e., a Ti-free material containing low Mn and no Ti, and Ti-added material with high Mn. For welding, low carbon steel plates were prepared, each having a thickness of 25 mm and a 10°V groove. Submerged arc welding (hereinafter referred to as "SAW") was performed under the conditions of root opening, 15 mm; welding current, 425 A; voltage, 30 V; welding speed, 5.8 mm/s; and inter-pass temperature, 180 °C to 200 °C. **Table 1** shows the compositions of the weld metals. The contents of P, S, and N were lower than 0.008, 0.003 and 0.010 mass%, respectively. Some of the weld metal thus obtained was subjected to post weld heat treatment (PWHT) at 640 °C for 108 ks.

1.2 Microstructure observations

Weld metal consists of an as-welded zone, which has an as-solidified matrix structure, and a reheated zone with a matrix structure that has been changed due to the thermal influence of subsequent welding passes. The grain size of the prior austenite in a reheated zone is smaller than that in an as-welded zone and changes with the distance from the melted part of the subsequent pass. When prior austenite grains are rather small, the amount of AF generation is affected by the size of prior austenite grains.^{17), 18)} For this reason, when comparing the AF structures in the reheated zones, the difference in the grain size of the prior austenite due to different observation points must be taken into account, which is cumbersome. Hence, in the present study, microstructure observations were conducted in the as-welded zones contained in the weld metal formed during the final pass, since these zones have sufficiently large prior austenite grains. The surfaces that are vertical to the welding direction were mirror-polished for observation under an optical microscope. Photographs were taken in

two fields at 1000x magnification. The number density and the average circle-equivalent diameter of the inclusions in the photos were determined by image analysis. Due to photographic resolution, inclusions of 0.5 μm or larger, in terms of circle-equivalent diameter, were analyzed. Subsequently, the same samples were etched with 3% Nital solution and the microstructures of their matrixes were observed under the optical microscope. In addition, inclusion particles and the AF structures nucleated from these were selected, and the surface etched layers were polished off. A scanning electron microscope, JEOL JSM-6500F, was used to analyze the electron backscatter diffraction (EBSD) patterns to determine the crystal orientation of AF. A step size of 0.1 μm was selected for the EBSD measurement in consideration of the ferrite phase and austenite phase. Furthermore, transmission electron microscopy (TEM) observations were carried out using JEOL JEM-2010F to identify the phase constituting the inclusion particles that became the nucleation site for AF generation. From the observation fields that had been subjected to EBSD measurement above, the regions containing inclusion particles were picked up by the focused ion-beam system (FB2000A) and were processed into thin film samples for the TEM observation. The TEM observations were carried out at an accelerating voltage of 200 kV. In order to identify the inclusion phase, the elements constituting the inclusions were determined by the energy dispersive X-ray spectroscopy (EDS). The crystal structure was determined by the selected area diffraction pattern. In addition, Kikuchi's pattern analysis¹⁹⁾ was applied to analyze the crystal orientation relationship between the inclusion phase and AF.

1.3 Mechanical properties

The yield strength (YS) and tensile strength (TS) were examined for the weld metals in an as-welded state, which is the state not subjected to post-welding heat treatment, etc., and for the weld metals after being processed by PWHT. Each tensile test piece (JIS Z 3111, A2 type) was collected from the center of the corresponding weld metal in a direction parallel to the welding direction. In order to evaluate the impact toughness, V-notch Charpy test pieces (3 pieces), in accordance with JIS Z 3111,

Table 1 Chemical compositions of weld metals (mass%)

	C	Si	Mn	Al	Ni	Cr	Mo	Ti	O	Fe
Ti free	0.06	0.07	1.20	0.005	1.54	0.28	0.78	0.001	0.047	bal.
Ti added	0.13	0.13	1.65	0.005	1.60	0.28	0.77	0.051	0.025	bal.

were collected from the central part of each weld metal and in the welding direction so that each notch was positioned at the joining portion of the respective welding pass. Charpy impact absorbed energy, $vE_{-30^{\circ}\text{C}}$, was evaluated by the average value of the results for three test pieces at -30°C .

2. Experimental results and discussions

2.1 Microstructure and mechanical properties

Fig. 1 shows the optical micrographs of the weld metals. In the Ti-free material, a coarse bainite microstructure is observed across the field, in which the bainite microstructure has substructures, such as packets and blocks, generated from the prior austenite grain boundaries. On the other hand, Ti-added material exhibits an extremely fine microstructure. It has been observed that some of the crystal grains that constitute this fine microstructure have been generated radially from inclusion particles, as indicated by the arrow in Fig. 1(d). These are the AFs generated from inclusion particles as their nucleation sites. The fine crystal grain, which seems to exist irrespective of the inclusion particles at first glance, is presumed to be AF formed on the inclusion particle inside the weld metal, or has undergone sympathetic nucleation from the AF that was generated earlier.²⁰⁾

Fig. 2 shows the size distributions of inclusion particles in the weld metals of Ti-free material and

Ti-added material. In the Ti-free material, which contains a greater amount of oxygen, there is observed a trend for the relatively fine inclusion particles with a circle-equivalent diameter of $1.00\mu\text{m}$ or less to increase in number. On the other hand, no significant difference due to the presence or absence of Ti addition has been detected in the number density of the coarse inclusion particles exceeding the circle-equivalent diameter of $1.00\mu\text{m}$. The mean circle-equivalent diameters of inclusion particles were $0.80\mu\text{m}$ for Ti-free material and $0.83\mu\text{m}$ for Ti-added material, showing that the values are almost the same.

Table 2 shows the mechanical properties of the weld metals. In the as-welded state, the Ti-added

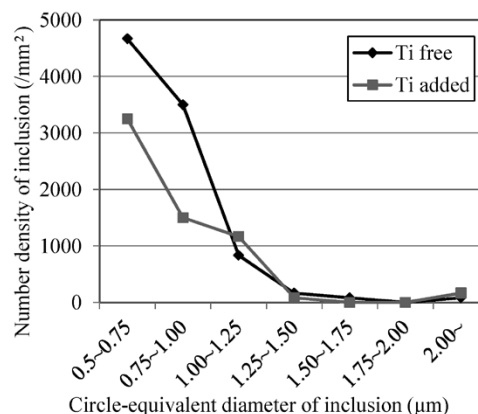


Fig. 2 Size histogram of inclusion particles in the weld metals

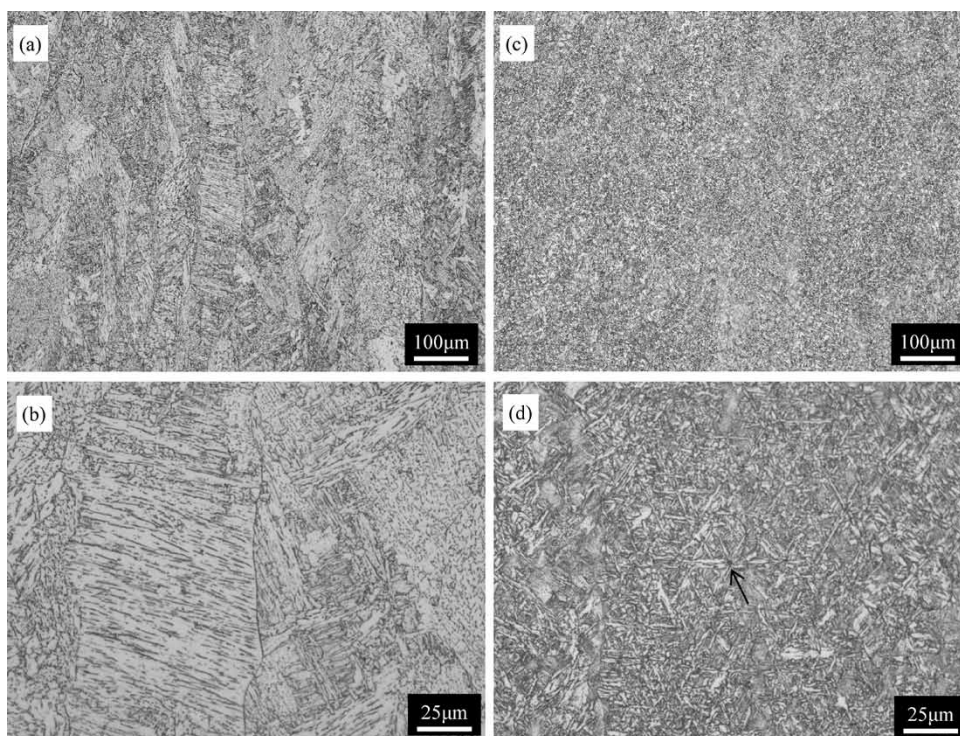


Fig. 1 Optical micrographs of the (a, b) Ti free and (c, d) Ti-added weld metals

Table 2 Mechanical properties of weld metals

	As weld			After PWHT		
	YS (MPa)	TS (MPa)	vE ^{30°C} (J)	YS (MPa)	TS (MPa)	vE ^{30°C} (J)
Ti free	580	672	53	454	575	59
Ti added	773	927	72	701	776	60

material exhibits a yield strength approximately 200 MPa higher than, and a toughness value that is substantially equal to, those of the Ti-free material. This is considered to be attributable to the microstructure refinement by the AF generated in the Ti-added material. The Ti-added material also exhibits a favorable balance of strength and toughness after the PWHT.

2.2 Mechanism of AF generation in Ti-added material

2.2.1 Inclusion phase acting as the nucleation site for AF generation

In the Ti-added material, it is worthy of note that AF has been generated from inclusions as its nucleation site. Prior austenite grain size has been reported to influence the generation of AF structure.^{17), 18)} The present weld metals have been prepared under identical welding conditions and have almost the same prior austenite grain sizes. Hence, their influence on AF generation is presumed to be negligible. The number of inclusions that act as the nucleation sites for AF generation is considered to be the product of the total number of inclusions and AF generation frequency in the individual inclusion particle; however, as shown in Fig. 2, the number of inclusion particles in the Ti-added material is smaller than that of the Ti-free material. Therefore, the inclusion particles in the Ti-added material are presumed to contain a phase that is more likely to generate AF, i.e., has a higher AF generation potential.

Fig. 3 shows an inverse pole figure (IPF) map of the field encompassing the inclusion indicated by an arrow in Fig. 1 (d) and the peripheral AF structure.²¹⁾ The black part (unanalyzable point) near the center is an inclusion particle providing the nucleation site for the generation of AF crystal grains (indicated as "AF1", "AF2" in the figure). Also observed are several crystal grains that are not in contact with the inclusion particle, but extending radially from it. These are considered to be AF generated from inclusion particles outside the observation surface, or crystal grains that have undergone sympathetic nucleation from the AF.²⁰⁾ There also are almost equiaxial crystal grains in contact with the inclusion particle. It is not clear whether these grains have

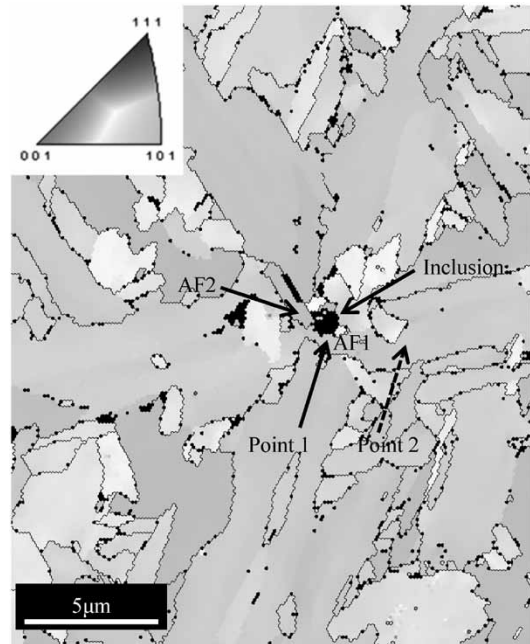


Fig. 3 Inverse pole figure map of the Ti added weld metal²¹⁾

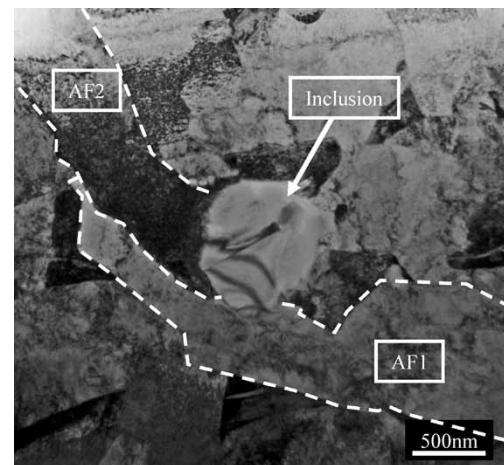


Fig. 4 Bright field image of the Ti added weld metal²¹⁾

been nucleated on the surfaces of other inclusion particles, or have grown from other nucleation sites and have touched the inclusion particle incidentally. Therefore, only two AF particles, AF1 and AF2, are confirmed to have been generated from the inclusion particle in Fig. 3.

Fig. 4 is the TEM bright-field image of the area including the inclusion particle in Fig. 3 and its surrounding matrix.²¹⁾ Once again, this confirms that the AF1 and AF2 observed in Fig. 3 have been generated from the inclusion particle as their nucleation sites. Fig. 5 is an EDS mapping of the inclusion particle.²¹⁾ The inclusion particle comprises four parts: namely (1) the part where both Ti and Mn are enriched, occupying a large area from the center to the lower left of the inclusion particle; (2) the part where both Si and Mn are enriched, surrounding the Ti and Mn enriched part; (3) the

part where Ti is enriched, as observed in the upper left of the inclusion particle; and (4) the part where Mn is enriched, as observed in the upper right and the far right of the inclusion particle. The selected area diffraction patterns (Fig. 6) have identified the fact that the part enriched by Ti/Mn, the part enriched by Si/Mn and the part enriched by Ti are MnTi_2O_4 , amorphous phase, and TiO_2 , respectively. In addition, a separately conducted EDS point analysis has detected S, indicating that the Mn-enriched part is MnS.

Comparison of these phases, constituting the inclusion particle, with the locations of AF1 and AF2 has revealed that AF1 is in contact only with the MnTi_2O_4 phase, and AF2 is in contact with the MnTi_2O_4 phase, TiO_2 phase, and amorphous phase. Also, it has been found that both AF1 and AF2 have been generated at positions away from MnS. There seem to be few reports indicating that, among the three phases in contact with AF2, the amorphous

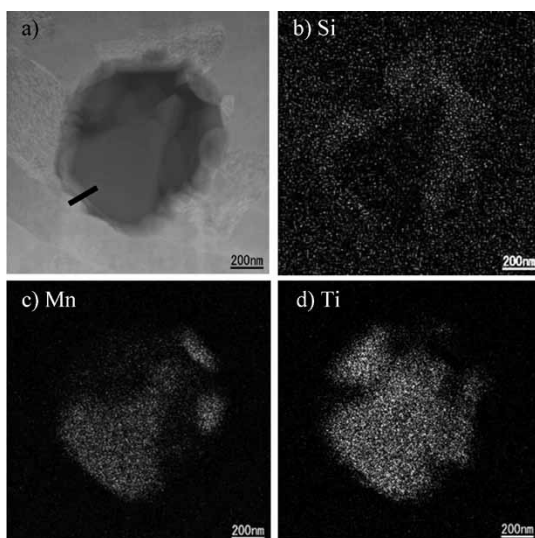


Fig. 5 (a) TEM image, (b)~(d) EDS mappings of Si, Mn and Ti of the inclusion particle observed in Fig. 4²¹⁾

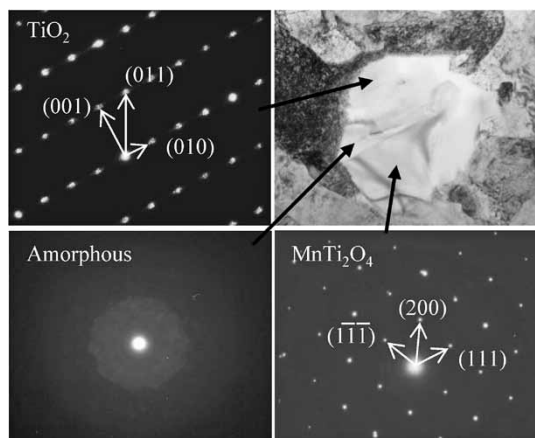


Fig. 6 Selected area diffraction patterns of the inclusion particle observed in Fig. 4²¹⁾

phase promotes AF generation. It has been reported that both the MnTi_2O_4 phase and TiO_2 phase function as the nucleation site of AF generation.^{22), 23), 10)} The fact that AF1 is in contact only with the MnTi_2O_4 phase suggests that the MnTi_2O_4 phase acts most effectively as the nucleation site for AF generation.

2.2.2 AF generation mechanism via MnTi_2O_4

The generation mechanism of AF1, which is deemed to have been nucleated on MnTi_2O_4 phase, has been studied from the viewpoints of the compositional change of the peripheral matrix and the lattice matching with AF.

Fig. 7 shows the results of measurements on the Mn and Ti concentrations along the bold line from MnTi_2O_4 to AF1 in Fig. 5(a). No Mn-depleted zone has been detected clearly, due to the unevenness of the data, on the side of AF1 and in the vicinity of the MnTi_2O_4 /AF1 interface, although the Mn concentration seems to have been decreased slightly. The formation of the Mn-depleted zone is a result of Mn diffusing from the austenite phase into the inclusions. In the case of the weld metals of the present study, it is considered that the cooling after welding has been too rapid to secure enough time for the diffusion of Mn. According to Shigesato et al.,¹³⁾ a zone in which Mn has been depleted by 0.4mass% has been detected in a sample with AF structure occupying at least 80% an area fraction. In the present study, however, the microstructure of the Ti-added material exhibits AF almost across the field, which makes it difficult to explain the AF generation on the basis of the Mn-depleted zone in the Ti-added material. Furthermore, almost no Ti, a ferrite stabilizing element, was detected in AF1.

Fig. 8 is an [101] pole figure of MnTi_2O_4 , in (100) of AF1 and MnTi_2O_4 . The figure has been obtained by analyzing their crystal orientations.²¹⁾ The $\{001\}_{\text{MnTi}_2\text{O}_4}$ and $\{001\}_{\text{AF1}}$, as well as $\langle 110 \rangle_{\text{MnTi}_2\text{O}_4}$ and

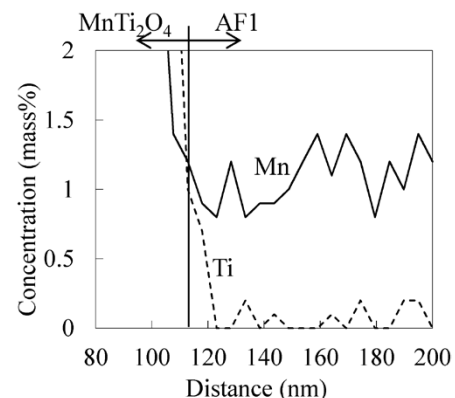


Fig. 7 Mn and Ti concentration profiles along the bold line in Fig. 5(a)

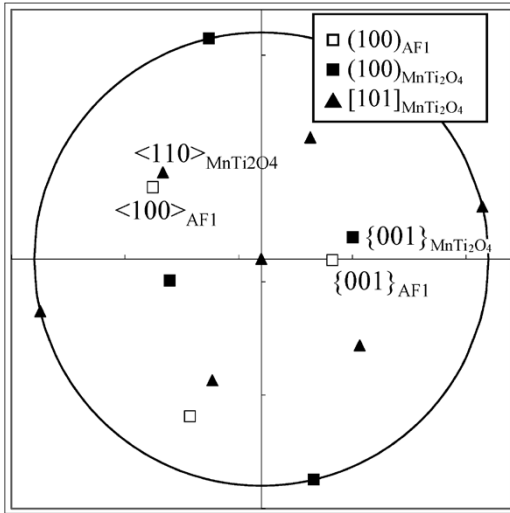


Fig. 8 Stereographic projection of the AF1 and the MnTi₂O₄ shown in Fig. 4²¹⁾

$\langle 100 \rangle_{AF1}$, are close to each other. This result suggests that the following crystal orientation relationship of Baker-Nutting (B-N relationship) holds in MnTi₂O₄ and AF1.

$$(001)_{MnTi_2O_4} // (001)_{AF}, [110]_{MnTi_2O_4} // [100]_{AF}$$

It should be noted, however, that the probability that B-N relationship occurs by chance, the probability assuming the allowable misorientation of 15°²⁴⁾ and determined by the technique of Grong et al.¹¹⁾, is relatively high at 10%; thus, it is possible that the B-N relationship has been established only by chance. Against this backdrop, the crystal orientation of AF1 has been analyzed in more detail. The (001) pole figure of the measurement area in Fig. 3 is shown in Fig. 9.²¹⁾ This measurement area is located inside one crystal grain of prior austenite, resulting in a highly symmetric pole figure roughly in accordance with the Kurdjumov-Sachs crystal orientation relationship (K-S relationship).²⁵⁾ It is noteworthy that the crystal orientation (Point 1) of AF 1 in the vicinity of the inclusion particle is displaced by 5.5° from the ideal K-S relationship. On the other hand, a crystal orientation close to a K-S relationship has been detected at Point 2, which is away from the inclusion particle in AF1. These results indicate that the AF1 nucleates with a crystal orientation slightly deviating from the K-S relationship, and has changed its crystal orientation such that it approaches the K-S relationship in the process of its growth. This is the same trend as reported by Takada et al. on the AF nucleated from TiO,²⁶⁾ and is considered attributable to AF1 nucleating preferentially in accordance with the B-N relationship. Bramfit has reported that the carbonitride, which has a planar disregistry below 12%, functions as the nucleus for the solidification of BCC iron because of their favorable lattice

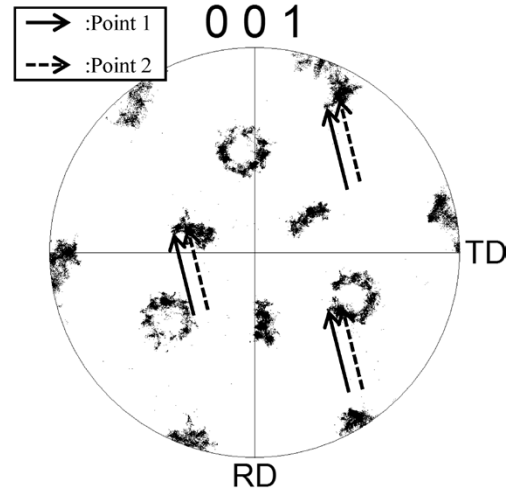


Fig. 9 (001) pole figure of the area corresponding to Fig. 3²¹⁾

matching.²⁷⁾ When the fact that MnTi₂O₄ has a cubic crystal structure with a lattice constant of 0.862 8 nm,²⁸⁾ the planar disregistry²⁷⁾ at the establishment of the B-N relationship is sufficiently low at 6.67%. From this, the fact that MnTi₂O₄, having an interface where the B-N relationship holds, is considered to have realized a favorable lattice matching with AF, facilitating the nucleation of AF.

Furthermore, it is presumed that AF retaining the K-S relationship with austenite phase has low interface energy with the austenite phase,²⁹⁾ further promoting the nucleation and growth. In the AF immediately after its nucleation, a crystal orientation close to the K-S relationship has been detected in addition to the B-N relationship. This suggests the possibility that a crystal orientation that is close to the K-S relationship may have been selected during the nucleation while satisfying the B-N relationship. The nucleation barrier energy ΔG^* when AF nucleates on inclusion is expressed by the following equations in the classical nucleation theory.

$$\Delta G^* = \frac{16\pi\sigma_{AF/\gamma}^3}{3(\Delta G_V + \Delta G_S)^2} \cdot f(\theta) \dots\dots\dots (1)$$

$$f(\theta) = \frac{(2 + \cos\theta)(1 - \cos\theta)^2}{4} \dots\dots\dots (2)$$

$$\cos\theta = \frac{\sigma_{\gamma/X} - \sigma_{AF/X}}{\sigma_{AF/\gamma}} \dots\dots\dots (3)$$

where

- $\sigma_{AF/\gamma}$: AF/austenite phase interface energy
- $\sigma_{\gamma/X}$: austenite phase/inclusion interface energy
- $\sigma_{AF/X}$: AF/inclusion interface energy
- ΔG_V : nucleation driving force, and
- ΔG_S : strain energy.

When the B-N relationship and K-S relationship are established simultaneously, the values of $\sigma_{AF/X}$ and $\sigma_{AF/\gamma}$ decrease. Therefore, it is considered that ΔG^* decreases as compared with the case where K-S and B-N relationships are established

independently,²¹⁾ facilitating the nucleation of AF.

The reason considered for the change in the crystal orientation of AF, the change that takes place as it approaches the K-S relationship during the growth process, is that this lowers the energy of the AF/austenite interface. In other words, although AF selects a crystal orientation that can predominate over both the interface energies of MnTi₂O₄ and austenite phase at the time of its nucleation, it changes its crystal orientation so that the energy of the interface becomes lower as the interface with the austenite phase increases during its growth process. From the above, it is concluded that the interface energy between AF and nucleation-site inclusions strongly affects the nucleation and growth of AF, and so does the interface energy between the austenite phase and AF.

It should be noted that both the B-N relationship between the AF and MnTi₂O₄ phase and the K-S relationship between the AF and prior austenite phase have been detected simultaneously at the time of nucleation. This suggests the possibility that, prior to AF generation, a specific crystal orientation relationship (herein referred to as the X-A relationship) has existed between the MnTi₂O₄ phase and prior austenite phase. In general, inclusions in weld metal are formed in molten iron, and the resulting crystal orientation relationship with prior austenite phase is considered to be random.³⁰⁾ This consideration leads to the interpretation that, among the MnTi₂O₄ particles with various crystal orientations, only the MnTi₂O₄ particles that satisfy the X-A relationship by chance have allowed the simultaneous establishment of B-N and K-S relationships, preferentially acting as the nucleation sites for AF. On the other hand, the above concept is based on the assumption that the inclusions generated in molten iron are solid inclusions, and if the solidification temperature of the inclusions is low, there is a possibility that a specific /non-random crystal orientation relationship may be established with the austenite phase. That is, when inclusions having existed in a liquid state at high temperature solidify in the austenite temperature region, there may be cases where the crystallization occurs with a crystal orientation relationship having a favorable lattice matching with the peripheral austenite phase. Kobe Steel's analysis²¹⁾ has revealed that a specific orientation relationship can exist between the austenite phase and MnTi₂O₄ phase. This orientation relationship achieves a relatively favorable planar discrepancy of 8.6% against the austenite phase while allowing the simultaneous establishment of K-S and B-N relationships with a deviation of 5.3° from the ideal

direction in the subsequent AF nucleation. There are many simple oxides having high solidification temperatures; however, Blais et al. have pointed out on the basis of their thermodynamic calculation that the solidification point of MnTi₂O₄ can be lower than that of steel.²²⁾ The relationships among the solidification point of inclusions and the crystal orientations of the AF, inclusions and austenite phase, as well as the relationship with the AF generation, will be the subjects of future study.

Conclusions

The generation behavior and mechanical properties of AF structures have been studied using weld metals with the dispersion of composite inclusion particles including Mn-Ti based oxide, and the following results were obtained:

- Of the plurality of phases constituting the inclusion particles, MnTi₂O₄ phase predominantly functions as the nucleation site for AF generation.
- From the viewpoint of nucleation and growth, the interface energy between MnTi₂O₄ phase/austenite phase and AF has a dominant influence on AF generation.
- Weld metals with the AF structure exhibit a favorable balance of strength and toughness.

References

- 1) M. Maki. Tekko no soshiki seigyō --Sono genri to hoho (Microstructure control of steel--Its principle and method). 1st Edition, Uchida Rokakuho Publishing Co. Ltd., 2015, pp. 125-127.
- 2) I. Watanabe et al. Journal of the Japan Welding Society (Journal of JWS). 1980, Vol. 49, No. 11, pp. 772-780.
- 3) N. Mori et al. Journal of the Japan Welding Society (Journal of JWS). 1981, Vol. 50, No. 8, pp. 786-793.
- 4) K. Yamamoto et al. ISIJ Int. 1996, Vol. 36, No. 1, pp. 80-86.
- 5) Y. Horii et al. Q. J. Jpn. Weld. Soc. 1995, Vol. 13, No. 4, pp. 500-507.
- 6) T. Hanamura et al. ISIJ Int. 1999, Vol. 39, No. 11, pp. 1188-1193.
- 7) T. Yamada et al. ISIJ Int. 2009, Vol. 49, No. 7, pp. 1059-1062.
- 8) A. R. Mills et al. Mater. Sci. Tech. 1987, Vol. 3, pp. 1051-1061.
- 9) J. M. Gregg et al. Acta Metall. Mater. 1994, Vol. 42, No. 10, pp. 3321-3330.
- 10) J. M. Gregg et al. Acta Mater. 1997, Vol. 45, No. 2, pp. 739-748.
- 11) O. Grong et al. Metall. Mater. Trans. A. 1995, Vol. 26A, No. 3, pp. 525-534.
- 12) K. Kasai et al. TETSU-TO-HAGANE. 2010, Vol. 96, No. 3, pp. 123-128.
- 13) G. Shigesato et al. TETSU-TO-HAGANE. 2001, Vol. 87, No. 2, pp. 93-100.
- 14) T. Minote et al. Iron and Steel Institute of Japan, 1995, pp. 65-74.
- 15) K. Sumino. Iron and Steel Institute of Japan, 1998, pp. 17-43.
- 16) J. M. Dowling et al. Metall. Trans. A. 1986, Vol. 17A, No. 9,

- pp. 1611-1623.
- 17) D. Zhang et al. *Acta Mater.* 2010, Vol. 58, pp. 1369-1378.
 - 18) F. J. Barbaro et al. *Mater. Sci. Tech.* 1989, Vol. 5, No. 11, pp. 1057-1068.
 - 19) S. Zaefferer. *J. Appl. Cryst.* 2000, Vol. 33, pp. 10-25.
 - 20) K. M. Wu et al. *Mater. Charact.* 2004, Vol. 52, pp. 121-127.
 - 21) H. Nako et al. *ISIJ Int.* 2014, Vol. 54, No. 7, pp. 1690-1696.
 - 22) C. Blais et al. *Sci. Technol. Weld. Join.* 1999, Vol. 4, No. 3, pp. 143-150.
 - 23) Y. Okazaki et al. *Quarterly Journal of the Japan Welding Society.* 2009, Vol. 27, No. 2, pp. 131-138.
 - 24) C. Lee et al. *ISIJ Int.* 2011, Vol. 51, No. 12, pp. 2036-2041.
 - 25) S. Morito et al. *Acta Mater.* 2003, Vol. 51, pp. 1789-1799.
 - 26) A. Takada et al. *Quarterly Journal of the Japan Welding Society.* 2013, Vol. 31, No. 1, p. 33-40.
 - 27) B. L. Bramfitt. *Metall. Trans.* 1970, Vol. 1, No. 7, pp. 1987-1995.
 - 28) Y. Huang et al. *J. Magnetism and Magnetic Mater.* 2012, Vol. 324, pp. 2075-2081.
 - 29) T. Nagao et al. *Metall. Mater. Trans. A.* 2006, Vol. 37A, No. 3, pp. 929-937.
 - 30) H. K. D. H. Bhadeshia et al. *Mathematical Modeling of Weld Phenomena.* The Institute of Materials, 1993, pp. 109-180.

Dissimilar Metal Joining Process "Element Arc Spot Welding"

Liang CHEN*¹, Dr. Reiichi SUZUKI*¹

*¹Automotive Solution Center, Technical Development Group

Dissimilar metal joining between aluminum and steel has mainly been performed mechanically, however, the method has problems such as production constraints. Hence, we have proposed element arc spot welding (EASW) as a new method for dissimilar metal joining. The new method comprises inserting a hollow steel element (rivet) into a hole in an aluminum upper sheet, after which, the molten filler metal is deposited by arc welding in the hollow part of the element; that is, the element and the lower steel sheet are firmly welded, while the upper aluminum-alloy sheet is tightly held between them. Thanks to the features of the joining mechanism, there is no restriction on the strength of the steel sheet. The method is also applicable to members with closed cross sections. With appropriate elements and welding wires, EASW can assure joint strength equal to or greater than mechanical joining. It allows welding in all positions and tolerates a gap of approximately 1 mm.

Introduction

Recently, multi-material structures, in which high-strength steel and lightweight materials such as aluminum alloy are suitably placed, are being increasingly studied and adapted in practice so as to decrease the weight of automobiles for emission reduction. Joining technologies for dissimilar materials such as steel and aluminum are key to multi-material car body design. Joining steel and aluminum alloy, however, has been considered difficult due to the differences in their physical properties, such as melting point, thermal conductivity and corrosion electric potential, and also due to the fact that the general-purpose fusion welding, such as resistance spot welding and arc welding, causes brittle intermetallic compounds to be formed. Currently, mechanical joining, such as

self-pierce riveting (SPR) and mechanical clinching, is being used; however, there are problems such as significant cost increase and production constraints. It is against this backdrop that a new method for joining dissimilar metals, namely, element arc spot welding (hereinafter referred to as "EASW"), has been proposed; this method exploits the existing technologies of arc welding and welding consumables. This paper introduces the joining mechanism and basic characteristics, including joint strength, of EASW.¹⁾⁻³⁾

1. Mechanism of EASW

Fig. 1 depicts the mechanism of EASW. Herein, the upper sheet is an aluminum alloy sheet, while the lower sheet is a steel sheet, in which the upper sheet is provided with a pre-hole. A hollow flanged steel rivet (hereinafter referred to as an "element"), is inserted into the pre-hole. Then, molten filler metal is deposited by arc welding in the hollow part of the element. That is, by performing arc spot welding from one side, the element and lower steel sheet are firmly welded, while the upper aluminum sheet is tightly held between them. It is desirable for the welding conditions to be controlled so that the weld metal protrudes slightly behind the steel sheet.

Although the EASW is a joining method using arc welding, which generates high heat, no intermetallic compound is formed because the aluminum alloy is not melted at all. It should be noted that the element can be optimally designed in accordance with the requirements for sheet thickness and/or joint strength. The time required for the welding operation is strongly affected by the sheet thickness and is roughly 0.5 to 1.5 seconds. Unlike mechanical joining, the EASW does not require the

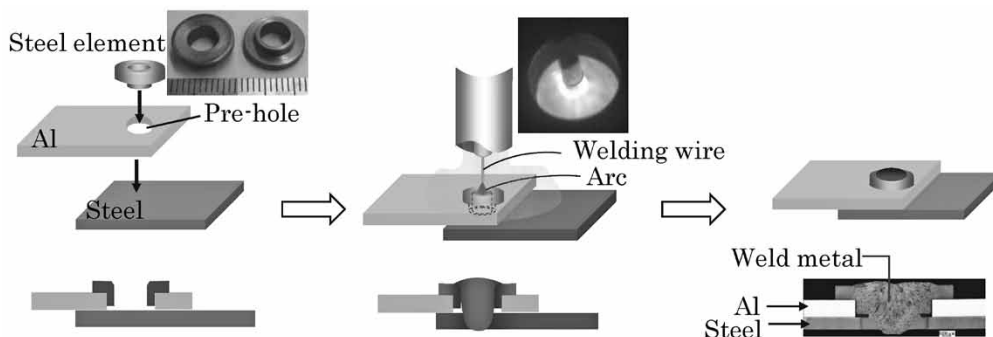


Fig. 1 Mechanism of EASW

steel sheet to be plastically deformed or penetrated; rather, the steel sheet is melted by high-temperature arc heat to form a welding joint. Therefore, there is no limit to the applicable strength of the steel sheets. There is also no need to access the subject from both sides to pressurize the upper and lower sheets. In other words, this single-side-access joining method has the advantage of being applicable, not only to open structures, but also to closed structures, as shown in Fig. 2.

2. Joint strength characteristics of EASW

The joint strength of EASW was evaluated by the tensile shear test in accordance with JIS Z 3136 and the cross tensile test in accordance with JIS Z 3137.

2.1 Study on failure mechanism of EASW joint

The following explains the failure mechanism of EASW on the basis of its structural features and analysis of the stress state of the joint during the strength test. In the schematic diagram of a tensile-shear specimen in Fig. 3, the nugget (weld metal) is pulled on its right side by the aluminum alloy sheet in the right side of the pre-hole and receives a shear force (P) and bending moment (M) during the tensile shear test. Therefore, it is believed that the fracture occurs from (i) the heat-affected zone (hereinafter referred to as "HAZ") in the right side of the lower sheet (steel sheet), (ii) the weld metal, or from (iii) the aluminum alloy sheet in the right side of the pre-hole. In other words, it is easier for the weld metal to fail when its strength is lower, or when the weld metal diameter (corresponding to the nugget diameter of resistance spot welding) is small,

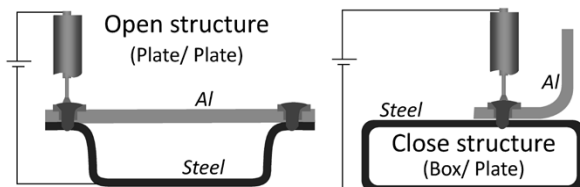


Fig. 2 Joining schematic of open/close structures

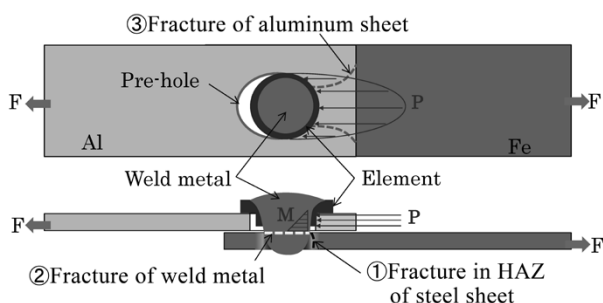


Fig. 3 Schematic diagram of specimen for tensile shear test

whereas the aluminum alloy sheet tends to fail when it is less strong, or it is thinner. In all other cases, it is believed that the lower sheet fails in its HAZ.

During the cross tensile test, as schematically depicted in the cross-sectional diagram in the longitudinal direction (the top diagram in Fig. 4), the force (P) acting on both ends of the upper aluminum alloy sheet causes the flange of the element to receive a shear force (Q) and bending moment (M). Therefore, the flange of the element may fail if it is thin and low in strength, or if the bending moment received is great (i). Alternatively, the aluminum alloy sheet may be damaged by the flange of the element, if the aluminum alloy sheet is thin with low strength (ii).

Also, as depicted in the cross-sectional schematic diagram in the longitudinal direction of the lower sheet (the bottom diagram in Fig. 4), the lower steel sheet is believed to receive a maximum bending moment in the proximity of the weld interface and is plastically deformed. For this reason, it is considered that the weld metal fails when it is low in strength (iii), and the HAZ (iv) of the lower plate or the weld interface fails when the HAZ of the lower sheet has high hardness with small elongation.

2.2 Effect of welding wire and element on joining strength

As described above, the strength of an EASW joint is affected by all of its components, namely, the material and strength of the upper and lower sheets, the strength of the weld metal, and the material and

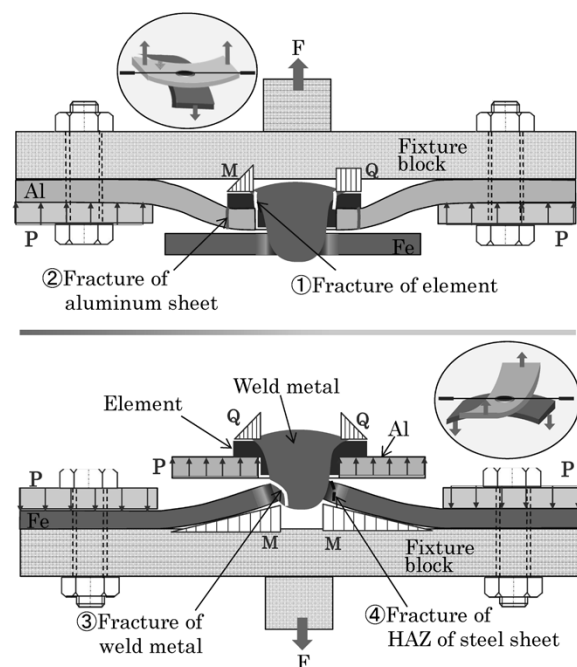


Fig. 4 Schematic diagram of specimen for cross tensile test

size of the element.

Hence, this section reports the results of the test on joining strength when the types of the upper and lower sheets are fixed. In such a case, the main controlling factors of the joining strength are considered to be (i) the strength of the weld metal and (ii) the cross-sectional area of the weld metal at the interface between the upper sheet and lower sheet. Furthermore, it is considered that (i) the strength of the weld metal is roughly determined by the welding wire, and (ii) the cross-sectional area of the weld metal at the interface is roughly determined by the hole diameter of the element and the welding conditions. As for the element, besides the hole diameter, the material and flange size affect the joining strength as described in Section 2.1. The following reports the results of the examination on the way that the type of welding wire and the size/material of the element affect the tensile shear strength (TSS) and cross tensile strength (CTS).

2.2.1 Test method

An upper sheet of aluminum alloy, A6061 (2.0 mm thick), T6 heat treated, was combined with a lower sheet of 980 MPa class high-tensile steel designed to have a dual phase microstructure (1.4 mm thick, hereinafter referred to as "980DP").^{4), 5)} Two types of welding wires (both $\phi 1.2$ mm) were used: i.e., JIS Z 3312 YGW11 (490 MPa class) and JIS Z 3312 G 59J 3M1T (590 MPa class). Two elements, having hole diameters of $\phi 5.0$ mm and $\phi 6.0$ mm respectively, were prepared using a steel in the strength class of 450-650 MPa. The shielding gas was

a mixed gas of 80%Ar+20%CO₂. In order to minimize spattering, the welding power was controlled by a high-accuracy feed control mode, in which the wire was fed forward and backward repeatedly.

2.2.2 Effect of welding-wire types and inner element diameter

The effects of the strength class of welding wires and of the interface cross-sectional areas of the weld metals on the TSS and CTS were examined, and the results are shown in Fig. 5. The elements were sized as shown in the figure, and were made of one type of material, SM490A (tensile strength: approximately 550 MPa). For the combinations of sheets in this test, the high-strength class wire resulted in both higher TSS and higher CTS. An element with a greater hole diameter also resulted in a greater interface cross-sectional area of the weld metal, leading to both higher TSS and CTS. With regard to the failure position, the TSS specimens based on the welding wire of 490 MPa class all failed in the weld metal at their sheet metal interfaces (part ② in Fig. 3), while the CTS specimens all failed in the weld metal (part ③ in Fig. 4). On the other hand, the TSS and CTS specimens based on the welding wire of 590 MPa class both failed in the HAZ of the steel sheets (part ① in Fig. 3 and part ④ in Fig. 4). From these results, it can be inferred that failure tends to occur from the weld metal when the strength of the weld metal is low, while failure tends to occur from other parts, such as the HAZ of the lower sheet, when the strength of the weld metal is sufficiently high.

2.2.3 Effect of element material on joining strength

The tests in the previous section have used elements all made of 550 MPa class strength steel, and no element damage was seen for any of the testing conditions. This section confirms the effect of elements made of different materials on the joining strength. Three types of elements, each having a hole diameter of $\phi 6.0$ mm, were made of three types of steel, i.e., 450 MPa class, 550 MPa class and 650 MPa class strength, respectively. Only one type of welding wire, JIS Z 3312 G 59J 3M1T (590 MPa class) was used, and the other conditions were the same as in 2.2.1.

The joining-strength was tested on the elements of the respective strength classes, and the results are shown in Fig. 6. These test results show no effect of the element strength on the TSS. In the case of the cross tensile test, on the

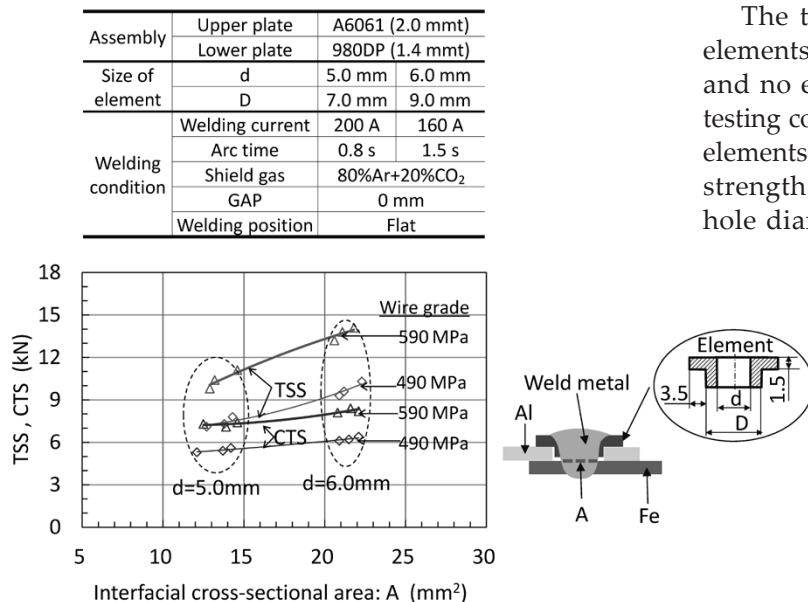


Fig. 5 Effect of welding wire and hole diameter of element on strength of joint

other hand, the element with a low strength, 450 MPa class, failed in the flange (part ① in Fig. 4), resulting in a low CTS. When the strength of the element is sufficiently high (550 MPa in this test), the position of failure shifted to the HAZ of the lower sheet, improving the CTS. It should be noted that the element with even greater strength (650 MPa in this test) led to the same result, failing in the HAZ of the lower sheet. In other words, an element with sufficient strength shows no further improvement in the CTS because its HAZ dominates the joining strength.

2.2.4 Effect of element's flange width

As described in the previous section, when the strength of the element itself is low, at the 450 MPa class, the flange of the element fails during the cross tensile test, resulting in a low CTS. It is believed that the failure of element's flange is caused by bending moment. The bending moment received is considered to change with the width of the flange. In other words, it is believed that the deformation and failure mode of a flange changes depending on the width of the flange, affecting the CTS, even if the strength classes of the elements are the same. Fig. 7 shows the results of the test on the joining strength when the width of element flanges is changed. The material of the elements used for this test is SS400 (tensile strength 450 MPa), and three flange widths of 2.0 to 3.5 mm were chosen. When the flange width was 2.0 mm, the lower sheet failed in its HAZ, but, when the flange width was 2.7 mm or 3.5 mm, the flange of the element failed, resulting in a low CTS. Furthermore, the CTS was lower for the flange width of 3.5 mm compared with that of 2.7 mm. This may be attributed to the fact that an element with a small flange width is subjected to a smaller bending moment. On the other hand, the effect of the flange width on TSS has not been confirmed. In the cross tensile test, the smaller the flange width of

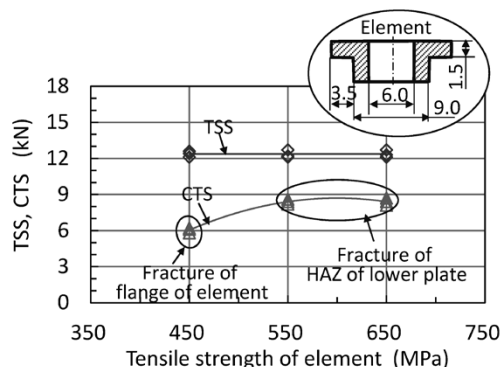


Fig. 6 Effect of tensile strength of element on strength of joint

an element, the higher the resulting CTS. However, if the flange width is too small, the pre-hole may expand in association with the plastic deformation of the aluminum alloy sheet, raising a concern that the element and weld metal may fall from the pre-hole. In addition, the flange of such an element may be melted by the heat of arc, making it impossible to engage the aluminum alloy sheet between the element flange and steel sheet. This suggests that an optimum width exists for a flange.

2.3 Comparison of joining strength in EASW and in other existing methods for joining dissimilar materials

By choosing appropriate welding consumables and elements, EASW can achieve a joining strength higher than the existing methods for joining dissimilar materials. In one example of the test, joints were prepared using an aluminum alloy, 6K21 (a Kobe Steel product equivalent to AA6022), 2.0 mm thick, and a 980 DP steel sheet, 1.4 mm thick, joined by EASW and various other existing methods for joining dissimilar materials. Fig. 8 shows the results of the shear tensile test and cross tensile test. The methods of joining dissimilar materials that were used for comparison are self-pierce riveting (SPR), Tuk Rivet®, Flow Drilling Screw (FDS®), Impulse Accelerated Tacking (ImpAcT) and Friction Element Welding (FEW). The rivet size and the joining conditions were in accordance with the manufacturers' recommendations. It should be noted, however, that the SPR and FDS® were unable to penetrate the 980 MPa steel sheet, rendering joining impossible. Hence, this figure shows reference values for the joining strength data when high-tensile strength steel sheets of 590 MPa class are used. Compared with the joining methods whose joining force relies only on friction resistance or swage structure, EASW and FEW,

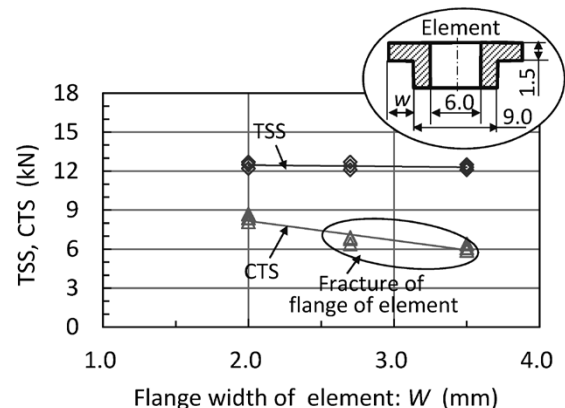


Fig. 7 Effect of flange width of element on strength of joint

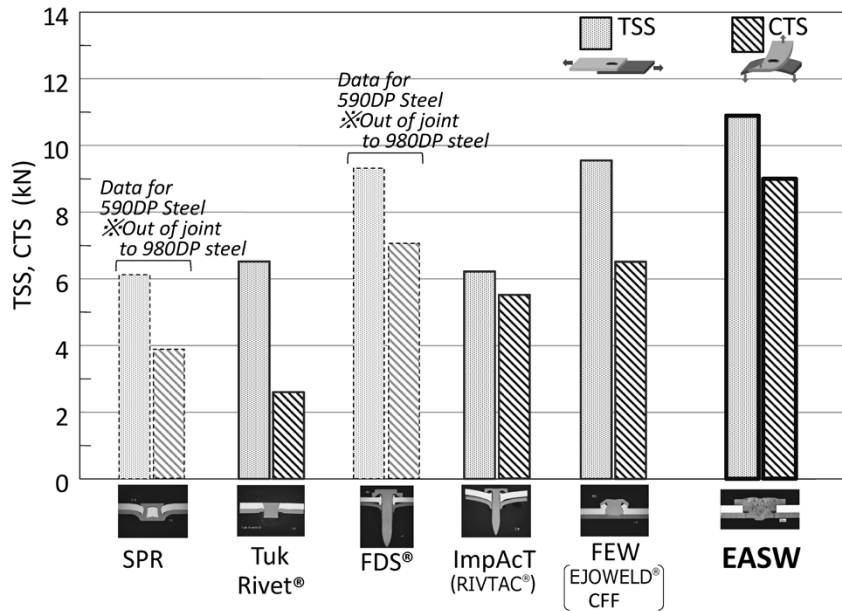


Fig. 8 Strength comparison of dissimilar metal joints

whose joining mechanisms include metallic bond achieved by welding, result in higher TSS and CTS. In particular, EASW yields high values. The reason is considered to be the fact that, although both are welding methods, arc welding and pressure welding have differences in the soundness of the joining interface, weld metal quality and heat input, which affects their peeling strength characteristics.

3. Robustness of EASW

Some existing mechanical joining methods may be constrained by the strength of the steel sheet, the cross-sectional shape of the structure to be joined, gap, joining positions, etc. In Section 1, describing the mechanism of EASW, it has been explained that EASW has few constraints on the strength of the steel sheet and the cross-sectional shape of the structure to be joined. This section explains the tolerance of the effective range of welding conditions, the range necessary for applying EASW in production sites, or so-called robustness.

3.1 Gap tolerance of EASW

At production sites, gaps may be generated between the joining objects of aluminum alloy sheet and steel sheet, due to the assembly accuracies of parts and processing accuracy, etc., and it is difficult to completely eliminate these gaps. Since excessively large gaps render joining difficult, the gap tolerance of EASW was investigated. The shapes of welding joints were evaluated in combinations of an upper sheet made of aluminum alloy A6061 (2.0 mm thick, fixed sheet thickness) and a lower sheet of DP 980

steel, while changing the thickness of the lower sheet from 0.5 to 2.0 mm and the gap from 0 to 2.5 mm. The shielding gas was a mixture of 80% Ar+20% CO₂, and three kinds of elements with hole diameters of ϕ 3.8 mm, ϕ 5.0 mm and ϕ 6.0 mm, respectively, were prepared.

Fig. 9 shows the results of the test. When the lower sheet is thin, and a gap exists, the lower sheet becomes more prone to burn through. By using an element with a small hole diameter, the arc heat can be removed by the element, limiting the amount of heat transmitted to the lower sheet, which makes it possible to suppress the burning-through of the lower sheet. Meanwhile, a thicker lower sheet has a greater resistance against burn-through, increasing the gap tolerance. When the hole diameter of the element becomes too small, however, the lower sheet becomes difficult to melt, making it impossible to form a sound nugget.

These test results confirm that a lower sheet in the thickness range of 0.5 to 2.0 mm can be welded with a gap of up to approximately 1.0 mm, if an element with the appropriate hole diameter is used. There is also the possibility that the gap tolerance could be further expanded by taking measures such as making the shielding gas Ar rich, or narrowing the wire diameter.

3.2 Compatibility with welding positions of EASW

In each of the above tests the welding position was flat. However, at production sites, the welding position depends on the shapes of structures, etc., and may not necessarily be flat. Welding is required to be compatible, not only with a horizontal flat

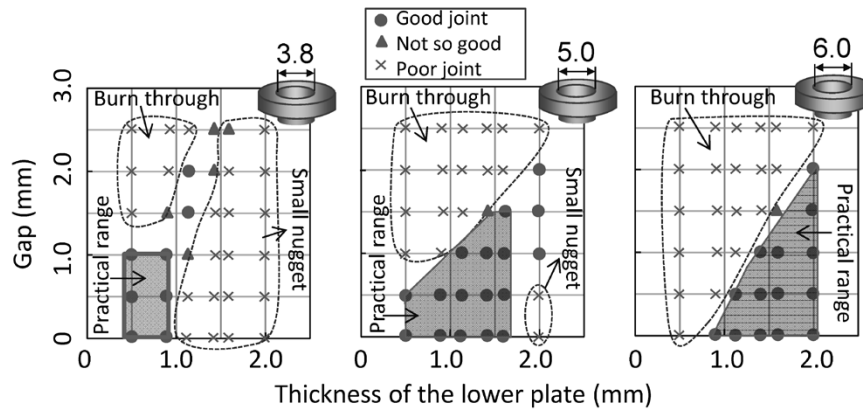


Fig. 9 Test results of gap tolerance by thickness of the lower sheet

position, but also with any other positions, including inclined or vertical ones. Fig.10 exemplifies EASW conducted in various positions. This confirms that EASW is compatible, not only with flat positions, but also with all positions, including those that are vertical and overhead. In general, arc welding using solid wires suffers from difficulty in vertical and overhead welding because the molten metal tends to drop due to gravity. EASW also uses arc welding with solid wire; however, it is compatible with welding in all positions. This has been enabled by incorporating a welding apparatus with a highly-accurate wire-feed control for repeated forward and backward feeding in which the wire tip and molten pool come in contact approximately 80 times per second, such that the small hole in the element can be filled in a very short period of approximately 1 second. The phenomenon of the molten part (droplet) of the wire tip being transferred into the molten pool by surface tension while the droplets are being positively brought into contact with the pool is referred to as short-circuit transfer and is capable of preventing the fall-off of the droplets due to gravity.

3.3 Robustness of wire aiming positions

EASW is based on the principle of depositing molten filler wire into the through-hole of an element by arc welding; hence, it is most desirable for the wire to be positioned at the center of the hole. In production sites, however, it is difficult to position the wire at the center of an element all the time, due to the curling of the wires and minute deviations of welding positions in the structure to be welded. Hence, an investigation was carried out to find the tolerance of positional deviation of wires from the center of an element.

An upper sheet (2.0 mm thick) of aluminum alloy A6061 was combined with a lower sheet (1.4 mm thick) of DP 980 steel, and an element having a hole with a diameter of $\phi 6.0$ mm was used. A welding

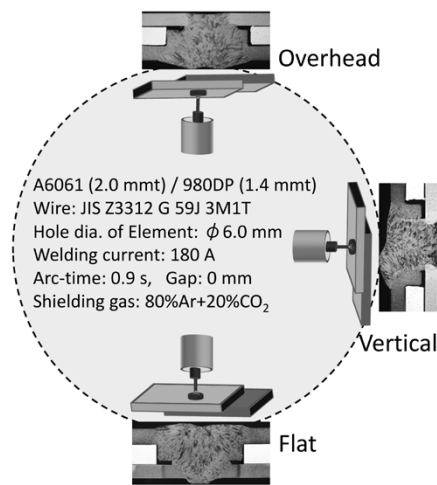


Fig.10 EASW in all position welding

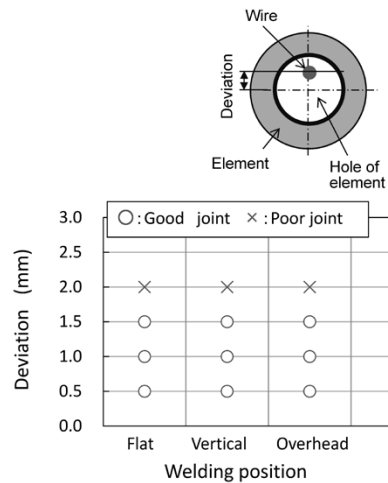


Fig.11 Relationship among appearances of welding joints, welding positions and deviation of wire tip

joint was formed with a gap of 0 mm, while the aim position of the wire was deviated. The evaluation results of the resulting appearance are shown in Fig.11. A welding joint with a favorable appearance was obtained for each of the welding positions, as long as the deviation of the aim position of the wire from the center of the hole of the element was no greater than approximately 1.5 mm.

4. Corrosion resistance of EASW welding joint

Dissimilar metal joining has issues not only of joining strength, but also of galvanic corrosion (dissimilar metal contact corrosion). Galvanic corrosion (hereinafter simply referred to as "corrosion") is a corrosion phenomenon that occurs when dissimilar metals are brought into contact with electrolyte solution as shown in Fig.12. In general, a metal with a base potential becomes the anode and corrodes faster than when it is placed alone. On the other hand, a metal with a noble potential on the cathode side generally corrodes slower than when it is placed alone, so-called cathodic corrosion prevention phenomenon. When aluminum in an electrolyte solution comes in contact with iron, which is a more noble metal, for an extended period of time, a local cell is formed, in which the aluminum ionizes and dissolves into the solution. The remaining electrons move through the aluminum alloy-iron and are released into the solution from the surface of the iron, a noble metal, generating hydroxide ion from the water and oxygen in the solution.⁶⁾

The most effective means of preventing corrosion is to prevent the contact points from being exposed to a wet environment. The practical measures for this purpose are to apply adhesives before the joining and, furthermore, to apply electro-deposition and sealing after the joining. Hence, the corrosion of the contact interface between aluminum alloy sheet and steel sheet has been investigated with

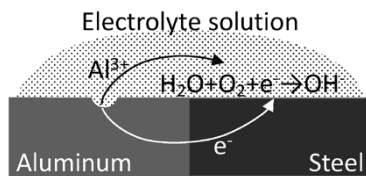


Fig.12 Mechanism of galvanic corrosion

and without the application of an adhesive. The specimen consisting of an upper sheet, aluminum alloy 6K21 (2.0 mm thick), and a lower sheet, a bare sheet (1.4 mm thick) of ultra-high-tensile 980DP steel, was prepared with a prototype element made of SS400 steel. No surface treatment such as plating was provided. The corrosion test was conducted in accordance with the JASO M 609-91 CCT standard. Fig.13 shows an example of the corrosion test results for a specimen coated with adhesive on the contact interface between the aluminum alloy sheet and steel sheet and a specimen without coating.

When there is no adhesive, corrosion occurred on the contact interface between the aluminum alloy sheet and the steel sheet. No significant corrosion was observed when an adhesive (DOW Chemical Betamate 1630, insulative) had been applied to the contact interface between the aluminum alloy sheet and the steel sheet.

On the other hand, no adhesive can be applied to the contact interface between the element and aluminum alloy. For this reason, there was some corrosion observed, although it was lighter in extent than the corrosion on the contact interface (without adhesive) between the aluminum alloy sheet and the steel sheet. Countermeasures were considered, approached from the point of view of (i) surface treatment and (ii) size of the element: (i) For the surface treatment, we considered plating the element with a metal having an electrical potential close to that of the aluminum alloy, or applying heat resistant insulation paint to the contact surface between the aluminum alloy sheet and element. (ii) As for the size of the element, it is believed that the anti-corrosion effect increases when the flange of the element in contact with the aluminum alloy sheet is minimized. This is because the corrosion of the aluminum alloy is expected to decrease as the area of steel decreases relative to the area of aluminum alloy. The feasibility and validity of these measures

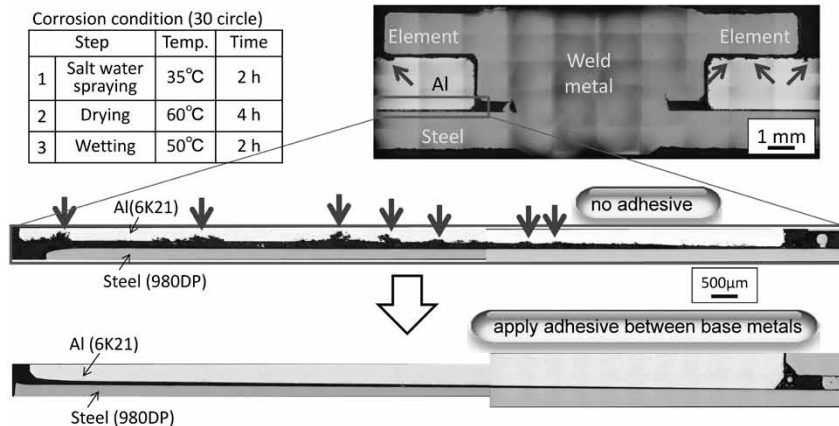


Fig.13 Results of corrosion tests with/without adhesive

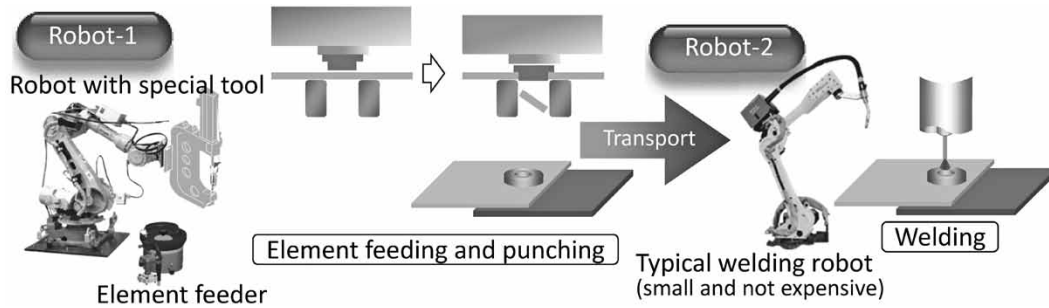


Fig.14 Conceptual diagram of 2 Robot/ 2 Step-type system for automatic EASW

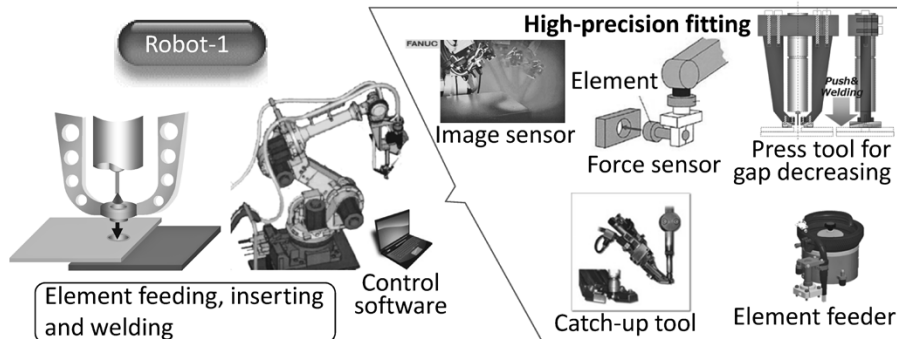


Fig.15 Conceptual diagram of 1 Robot/ 1 Step-type system for automatic EASW

must be confirmed by future tests.

5. Automatic system for EASW

Implementing EASW in the factory production process essentially requires its automation using robots. The automation of EASW is a step for future development, and this paper introduces two possible scenarios although this deviates from the purpose of introducing basic principles and effects.

A two-robot/two-step type system (Fig.14), in which the element insertion and arc welding are separated, is based on readily available fundamental technologies and easier to implement. This system allows simultaneous pre-hole formation and element insertion. This system has already been utilized in resistance element welding (REW), in which punching, and swage fastening is performed with the first robot tool using an element. The system is relatively large, being equipped with a pressurizing tool. The second robot performs standard arc welding. An inexpensive compact robot specified for arc welding can be applied as it is. It is also possible to carry out the 1st step and the 2nd step in separate factories or in separate companies. The drawback of this system is that one side accessibility, a major advantage of EASW, cannot be realized with the first robot.

Meanwhile, a one-robot/one-step type system (Fig.15) is more difficult to develop, but should perform joining highly efficiently with one compact robot. Although this system carries out all the

functions of element feed, position correction, insertion, base material pressurization and arc welding with one robot, it is a prerequisite that the pre-hole formation be provided by other means. The step that is in general considered to be the most difficult is inserting an element into a pre-hole, which inevitably involves a positional deviation. It is an extremely easy task for human eyes, but a robot requires a sensor with high accuracy. In recent years, however, the development of sensor technology has been remarkable, as represented by the prevalence of in-vehicle sensors, and robot-mounted sensors are also exhibiting high functionality. It is already possible to perform the mating process with high accuracy, and this technology should enable the reliable insertion of the elements. The pressurization of base materials is a function that reduces the root opening between base materials. Unlike resistance welding, which requires zero gaps for joining, no strong pressurization function is required.

Conclusions

An element arc spot welding method (EASW), based on arc spot welding, has been developed as a method for joining dissimilar metals of aluminum alloy and steel. Its advantages include the following:

- (i) Being a single-side access joining method, EASW can be applied to a wide range of structural shapes, such as closed cross-sectional shapes and open cross-sectional shapes.

- (ii) There is no restriction on the applicable steel sheet strength.
- (iii) A high joining strength can be obtained.
- (iv) Relatively inexpensive and compact arc-welding robots can be used.

We will continue to work on the development of practical equipment in cooperation with the manufacturers of robots and equipment, as well as with system integrators.

References

- 1) R. Suzuki. Welding technology. Vol.65 (2017-1), p.71.
- 2) R. Suzuki et al. Joining in Car Body Engineering 2017. Module 2, Automotive circle, pp.225-242.
- 3) L. CHEN et al. Abstracts of Spring Meeting 2017, Japan Welding Society. No.218, pp.78-79.
- 4) Y. Omiya et al. R&D Kobe Steel Engineering Reports. 2007, Vol.57, No.2, p.2.
- 5) T. Tamura et al. R&D Kobe Steel Engineering Reports. 2002, Vol.52, No.3, p.6.
- 6) Journal of light metal welding. 2009, Vol.47, No.3, pp.33-34.

Tire Uniformity Machine, LIBROTA®

Shinichiro IKAI*¹, Yasuhiro MATSUSHITA*²

*¹ Machinery Business Industrial Machinery Division Industrial Machinery Department

*² Machinery Business Industrial Machinery Division Electrical & Control Systems Section

Tire uniformity machines are used to inspect the quality of automotive tires. Two capabilities are emphasized, i.e., the measurement repeatability expressed by the variation of measurement values when a tire is measured several times and the cycle time for inspecting each tire. There are various restrictions in reconciling these two, and we have reconsidered the structure of mechanical parts, including spindle and drum, and the control component of the machine. As a result, it has become possible to shorten the cycle time to 18 seconds, 10% faster than before, while improving the measurement repeatability to $RFV\sigma \leq 1.69$ N. This paper reports the outline of the technology introduced for improving the measurement repeatability and cycle time performance.

Introduction ¹⁾

In 1967, Kobe Steel began the production and sales of tire uniformity machines (hereinafter referred to as "TUMs") for inspecting the quality of tires for passenger cars, trucks and buses. Since then, the company has sold over 800 units. The company's TUMs have been sold mainly in Japan and Southeast Asia so far, and, to win the leading spot, there has been a need to commercialize new TUMs applicable everywhere, including China, Europe, and the U.S., the markets currently dominated by competitors.

In a TUM, two capabilities are emphasized, i.e., measurement repeatability (σ), which evaluates the reliability of measurement when a tire is measured several times and is expressed by the variation of measurement values, and cycle time, which is the time required for inspecting each tire. In order to surpass competitors in these two capabilities and win the leading spot, Kobe Steel engaged in the development and, in 2013, commercialized a new TUM, "LIBROTA® note 1." The appearance and basic specifications of Librota are shown in Fig. 1 and Table 1, respectively.

This paper describes the steps taken to improve Librota's measurement repeatability and, at the same time, to shorten the cycle time.

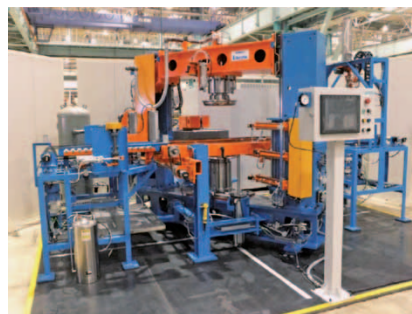


Fig. 1 New tire uniformity machine (TUM): LIBROTA®

Table 1 Base specifications of LIBROTA®

Tire size (bead diameter)	12~28 inch
Tire outside diameter	ϕ 500~ ϕ 1,020 mm
Tire test load	MAX. 18,000 N
Drum size	ϕ 854×406 mm
Repeatability (standard deviation)	1.69 N (215/60R16)
Cycle time	18 s (16 inch)

1. Features of Librota

There are two indicators that show the uniformity of a tire: the radial force variation (RFV), showing how much the force fluctuates in the radial direction of a tire when it rotates with a radius while receiving a load, and the lateral force variation (LFV), showing how much the force fluctuates in the lateral direction during the same action. A TUM is an apparatus for measuring the RFV and LFV (Fig. 2).

Conventionally, the tires for passenger cars, sized 13"-18" in diameter, and the tires for light trucks, sized 15"-24" in diameter, could not be measured on one machine. Librota, on the other hand, has a basic structure that has been significantly modified to widen the range so as to enable the measurement of tires sized 12"-28". In addition, its easy-to-understand operational interface, which introduces a schematic diagram of the machine on the operation screen, permits intuitive and reliable operation. Fig. 3 shows the main screen.

Uniformity measurement is conducted in accordance with the operating conditions specified in a recipe prepared for each type of tire. The recipe selection allows the measurement of various types of tires. These recipes are important in making accurate measurements, and their preparation requires high

note 1) LIBROTA is a Kobe Steel's trademark registered in the U.S. Librota is also a trademark registered in Japan (No. 5257882). Hereafter, it is simply referred to as "Librota" in this paper.

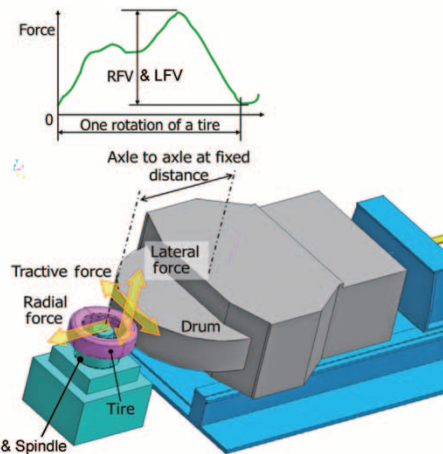


Fig. 2 Measurement mechanism of tire uniformity

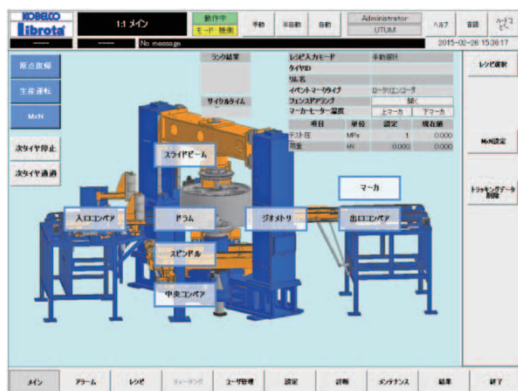


Fig. 3 Main operation screen of LIBROTA®

expertise.

Librota is equipped with a semi-automatic mode to facilitate and ensure the preparation of these recipes. In the semi-automatic mode, parameters are recorded in a recipe for each operation block while tires are being processed in the same manner as in the automatic operation. Preparing a recipe while confirming the same work as the automatic operation facilitates the setting of the optimum conditions of the operation. Maintenance and troubleshooting can also be executed from this screen, making the screen more user friendly.

On the performance side, the goal was set to achieve the repeatability and cycle time of $\sigma \leq 1.69$ N and 18 seconds or less, respectively, which exceed the values for previous machines, RFV $\sigma \leq 2.4$ N, cycle time and 20 seconds, and to surpass the competitors. One of the challenges in attempting to achieve the trade-off of improving measurement repeatability and shortening cycle time was to stabilize the tire pressure in as short a time as possible.

2. Measurement repeatability

In order to improve the measurement

repeatability of a TUM, the following three points are known to be important for the principal measurement part shown in Fig. 2:

- (1) Reducing "rim vibration," which affects the variations in rotational runout;
- (2) Reducing "drum vibration," which affects the variations of the reaction force from the tire; and
- (3) Reducing the "inner pressure variation," which affects the variation of the spring constant of the tire.

This section describes the technology adopted to reduce the influence of these factors to achieve the target measurement repeatability.

2.1 Rim vibration²⁾

Reduction of rim vibration is required to show a significant improvement in accuracy in comparison with that of Kobe Steel's previous machines. Since it turned out to be difficult to achieve the target with the mere improvement of the conventional technologies, a new approach was studied.

The previous TUM spindles use tapered roller bearings for retaining the radial direction during low-speed rotation and for holding the high load in the axial direction caused by the tire pressure after the upper and lower spindles are fastened. In developing Librota, a study focusing on the spindles for machine tools was conducted with the intention of employing high accuracy angular bearings. In the case of previous machines, the introduction of air inside the tire at the beginning of each test generates a separating force that acts to move the upper and lower spindles apart. This force acts on the tapered roller bearing on one side of the tire, reducing the preload on the bearing on the other side of the tire and weakening the restraining force against runout in the radial direction.

In order to solve this problem, an attempt was made to suppress the runout in the radial direction by placing, on the other side of the tire, an angular bearing that can maintain the retaining force in the radial direction even when the axial load is applied. In general, placing a bearing that receives the separating force near the tire can retain the separating force more effectively. For this reason, a pair of tapered roller bearings is arranged in the upper and lower spindles so that the tapered rollers face each other on the side with the smaller rotating radius. More specifically, a high-load/high-accuracy spindle (Fig. 4) was devised, in which angular bearings and tapered roller bearings are combined.

A prototype spindle with this structure was made to confirm that the rim vibration can be reduced to

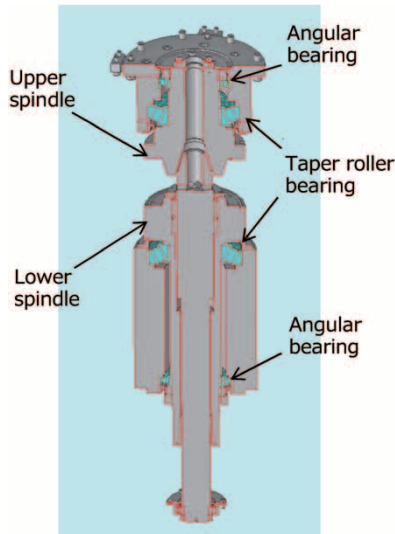


Fig. 4 Spindle structure

one-fifth of that of the conventional machines.

2.2 Drum vibration

In addition, a significant improvement in accuracy, compared with that of previous TUM drums, needed to be made in drum vibration to achieve the target repeatability. For this reason, the issue was approached from the angles of structure and manufacturing technology.

2.2.1 Drum structure

Previous machines employ bearings with tapered rollers, and the axial load received by the drum is rather small. Librota, on the other hand, employs bearings that have been changed to an angular type, the same type as adopted in the spindle, to reduce the vibration of the drum.

Moreover, its rib structure was completely revised to minimize the amount of drum deformation when the load is applied to the tire.

2.2.2 Manufacturing technologies

A drum requires a drum shaft that serves as the rotating axis. The drum shaft is fitted with a load cell for detecting the reaction force from each tire. In the case of Librota, a jig was devised to finish the drum shaft with high accuracy and to reduce the runout of the drum shaft itself. For the drum, the circumference polishing process to finish the shape was revised.

A prototype drum (Fig. 5) incorporating these measures of drum vibration reduction was made to verify that the drum vibration had been reduced to less than half of that of previous machines.

2.3 Variation of tire pressure

The tire pressure must be stabilized as much as possible during the tire measurement. In order to improve the measurement repeatability, during the inspection, we aimed at keeping the pressure fluctuation of tires within 0.05% of the set tire pressure of 200 kPa.

2.3.1 High-speed control

The electromagnetic valves used for the air circuit shown in Fig. 6 were chosen to respond to input signals faster than the previous machines. In addition, the electric pneumatic (EP) regulators and pressure sensors used for the tire pressure control were selected on the basis of their excellent accuracy and repeatability. Moreover, the high-speed control cycle of the controller has improved the pressure repeatability, reducing pressure fluctuation during the test. In the end, the control cycle necessary to stabilize tire pressure was found.

2.3.2 Measures against electric noise

A TUM uses a number of servo motors for

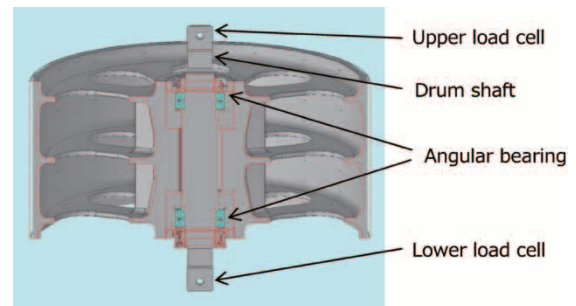


Fig. 5 Drum structure

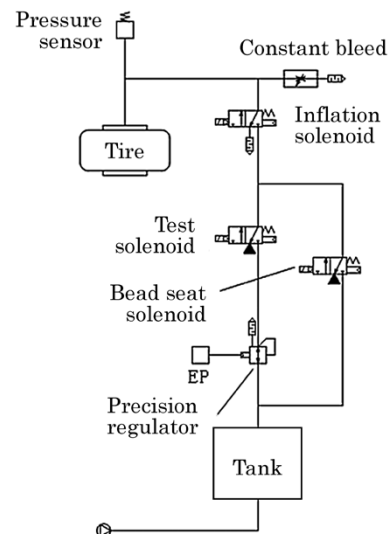


Fig. 6 Air circuit for tire inflation

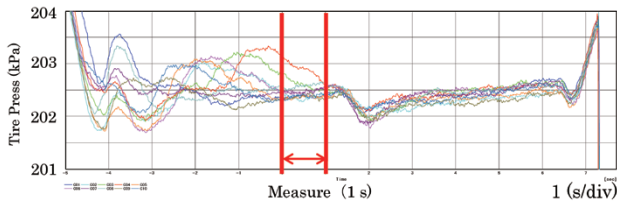


Fig. 7 Tire pressure before noise reduction

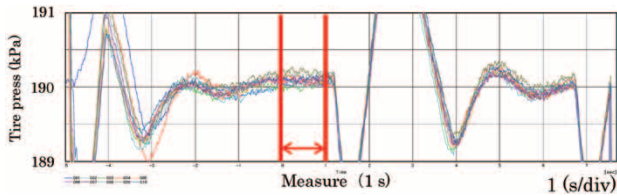


Fig. 8 Tire pressure after noise reduction

machine operation. It was found that the electric noise generated from these servo motors adversely affects the control of tire pressure. As shown in Fig. 7, mixed noise makes it difficult to suppress the fluctuation of inner pressure to within 0.05% of the set value. To this end, a study was conducted to reduce the noise generated from the servo motors and to prevent the noise from intruding into the control equipment.

As a result of implementing various measures that were required, it was confirmed that the tire pressure variation at the time of inspection had been decreased to allow the pressure to be controlled within 0.05% of the parameters, as shown in Fig. 8.

3. Cycle time

Passenger vehicle tires produced at tire factories are subjected to 100% inspection, and thus the shortening of cycle time is directly linked with productivity improvement. Therefore, a TUM is required to operate with as short a cycle time as possible.

3.1 Downsizing of machine³⁾

In the development of Librota, the working strokes and weight of the apparatus were reviewed in pursuit of thorough downsizing. The revision of the elevation mechanism of the spindle is an example. In the measurement zone of a TUM, a function for raising and lowering the spindle is required to chuck the tire with the rim. Kobe Steel's previous TUMs and those of competitors use hydraulic power to raise and lower the spindle. Librota has a structure in which ball screws arranged in the left and right guide frames are synchronically controlled by their respective servo motors to raise and lower the upper spindle. The separating

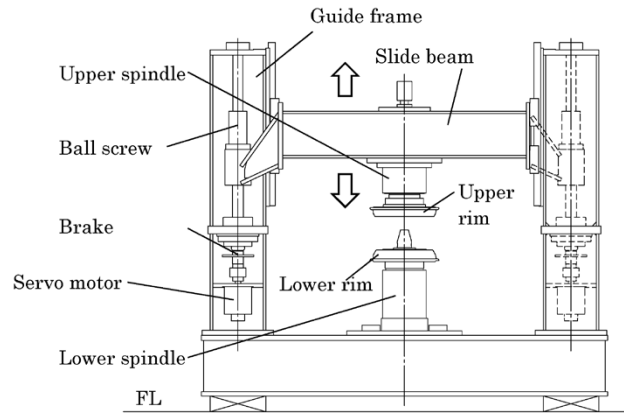


Fig. 9 Mechanism of spindle elevator

force caused by tire pressure is retained by a brake mechanism. Fig. 9 shows the elevating mechanism of the spindle in Librota. This structure has increased the ascending and descending speed of the spindle and thus shortened the cycle time. Moreover, the use of servo motors has eliminated the need for a hydraulic system, facilitating maintenance. Furthermore, without the risk of oil leakage, it is now possible to install the spindle lifting/lowering unit on top of the machine. This has successfully eliminated the need for a floor pit.

The revision of these mechanical structures has led to the reduction of the occupied volume to approximately 30% of that of the previous machines.

3.2 Adopting high-speed controller

As shown in Fig. 10, the operation of the machine follows the program in the controller, which repeats the sequence of the status check (thick horizontal line) and action (shaded box). Here, the delay time due to the fieldbus communication cycle consists of:

- the time from the detection of the actual state to the detection of the condition by the controller and
- the time from the operation command by the controller to the actual start of the operation.

The TUM operation related to cycle time includes hundreds of status checks and actions, which leads to cycle time delay for the number of fieldbus communication cycles. The cycle time is also affected by the processing capacity of the controller CPU, which influences the program execution speed.

Therefore, a decision was made to construct a control unit with a controller capable of high-speed processing with a short task cycle and a high-speed communication fieldbus with a short communication cycle (Fig. 11).

Performance evaluation by a breadboard test confirmed the cycle time of 18 seconds.

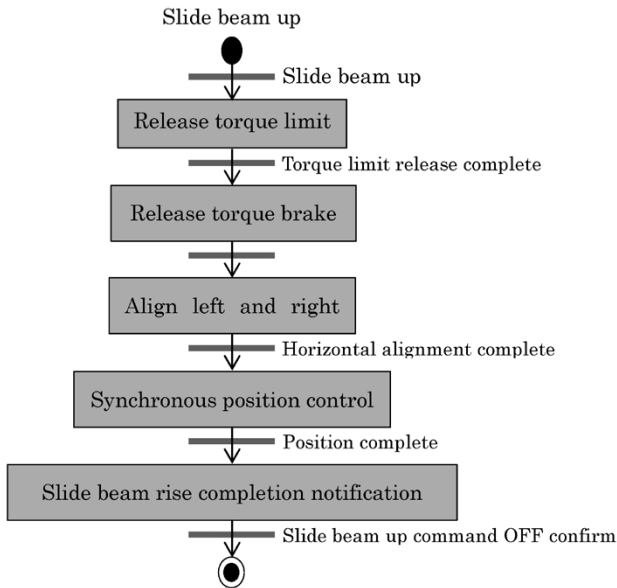


Fig.10 Flow of elevating operation for spindle

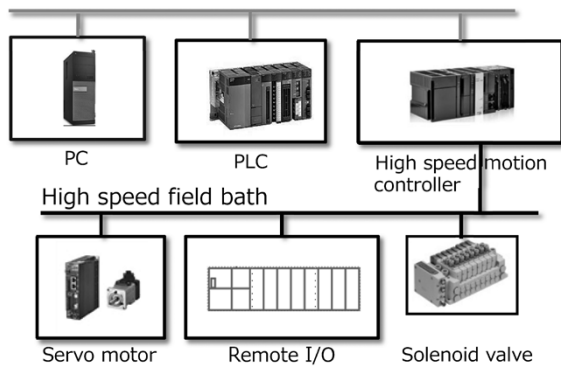


Fig.11 Controller configuration

Conclusions

Kobe Steel resolved the trade-off between improved measurement repeatability and short cycle time, and since Librota's commercialization in 2013, more than 70 units have been sold, mainly in China and Southeast Asia. It can respond to diverse needs with the optional apparatuses required for tire quality inspection, including a sheet-of-light laser geometry system, which inspects a tire's circularity and concave/convex abnormality on a plane, and a shoulder grinder, which grinds the edge of a tire to reduce vibration and noise.

Kobe Steel will strive to expand the lineup of TUM responding to the wide range of customer needs, while developing the market in Europe and the U.S., and continue its activities to take the lead in the world market.

References

- 1) K. Goto, SHINKO TECHNO ENGINEERING REPORTS, 2015, Vol.43.
- 2) Kobe Steel. SPINDLE STRUCTURE AND TIRE TESTING MACHINE HAVING THE SAME. JP2012145503. 2012-08-02.
- 3) Kobe Steel. TIRE TESTING MACHINE. Japanese Unexamined Patent Application Publication No. Hei 6-317504. 1994-11-15.

Newly Developed Large Size Continuous Mixer (LCM-IM)

Kazuo YAMAGUCHI*1, Yoshinori KURODA*1, Toru OKADA*2

*1 Plastics Processing Machinery Department, Industrial Machinery Division, Machinery Business

*2 Mechanical Engineering Research Laboratory, Technical Development Group

A new generation continuous mixer has been developed to cope with the advancement of bi-modal high-density polyethylene (HDPE), which is more difficult to mix. Basic mixing experiments were carried out to confirm that the new continuous mixer, which has been developed on the basis of a new mixing theory, effectively eliminates the gels of the bi-modal HDPE film and exhibits mixing performance superior to that of conventional continuous mixers. Furthermore, a new technique for measuring the action force of mixing has been developed. This technique was used to obtain data, which was analyzed by a newly established analysis method to confirm the mechanical reliability of the new continuous mixer.

Introduction

A large mixer, such as Kobe Steel's LCM (Fig. 1), used for primary granulation, must melt and mix powder-like resin polymerized in a reactor in the upstream of the resin production process and homogeneously blend additives, etc., as required. Meanwhile, in recent years, bi-modal high-density polyethylene (HDPE) resins with favorable durability, strength and excellent formability are being actively developed.¹⁾ Some of these newly developed HDPE resins are difficult to mix due to the difficulty of homogenizing the polymer components in their raw powder.

In order to cope with such newly developed bi-modal HDPE resins, Kobe Steel has extended the conventional design theory of rotor shape, which plays a central role in the mixing operation, and employed intermeshing rotors to achieve a successful mixing performance superior to that of the conventional rotors.

Since the reaction force received by the intermeshing rotors during mixing was unknown, the company developed a method to measure it accurately. This has made it possible to use the actual measurement of the reaction force in

the design, ensuring the reliability of the mixer employing intermeshing rotors.

1. Development of mixing rotors

A procedure was adopted in which a two-dimensional model test apparatus was used first to pursue the cross-sectional shape of a rotor that can achieve high mixing quality with less energy, and then the resulting cross-sectional shape was applied to a continuous mixer.

1.1 Mixing theory

The dispersion of gel (agglomeration of undispersed polymer) is driven by the fluid force, exerting shearing and stretching actions, caused by the resin flow created by the mixing blade. Conventionally, Kobe Steel evaluated the mixing performance on the basis of the shear stress the material receives as it passes near the tip of a mixing blade and the number of times the material receives the shear stress.²⁾ As for conventionally shaped rotors, the company focused on increasing the shear stress and the number of times that tip-passing occurred to ensure the mixing quality of bi-modal HDPE resin, which has been developed in recent years.

For the production machine, this means decreasing the production volume to increase the residence time and increase the frequency of tip-passing, or reducing the tip clearance to provide higher shear stress. Such an attempt, however, may result in the problems of increased energy consumption, and deterioration of resin due to excessively high temperature. Furthermore, a larger size mixer is required to secure the production volume.

In designing the cross-sectional shape of the mixing blade for the new continuous mixer, the emphasis was put on the mixing action of stretching, in addition to that of shearing, to attain energy efficiency such that the reduction rate of the gel is maximized for the energy provided.

In this way, the development goal for the new continuous mixer was set to secure production volume with the size of a conventional machine and achieve quality using the smallest possible amount of energy.

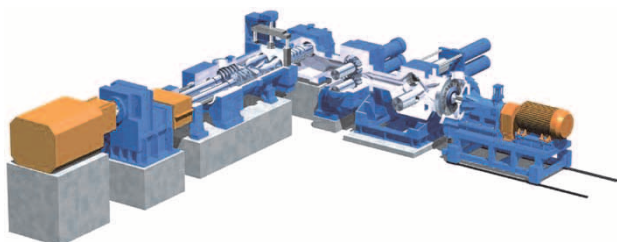


Fig. 1 Large continuous resin mixer, LCM-H

1.2 Method for evaluating mixing

For pipe grade HDPE, used for gas piping, etc., the "white spots" that appear upon mixing and dispersing carbon were regarded as gel, and their size (hereinafter referred to as "ISO rating") and quantity (as represented by white spot area, hereinafter referred to as "WSA") were evaluated. Fig. 2 shows an example of photomicrographs containing gel.

1.3 Evaluation of rotor cross-sectional shape on two-dimensional model

1.3.1 Experimental method

A two-dimensional (2D) model test apparatus was used to evaluate the cross-sectional shapes of rotors. This apparatus performs mixing experiments simulating a two-dimensional cross-section of a continuous mixer (Fig. 3). The degree of meshing between two rotors is set for two types of rotors, a tangential type and intermeshing type. Fifteen types of rotor cross-sectional shapes (Table 1) were prepared using the tip clearance and the inclination angle (front angle) of the working surface as the main parameters.¹⁾

These rotors were installed on the 2D model test apparatus, which was charged with powder material and carbon black powder for coloration. After the mixing operation was performed for a prescribed

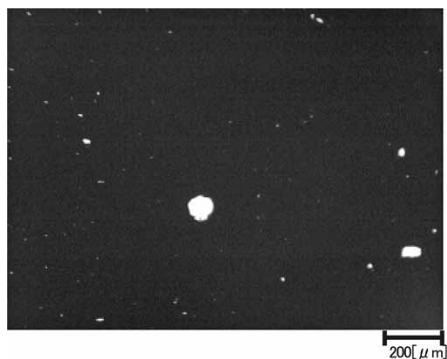


Fig. 2 Gel (white spots) in polyethylene compound pellet colored with carbon black

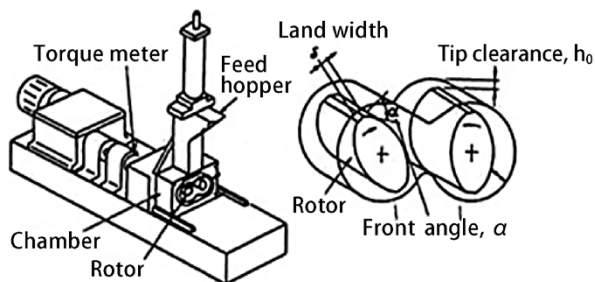


Fig. 3 2D model test apparatus

time, the melted and mixed material was taken out to make comparisons of the ISO rating and WSA.

1.3.2 Experimental results

In general, the mixing action and mixing energy are roughly in proportion, and the greater the energy, the greater the degree of mixing that is accomplished. In the experimental results, the rotor achieving superior mixing with a small energy input is regarded as exhibiting high efficiency and excellent performance.

Therefore, to make a comparison, the dispersion ability of each rotor shape was normalized by the specific energy, which is the value obtained by dividing the total energy required for mixing by the amount of material to be processed. Fig. 4 shows how the WSA values of mixtures are reduced during the mixing time in the 2D model test apparatus in the cases of the 15F rotor shape, which exhibits the most favorable mixing performance with a low energy input among the standard tangential-type rotors, and the 15Q rotor shape, which exhibits the most favorable performance among the intermeshing rotors.

In a tangential-type rotor, mixing is driven mainly by the shearing action occurring in the wedge-shaped space between the inner wall of the

Table 1 Cross-sectional shapes of rotors for 2D model test

		Front angle			Land width	New concept shape
		Small	STD	Large	Large	
Tip clearance	Narrow	Rotor # 15A	Rotor # 15B	Rotor # 15C	Rotor # 15L	Rotor # 15P
	STD	Rotor # 15E	Rotor # 15F [STD]	Rotor # 15G	Rotor # 15M	Rotor # 15Q
	Wide	Rotor # 15H	Rotor # 15J	Rotor # 15K	Rotor # 15N	Rotor # 15R

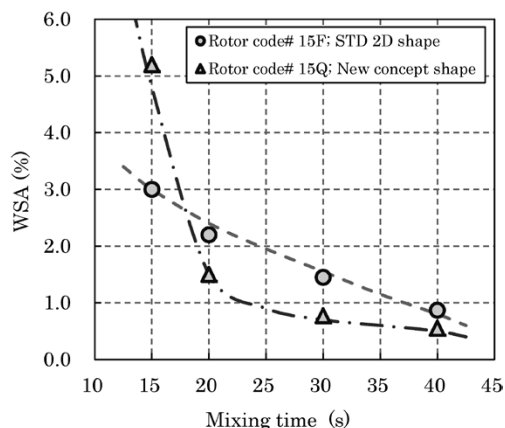


Fig. 4 Results of mixing experiment using 2D model test apparatus

chamber and the rotor tip. Among the standard tangential-type rotors, the 15F rotor shape is believed to provide the mixture with shearing action most efficiently.

Among the intermeshing rotors, the 15Q rotor shape showed an even more favorable performance than the 15F shape. That is, a favorable WSA value was achieved within a shorter mixing time. In the case of intermeshing rotors, it is believed that a complicated flow field is generated near the center part where the rotor meshes, which causes stretching action in the flow, in addition to the shear action between the inner wall of the conventional chamber and the rotor tip. In a stretching stress field, the gel is dispersed by energy smaller than that in a shearing stress field. This is considered to be the reason for the more efficient gel dispersion.³⁾

1.4 Application to continuous mixer

A rotor for continuous mixers comprises a screw part for sending material downstream and a rotor part for providing mixing action. In general, the rotor part consists of a pair of threads each having a relatively long pitch, one for forwarding the material and the other for returning the material.

A study was conducted to determine the optimum combination of the length and angle of the threads for forwarding and returning the material, including the combinations for the conventional tangential rotors, to select candidate cross-sectional shapes of rotors to be applied to the continuous machine.

Various combination experiments have revealed that optimal mixing performance is achieved by a two-stage mixing-rotor configuration that follows the LCM-H mixing concept, in which a tangential-type rotor is applied to the first mixing part, and an intermeshing type rotor is applied to the second mixing part. The conventional LCM-H and newly developed LCM-IM were used to mix and granulate film-grade bi-modal HDPE, and the pellets thus prepared were formed into films. The total area of the gel in the film was plotted against the specific energy input (SEI) required for mixing, as shown in Fig. 5.

Fig. 6 schematically compares the rotor construction of the newly developed LCM-IM with that of the conventional LCM-H. The newly developed LCM-IM employs the 15F cross-section for the first stage and the 15Q cross-section for the second stage.⁴⁾

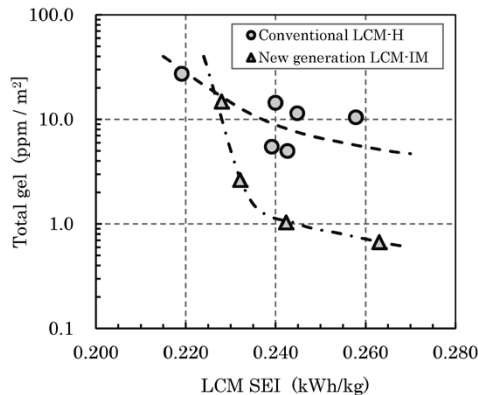


Fig. 5 Results of mixing experiment using continuous mixer

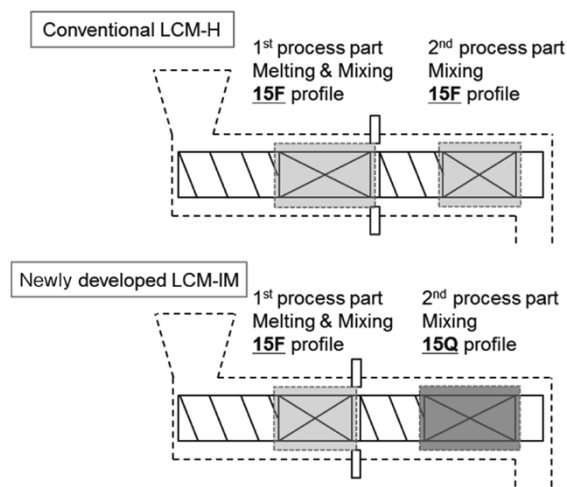


Fig. 6 Comparison of rotor arrangements between conventional LCM-H and newly developed LCM-IM

2. Measurement of mixing force

Mixing force is an important factor in designing LCM. In LCM, the force required for melting and mixing resin is provided as the mechanical action force of a rotating rotor. The rotor receives the reaction force. Unlike bi-axial extruders, this reaction force is supported by the bearings holding the rotor. As a result, the rotor becomes subjected to repeated bending stress, which can cause fatigue fracture if the stress exceeds the allowable limit.

The mixing force has been measured every time the shape was changed since the beginning of the LCM development. Intermeshing rotors, however, are unprecedented and unknown. Hence, the mixing force was measured in more detail before adopting the new intermeshing rotors.

2.1 Mixing force measuring system

The new LCM employs two-stage mixing, and each of its mixing rotors comprises a first mixing part and a second mixing part. The newly developed load-measuring system includes strain gauges to

independently measure the force acting on each mixing part.

Each rotor is supported by three bearings, i.e., two bearings, both supporting the drive end, and one bearing supporting the water end. Therefore, the deflection due to mixing force constitutes a statically indeterminate beam problem, and the superposition principle can be applied in a model where the mixing force acts on two locations. Fig. 7 shows the relationship between the strain gauge location and load location for the rotor supporting method.

Each of the strain values at the drive end (DE) and the water end (WE) is a composite value of the strain due to the mixing forces acting in the first mixing part and the second mixing part. Hence, the loads are applied separately in advance in the first mixing part and the second mixing part to measure the strain values and to determine the linear coefficients, a_1 , a_2 , β_1 and β_2 , of the force-strain relationship. The relationship between the mixing force and measured strain is expressed by the following simultaneous equations:

$$\varepsilon_{DE} = a_1 \cdot F_1 + a_2 \cdot F_2$$

$$\varepsilon_{WE} = \beta_1 \cdot F_1 + \beta_2 \cdot F_2,$$

wherein F_1 and F_2 are the mixing force acting in the first mixing portion and second mixing part, respectively, and ε_{DE} and ε_{WE} are the strains at the DE and WE, respectively.

Measured strains are substituted into these simultaneous equations, and solving the equations determines the mixing force independently imposed on the first mixing part and the second mixing part.⁵⁾

2.2 Results of mixing force measurement

Examples of measured mixing force are described. Fig. 8 shows the fluctuations of the mixing force measured at the first mixing part and second mixing part. Fig. 9 shows the direction and magnitude of the mixing force at the moment when

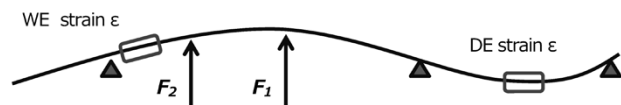


Fig. 7 Relationship between mixing force and strain

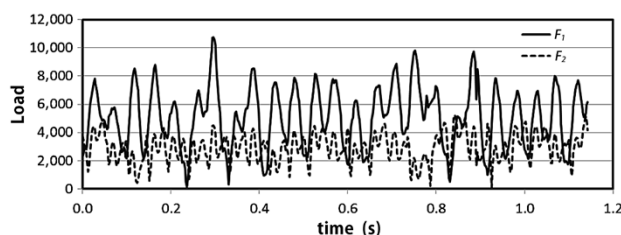


Fig. 8 Time history of mixing force

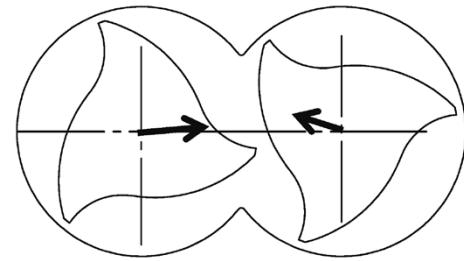


Fig. 9 Example of mixing force direction measurement

it reaches the maximum in the mixing part.

These evaluation results provide the basis for rotor design taking into account the load acting on the rotor during operation and without any risk of breakage, etc.

Conclusions

In the development of a new continuous mixer, it is essential to develop a rotor shape for improved mixing performance and an accurate mixing force measurement technology that supports it. These are regarded as the basis for the development of Kobe Steel's large mixers. The material development of HDPE is still being carried out by material manufacturers. Kobe Steel's continuous mixers must constantly improve their mixing performance so as to catch up with these developments.

The technologies introduced in this paper provide the foundation of future rotor development. The technologies can be combined with the flow analysis technology being developed by Kobe Steel's corporate research laboratories, to respond in a timely manner to market needs. Kobe Steel will continue to strengthen its technology development framework and further improve competitiveness.

References

- 1) Y. Nagai, Journal of the Society of Rubber Science and Technology, Japan, 2007, Vol.80, No.8, pp.315-316.
- 2) K. Inoue et al., R&D Kobe Steel Engineering Report.1994, Vol.44, No.3, pp.53-56.
- 3) Kobe Steel, Ltd., CONTINUOUS KNEADING MACHINE AND KNEADING METHOD, Japanese Patent No.5832172, Nov.06, 2015.
- 4) Kobe Steel, Ltd., CONTINUOUS KNEADING APPARATUS, Japanese Patent No.6242232, Nov.17, 2017.
- 5) Kobe Steel, Ltd., METHOD FOR OBTAINING ROTOR LOAD GENERATING IN KNEADING ROTOR OF KNEADER, ROTOR LOAD CALCULATION DEVICE, AND KNEADER, Japanese Unexamined Patent No.2016028877, Mar.3, 2016.

New Technology for Continuous Casting Machine

Tomonori NISHIOKA*¹, Fumiki ASANO*¹, Hiroshi KAWAGUCHI*²

*¹ Heavy Machinery Department, Industrial Machinery Division, Machinery Business

*² Industrial Machinery Engineering Division, SHINKO TECHNO ENGINEERING CO., LTD

In pursuit of high productivity, energy saving, steel-type versatility, and more stringent quality, each engineering company of steel making equipment has made a variety of unique development and improvements of continuous casting machines since its full-scale practical applications in the 1960s. Kobe Steel has newly developed an optimal support mechanism for a large tundish, and a highly precise weighing device for tundish cars, which are closely related to safety and workability. In addition, the company has newly developed a structure, capable of maintaining high rigidity and movements without backlash for an extended period of time, for the mold oscillator and supporting roll stand, which can significantly affect the quality of cast blooms. This paper introduces these technologies, which have been employed in the continuous bloom casting equipment for special steel—equipment that was delivered to Kobe Steel's Kakogawa Works in January 2017.

Introduction

Continuous casting equipment is used to continuously cool and solidify molten steel, and its apparatuses must demonstrate stable performance in a high temperature environment.

In the periphery of the continuous casting machine (CCM), which is located the farthest upstream, there are large apparatuses such as a ladle turret, tundish, and tundish car, which slew, lift, and/or travel in a three-dimensionally interlacing manner. The No. 6 continuous casting equipment at Kobe Steel's Kakogawa Works, recently delivered by Kobe Steel, includes a casting machine that handles a ladle containing 240 tonnes of molten steel. Any trouble with the casting machine during the handling of molten steel can lead to a serious accident. Hence, each apparatus must have excellent workability and high reliability.

In the main CCM equipment (e.g., mold, mold oscillator, and supporting roll stand), which is located in the downstream of the pig bed, a primary solidified shell is formed in the mold, and the solidified shell is grown by spray cooling in the secondary cooling zone to continuously produce semi-finished slabs. In order to manufacture a high-quality slab without any hazardous cracks on the surface or inside, no strain exceeding the allowable limit should be applied to the slab during solidification. The mold, mold oscillator, and

supporting roll stand are required to have structures with high rigidity and to move without backlash so as to allow each slab to be accurately drawn along the track even under high-temperature high-load conditions.

Kobe Steel has conducted development and improvement in various manners to meet customer requests, not only for apparatus reliability but also slab quality. This paper introduces the technologies adopted to the continuous casting equipment for producing special steel blooms that was delivered to Kobe Steel's Kakogawa Works in January 2017.

1. Tundish car

1.1 Role of tundish car

A tundish car (hereinafter, a "TD car") is a self-propelled carriage that transports a tundish (TD), which has the role of distributing molten steel poured from a ladle into a plurality of strands. **Fig. 1**¹⁾ shows a conventional TD car with a TD mounted on it. Each TD is heated to a high temperature by a heating apparatus at a standby position and transported to the casting station by the TD car immediately before casting begins.

In addition to the traveling function, a TD car comprises a lifting function for inserting a submerge nozzle arranged at the bottom of each TD into a mold, a centering function for adjusting the position of the submerge nozzle, and an automatic molten-steel-level control function for keeping molten steel

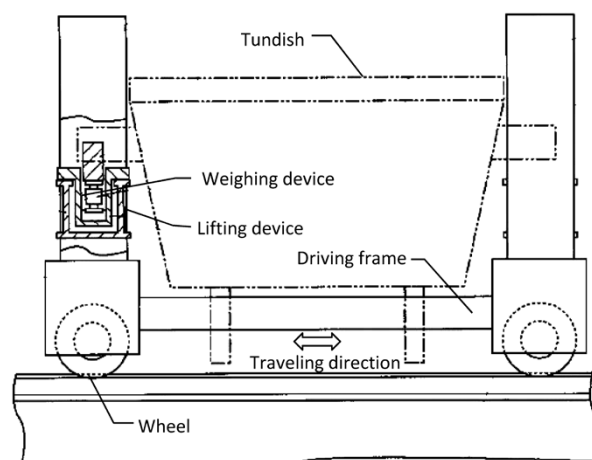


Fig. 1 Conventional tundish car with tundish mounted¹⁾

at a constant level to separate impurities by flotation. One of the important devices of the automatic molten-steel-level control is a weighing device, which is required to measure the weight of molten steel in each TD with high accuracy while the weight changes from time to time.

The size of the TD car is usually increased as the number of strands increases, and the interference with adjacent apparatuses becomes tighter. Therefore, it must have a mechanism that is lean in terms of structure dynamics.

1.2 Problems of conventional technology

The multi-strand bloom continuous casting equipment recently delivered by Kobe Steel has a large TD whose total weight exceeds 200 tonnes. The TD is surrounded by a ladle above, a ladle turret on its side and a mold below it. In this limited space, it must accomplish the functions of traveling, elevating, centering and weighing. In addition, the operators must be able to safely perform their work around the ladle, TD, and mold.

A Kobe Steel's conventional TD car with lifting and weighing functions generally adopted a method of supporting the trunnions at both ends of a TD. However, when applied to a large, long TD for multi-strands, as in this case, Kobe Steel's conventional structure causes large bending stress in the TD itself due to its own weight. Hence the rigidity of the TD must be increased, which has turned out to be difficult to achieve within the limited space.

1.3 New technology

1.3.1 Main frame construction of new TD car

The new TD car consists of a carriage frame, wheels, a lifting frame, a saddle frame, a lifter, a weighing device, a saddle-frame actuator, and a driving unit. **Fig. 2** shows the new TD car with a TD mounted on it. The right side of the figure shows the lifter in a raised position, while the left side shows the same in a lowered position. The latter is the position during the casting operation.

The new TD car comprises a carriage having a rectangular-frame structure, a wheel attached under each corner of the carriage, and a hydraulic-cylinder type lifter placed on top of the carriage. Furthermore, a rectangular lifting frame is mounted on the rod tips of these hydraulic cylinders. Each rod tip is made to coincide with the corresponding corner of the frame, and a load cell is placed between them. The saddle frame is placed so as to surround

the two sides of the rectangular lifting frame, and both ends of the saddle frame are placed on the receiving rollers provided at the four corners of the lifting frame. A TD is placed on the four receiving parts provided on the saddle frame. The new TD car also employs a hydraulic cylinder for driving the saddle frame.

Each trunnion of the hydraulic cylinder is connected to the lifting frame, while each clevis is connected to the saddle frame, so that the saddle frame can be moved to the horizontal direction relative to the lifting frame. In other words, each TD can be moved in the direction orthogonal to the traveling direction of the TD car, so that the respective submerge nozzle can be adjusted to the center of the mold.

It should be noted that the greater the distance between a TD and mold, the greater the potential energy of the molten steel to be discharged from the TD, which makes the submerge nozzle longer and is not desirable. Therefore, the space between the TD bottom and the mold-top end is made narrow. The middle portions of the carriage frame, lifting frame, and saddle frame must traverse this narrow space, which has been enabled by the structure shown in **Fig. 2**.

1.3.2 Supporting mechanism of new TD

The new TD car supports a TD at the point where the deformation of the TD is minimized. The bending stress occurring in the TD itself is kept low by having both ends of it overhang the car. A structure was also devised in which the wheels, carriage frame, hydraulic lifting cylinder, load cell, and lifting frame are arranged in a vertical line to prevent a bending load from acting on the carriage frame.

An optimum support mechanism for a large, long TD has been realized by incorporating these ideas.

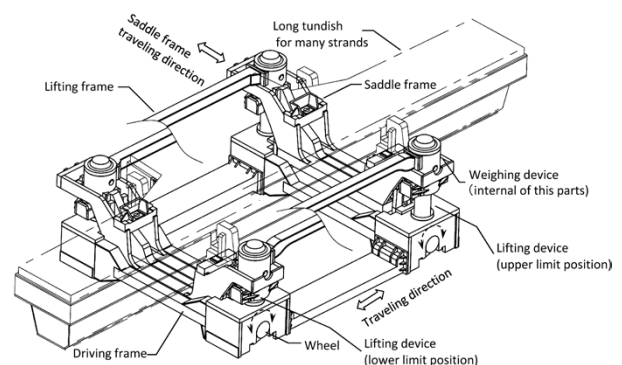


Fig. 2 New tundish car with tundish mounted (right: lifting state, left: lowering state)

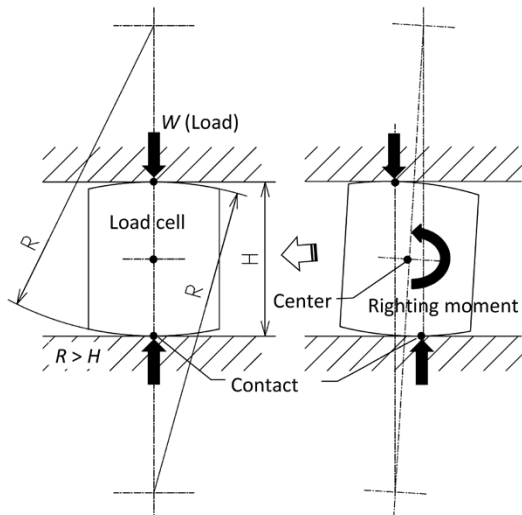


Fig. 3 Restoration principle of load cell

1.3.3 Weight measurement mechanism of new TD

In order to improve the accuracy of weight measurement using a load cell, it is necessary to devise an ideal mechanism for supporting the load only in the vertical direction. In order to increase the measurement accuracy, Kobe Steel employs a double-convex-type load cell. When a vertical load acts on a double-convex-type load cell in an inclined state, the load cell itself rolls in the vertical direction like a self-righting doll (Fig. 3). It is a characteristic of the load cell that the greater its inclination, the greater the resilience to the vertical (upright) direction becomes, and the lifting frame placed on the load cell swings like a cradle. When a traveling TD car accelerates or decelerates, a force is generated in the horizontal direction in the lifting frame to tilt the load cell, whereas, when it travels at a constant speed or is stationary, the load cell is restored to the upright position. This property was exploited in eliminating the lifting guides for restraining the lifting frame, and other restraints that can deteriorate the measurement accuracy. This, as a result, has secured an extremely favorable measurement accuracy.

2. Mold oscillator

2.1 Role of mold and mold oscillator

The mold is a primary cooling apparatus for forming an initial solidified shell that is healthy and homogeneous. In the mold, molten steel comes in contact with a copper plate the back of which is water cooled. The mold oscillator is an apparatus which oscillates the mold in the pulling direction of the slab to prevent adhesion between the mold

and the surface of the solidified shell. Here, the oscillation typically has a sinusoidal waveform. When a lateral displacement of the oscillating mold occurs, the fluctuation of the molten surface becomes so large that it adversely affects the formation of the initial solidified shell in the meniscus portion, which is formed in every cycle of mold oscillation. In other words, disturbance occurs in the oscillation mark, causing surface defects. In order to secure the surface quality of slabs, it is very important to suppress the lateral displacement of the mold oscillator.

2.2 Problems with conventional technology

Fig. 4 shows a typical mold oscillation mechanism commonly used today. The oscillating table is supported by a pair of links, each configured in a parallelogram shape, which creates a pseudo circular movement along the profile of the apparatus when a vertical movement is provided at the end of a driving lever. Hydraulic cylinders or electric motors with eccentric shafts are used for the driving source of the vertical motion. This mechanism has the advantages of allowing the placement of the oscillation source in a favorable environment remote from the mold, avoiding thermal influence, facilitating maintenance, easily responding to amplitude change, etc. On the other hand, this mechanism has a plurality of joints connecting the links, and each joint engages in repetitive forward and back movement. Since the oscillation amplitude is rather small with respect to the link length, the rolling angle of each bearing, built in the corresponding joint part, is very small, and the rolling angle of the roller in the bearing becomes extremely small. Therefore, it has the drawback that the lubrication oil film is not formed on the rolling surface of each roller, causing the bearings to wear prematurely, and the favorable oscillation

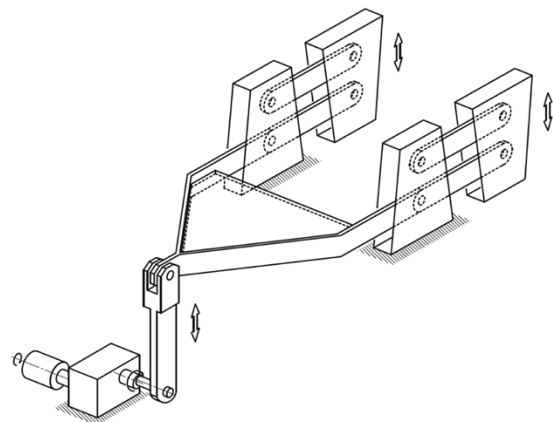


Fig. 4 Lever-type mold oscillator

state cannot be maintained for an extended period of time. Furthermore, the gaps existing in the joints may cause lateral displacement during oscillation.

2.3 New technology

2.3.1 Construction of new mold oscillator

As shown in Fig. 5,²⁾ Kobe Steel's new mold oscillator³⁾ comprises a pair of eccentric shafts supported by corresponding fixed bearing boxes on the upper side of a fixed oscillation table in the form of a rectangular frame, wherein each eccentric shaft is driven by a common electric motor via reduction gears. Each of the eccentric shafts has two movable bearing boxes attached via bearings.

The movable bearing boxes support the four corners of the rectangular-frame-shaped oscillation table from below through thin sheet-like connecting plates that are placed vertically. Each spring plate has both ends supported by the fixed table, while the center part of the spring plate is connected to the oscillation table.

2.3.2 Oscillation mechanism causing no lateral displacement

Kobe Steel has developed a mechanism, as described below, for the new mold oscillator that causes no lateral displacement. The spring plates, bending and deforming in the vertical direction, permit the vertical displacement of the oscillation table. Meanwhile, the spring plate regulates the lateral displacement of the oscillation table.

Along with the rotation of the eccentric shaft, the movable bearing box causes an orbital motion that centers on the rotation center axis of the eccentric shaft with the radius of the eccentricity. For the orbital motion of the movable bearing box, the thin sheet-like connecting plate transmits

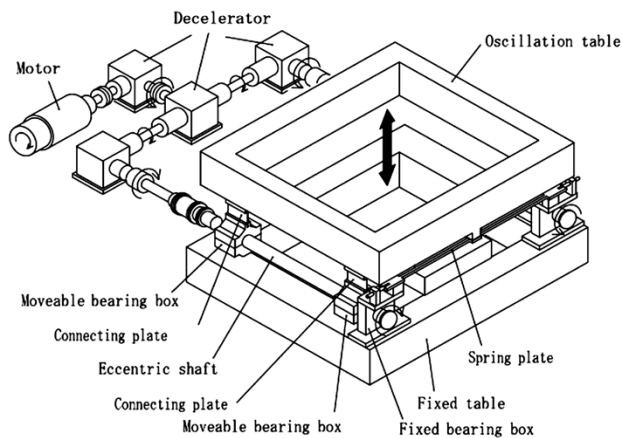


Fig. 5 New mold oscillator

only the vertical motion of the orbital motion to the oscillation table. The horizontal direction displacement of the orbital motion is absorbed by the bending of the connecting plate. Fig. 6 is an operation diagram of this motion.

The connecting plate and spring plate are subjected to bending deformation alternating in every other cycle of the mold oscillation; however, the stress caused by this deformation is set to be less than their fatigue limits. The weights of the mold and oscillation table, the frictional force generated between the mold and the slab, and the acceleration during the oscillation act as compressive forces on the connecting plate. Increasing the thickness of the connecting plate increases its resistance to buckling, but increases the bending stress. Conversely, decreasing the thickness reduces the bending stress, but decreases its resistance to buckling. Kobe Steel's connecting plate achieves the optimal degree of both bending stress and buckling strength, which are in a trade-off relationship.

2.3.3 Maintaining high precision oscillation performance

The oscillation mechanism devised by Kobe Steel, as described above, has eliminated all the pivot points of forward and reverse rotation; the pivot points have caused problems in the conventional technology. This has enabled high-precision oscillation to be maintained for a long period of time. No lateral displacement occurs during the oscillation because the horizontal direction is regulated without a gap by the spring plate. In addition, all the bearings rotate 360° in one direction without causing any problems associated with the repetition of forward and reverse rotations. Even when there is a small gap in a bearing part, the gap is kept pressed downward by the weight of the mold, causing no disturbance in the oscillation waveform. Any difference in the eccentric phases of the two eccentric shafts would cause a lateral displacement of the

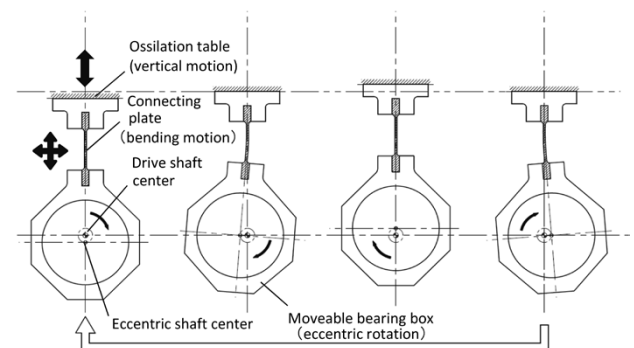


Fig. 6 Motion of connecting plate

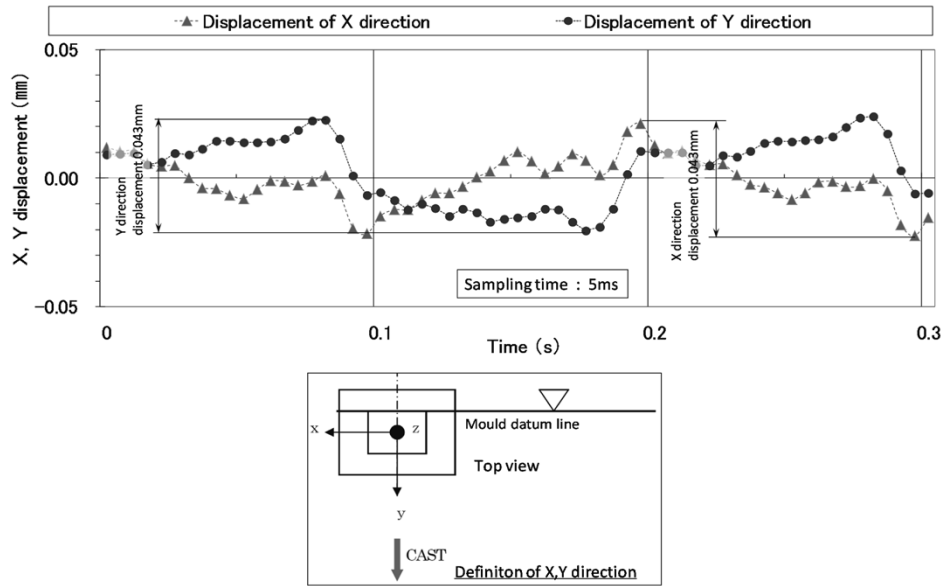


Fig. 7 Oscillation test results (X, Y displacement) of new mold oscillator

oscillation table; however, no difference in eccentric phase should occur, thanks to the two eccentric shafts that are driven by reduction gears branched from one electric motor. Also, the two eccentric shafts are rotated in opposite directions so that the horizontal forces generated at the time of oscillation cancel each other out. Furthermore, the stress generated by the alternating bending deformation is set to be less than the fatigue limit, which ensures the long-term durability of the connecting plates. The fixed table can be detached from the dedicated mount, enabling the mold oscillator to be taken out as a unit for offline maintenance, which has eliminated the need for online maintenance. The connection between the reduction gears and the eccentric shafts via drive shafts allows the placement of the vibration source in a favorable environment remote from the mold.

As a result of various measures, including ones for extending the service life, the amount of lateral displacement during oscillation was confirmed to be 0.05 mm or less, as shown in Fig. 7.

3. Supporting roll stand

3.1 Role of supporting roll stand

A supporting roll stand serves to guide a slab consisting of a shell filled with unsolidified metal by means of a set of rolls arranged in a predetermined profile. Solidification is promoted by the spray water cooling in the secondary cooling zone, where the slabs are completely solidified, and their quality is determined. A supporting roll stand plays major roles; for example, it suppresses the bulging that

may occur in the solidified shell due to the static pressure of the molten steel pool inside the slab, reduces the roll gaps to match the slabs' thermal contraction, and decreases strain caused by bending and unbending. Therefore, a supporting roll stand is required to have a rigidity high enough to withstand the deformation due to the heat and force received from slabs.

3.2 Problems with conventional technology

As shown in Fig. 8, a conventional supporting roll stand (hereinafter "conventional stand") comprises a lower frame, a set of lower rolls, an upper frame, a set of upper rolls, and a connecting member for connecting the lower frame and upper frame. In both the lower frame and upper frame, a plurality of rolls are attached at predetermined intervals via bearings, and the connecting member joins the upper and lower frames such that the lower rolls and upper rolls face against each other.

During casting, the slab is held between the lower and upper rolls, and the forces due to the static pressure of molten steel and straightening reaction act to stretch the connecting member. In addition, other forces act to bend the lower frame and upper frame. Furthermore, each member of the supporting roll stand is subjected to complicated thermal deformation during casting due to the increase in atmospheric temperature and radiant heat from the slab. As a result, each roll is displaced from its predetermined profile and causes misalignment.

The misalignment can cause internal cracks in the cast slab. Increasing the rigidity of the construction elements (the upper frame, lower frame, and

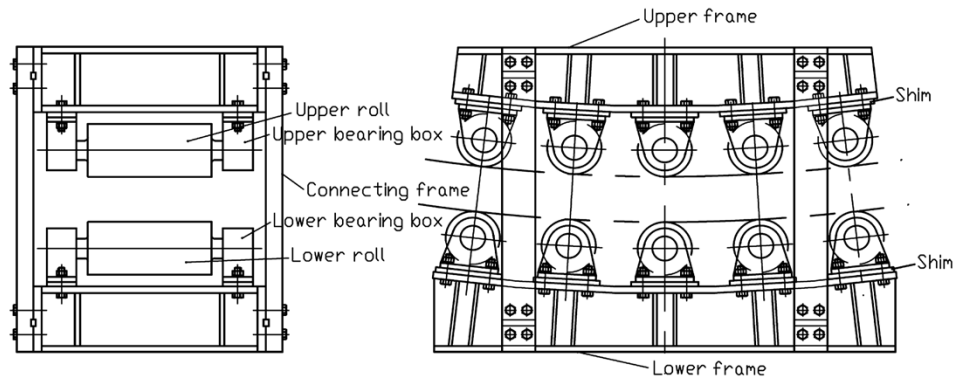


Fig. 8 Conventional supporting roll stand

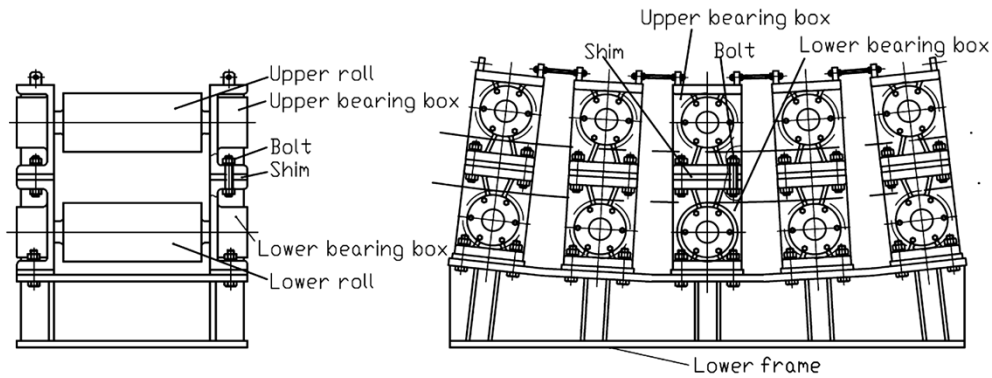


Fig. 9 New supporting roll stand

connecting member) may solve this problem. However, there is a limit in terms of the weight and cost of the stand. In addition, the fluctuation of the roll alignment due to the temperature change in the members cannot be avoided even by increasing the rigidity. For this reason, it was difficult to resolve the issue of roll misalignment in the conventional stand structure.

3.3 New technology

3.3.1 Construction of new supporting roll stand

The new supporting roll stand⁴⁾ comprises a lower bearing box supporting a lower roll and an upper bearing box supporting an upper roll, in which the lower and upper bearing boxes are connected pair by pair so as to eliminate the upper frame that was indispensable in the conventional stand. Fig. 9⁵⁾ depicts the new supporting roll stand. The lower surface of each lower bearing box is fastened by bolts to the lower frame via a shim for alignment adjustment. Furthermore, an upper bearing box is stacked on the lower bearing box via a shim to adjust the gap between roll surfaces, and both the boxes are fastened by bolts.

3.3.2 Advantages of new supporting roll stand

The structure of the new supporting roll stand is less susceptible to the influence of stretch deformation and thermal deformation, which, in the conventional stand, would occur in the upper frame and the member connecting the lower frame and upper frame. The displacement of rolls is minimal because the static pressure of molten steel and straightening reaction force, both acting on the rolls, are limited by the elastic deformation of a small area in the bearing box. In addition, the upper and lower bearing boxes are internally water cooled and are less susceptible to the temperature change in the surrounding area. This has enabled the initial roll gap and roll alignment to be maintained with high accuracy even when the surrounding environment is changed.

The assembly of the conventional stand required the following steps: First, the rolls on each of the upper frame and lower frame were assembled. Next, the upper frame was turned upside down so that its roll surfaces faced those of the lower frame, and the upper and lower frames were connected with tie rods. Then, the gap between the roll surfaces was adjusted to a predetermined dimension by means of shims placed between the bearing boxes and the frames. The new supporting roll stand, on the other

hand, has a structure in which each upper bearing box is mounted on a corresponding lower bearing box, and the upper and lower bearing boxes are fastened by bolts. This has made the assembly work safer and easier.

Conclusions

Continuous casting machines came to be in wide practical use in the 1960s, and since then, various R&D and improvements have been made in pursuit of high productivity, energy saving, steel-type versatility and quality improvement. This paper has introduced a tundish car, which is closely related to safety and workability, a mold oscillator, which is closely related to slab quality, and new technologies having to do with the supporting roll stand.

Kobe Steel will strive to continue development

and improvement to respond to customers' more advanced needs, including the improvement of apparatus safety and reliability, and further improvement of slab quality.

References

- 1) H. Kawaguchi, "WEIGHING DEVICE AND CONTAINING BODY SUPPORT DEVICE PROVIDED WITH WEIGHING DEVICE," Japanese Patent No.5030598.
- 2) H. Kawaguchi, SHINKO TECHNO ENGINEERING REPORTS, 2015, Vol.27, No.43, p.16.
- 3) H. Kawaguchi et al., "MOLD OSCILLATOR," Japanese Patent No.4974702.
- 4) H. Kawaguchi, "CAST SLAB GUIDE APPARATUS FOR CONTINUOUS CASTING EQUIPMENT," Japanese Patent No.4593992.
- 5) H. Kawaguchi, SHINKO TECHNO ENGINEERING REPORTS, 2015, Vol.27, No.43, p.18.

Horizontal CIP Apparatus for Food

Tomoya MINAMINO*¹

*¹ Heavy Machinery Department, Industrial Machinery Division, Machinery Business

High pressure processing (HPP) technology attracted attention in the 1980s as a non-thermal sterilization method, and its research, development and practical application were promoted in Japan. High pressure food processing equipment, which did not spread widely at that time, is now seeing increased demand due to recent situational changes in food companies in Japan. Conventional, vertical, cold-isostatic-pressing (CIP) apparatuses are difficult to install in the facilities of food companies; hence, a horizontal CIP apparatus, "FOOD FRESHER," has been developed. This paper describes the situation in high-pressure food processing technology and outlines the newly-developed FOOD FRESHER and its future development.

Introduction

High pressure processing (HPP) is a process of applying a high pressure above several thousand bars on food and has been proposed as a sterilization method to replace heat treatment. Full-fledged research and development began in the latter half of the 1980s in Japan. There also are studies on the utilization of HPP to obtain, for example, unique texture and flavor, as well as the sterilization effect. Since the 1990s, HPP has been practically applied and disseminated to general products in the United States. In Japan, interest in and demand for the practical application of HPP have recently been increasing.

Against this backdrop, Kobe Steel has developed a horizontal cold-isostatic-pressing (CIP) apparatus, FOOD FRESHER, for food manufacturers by applying the technology of CIP apparatuses, which the company has developing for many years.¹⁾ In 2015, Kobe Steel delivered a 400 MPa machine, its first, for shucking oysters, and then it completed a machine with 600 MPa specifications. This paper outlines these high-pressure apparatuses and examples of the application of HPP.

1. Worldwide status of HPP

HPP is a technology mainly aimed at obtaining a sterilizing effect using the energy of pressure, instead of heat. Unlike heat treatment, pressure treatment generally does not promote any chemical change in food²⁾ and has the advantage of affecting neither nutrients nor flavor. Substantial research

and development activities were initiated in Japan in the latter half of the 1980s. Various applications other than sterilization have also been studied. These activities have resulted in a wealth of data regarding, for example, the modification of proteins and starches, utilization of a high-pressure non-freezing zone (pressurized rapid thawing, pressure-shift freezing, and pressurized non-freezing preservation), control of enzyme reaction (inactivation and activation), and the effect on biological membranes (extraction and osmosis).¹⁾

Since then jams and rice products have been sold as high-pressure processed foods; however, the application to general products has been limited due, among other things, to its lack of a sterilization effect on spores and the difficulty of obtaining Food Sanitation Act approval for it as a method of non-heating sterilization.

Meanwhile, stimulated by the extensive activities in Japan, basic research has been carried out overseas, mainly in Europe and the U.S. Especially in the United States, the practical applications of HPP spread rapidly in the 1990's, and it is being applied widely to juice, meat, pet food, baby food, etc.³⁾ One of the most common high-pressure processed foods in the United States is avocado paste. Unlike heat treated products, this high-pressure treated avocado paste retains its original flavor and texture, while having a longer best-before date.

Recently, the Japanese food industry has been increasingly interested in foods without antimicrobial additives and in unique products with natural flavor and texture not found in conventional products. As a result, HPP is attracting attention again. This method not only improves the quality of foods but also extends the product expiration date, an achievement that has been difficult in the case of heating sterilization. Thus, HPP is expected to reduce the amount of waste and the number of deliveries, contributing to the resolution of environmental issues.

In addition, there is an increasing interest in high-pressure processing as a means of increasing production capacity. Applying high pressure to shellfish, such as bivalve shells, and crustaceans can facilitate shucking, the extraction of scallops and meat. It also offers the advantage of more easily preventing the contamination of products by shell fragments, compared with the conventional

shucking by hand. The marine product processing industry that deals with bivalve shellfish and the like suffers from the lack of shucking workers, and has already introduced high-pressure processing for shucking applications.⁴⁾ In Japan, HPP is being disseminated into food processing facilities in this way.

2. HPP apparatus

2.1 Construction of HPP apparatus

HPP employs a CIP apparatus using liquid as a pressure medium, or, a warm-isostatic-pressing (WIP) apparatus, which is based on a CIP apparatus and is equipped with a heating function up to approximately 90°C. Kobe Steel began the production of high-pressure apparatuses for industrial applications, such as metal, ceramics and electronic parts, in the 1960s and has sold nearly 900 units so far.¹⁾ For industrial applications, CIP apparatuses with pressure capacities greater than 700 MPa and vessel volume greater than 15 m³ have been used in production (Fig. 1). As shown in Fig. 2, the basic structures of CIP apparatuses are classified into the following two types in accordance with the difference in their pressurizing mechanisms:

(1) Intensifier type (Fig. 2 (a)): a mechanism that feeds a medium into a high-pressure vessel for pressurization by an intensifier and is mainly used for a mid- to large-size machine with a processing pressure of 600 MPa or below.

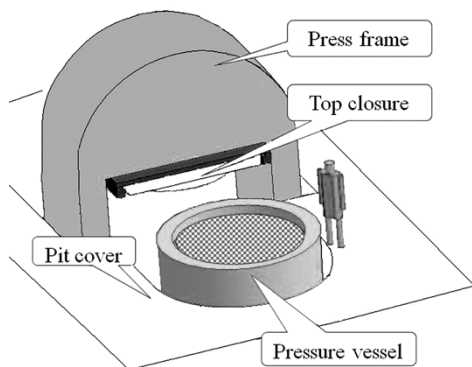


Fig. 1 Large CIP apparatus

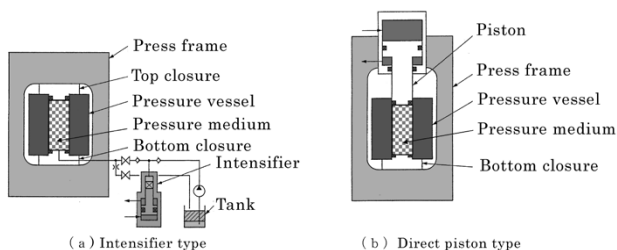


Fig. 2 Comparison of pressurizing system¹⁾

(2) Direct piston type (Fig. 2(b)): a mechanism that pushes a piston into a high-pressure vessel to directly pressurize the medium and is mainly used for a small machine with a processing pressure exceeding 600 MPa. In this construction, the pressure vessel and pressure cylinder are arranged in series, making the body of the apparatus larger than that of the intensifier-type. It requires no intensifier or ultrahigh-pressure piping, which simplifies the overall construction of the apparatus.

Kobe Steel applied the technologies of the intensifier-type and direct-piston-type machines described above and had developed a vertical-type high pressure apparatus for the food industry, as described below.

2.1.1 HPP apparatus for research and development

A direct-piston-type compact apparatus (Dr. CHEF) for R&D is shown in Fig. 3. The pressure specified for this apparatus is 700 MPa (processing chamber size, $\phi 60 \times 200$ mm), and it is also possible to build an apparatus with a maximum specification pressure of 1 GPa (processing chamber size, $\phi 50 \times 150$ mm). The apparatus is very compact, allowing manual swinging of its press frame that holds the axial force caused by high pressure, for example.

2.1.2 HPP apparatus for production

A high-pressure processing apparatus for cooked rice packs is shown in Fig. 4. This apparatus has a vertical arrangement with a height of approximately 5 m, in which work is put in and taken out from the opening on the top of the pressure vessel by a dedicated carrier device. Food processing requires high productivity attained through continuous processing. To that end, this apparatus combines two vessels with a pressurizing device and adopts



Fig. 3 HPP apparatus (Dr. CHEF) for research and development¹⁾

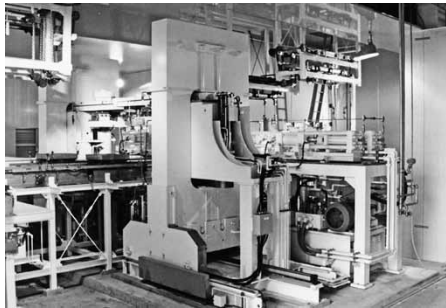


Fig. 4 HPP apparatus for production



Fig. 6 FOOD FRESHER (400 MPa, 100L of process volume)

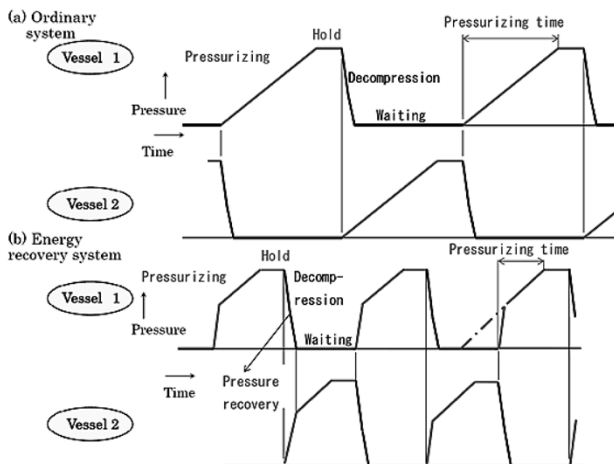


Fig. 5 Comparison of time-charts for high pressure processing¹⁾

a differential pressure recovery system, which has shortened the pressurization time to about half that of the conventional system and realized high productivity. Fig. 5 (a) is a time chart for the apparatus operated by a conventional system, while Fig. 5 (b) is a chart showing the time when the differential pressure recovery system is adopted. These figures indicate the effect of cycle time shortening.

3. Development of horizontal CIP apparatus

3.1 Background of development

Due to a serious labor shortage and the aging of the workers involved in the shucking of bivalves, Kobe Steel received a request from the Momonoura Producer of Oysters Consolidated Company for the development of a high-pressure apparatus for oyster shucking. Kobe Steel's apparatus at that time was a vertical type, as described in the previous section, requiring a crane for work loading and unloading. Also, the heavy apparatus requires a high soil-bearing capacity for its foundation. Hence, it was difficult to install a vertical apparatus in the building at the delivery site.

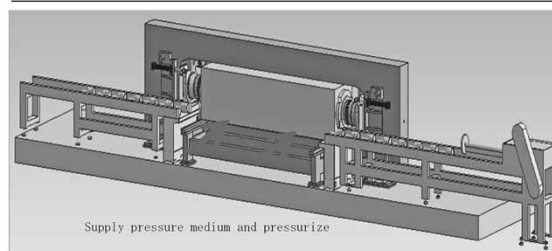
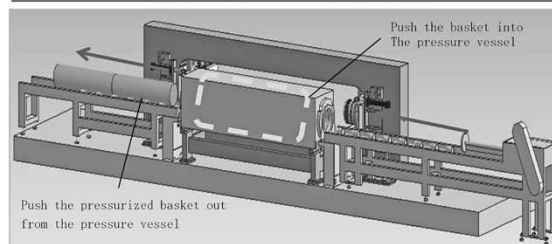
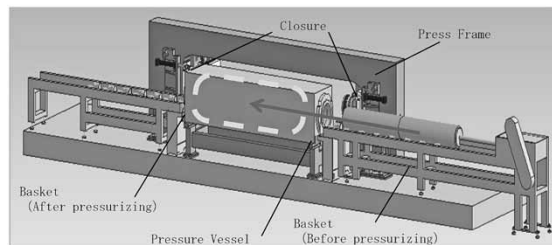


Fig. 7 Production process of FOOD FRESHER

To solve these problems, Kobe Steel developed a horizontal type CIP apparatus, "FOOD FRESHER," and delivered the first 400 MPa machine (processing volume: 100 liters) in 2015. Fig. 6 shows the appearance of FOOD FRESHER.

3.2 Advantages of FOOD FRESHER

3.2.1 Low height and ease of operation

The process flow of FOOD FRESHER is shown in Fig. 7. As a basket filled with work is pushed into the pressure vessel, a high-pressure treated basket is pushed out of the vessel. Subsequently, the pressure vessel moves to the pressurizing position, and water-supply and pressurization begin.

Compared with the conventional vertical CIP apparatus, the horizontal CIP apparatus has the following advantages:

- (1) The apparatus has a height of approximately 2 m (vertical type: 5 m) and can be installed in a building with low ceiling height.
- (2) It has a greater footprint compared with that of a vertical CIP apparatus and reduces the floor load per unit area.
- (3) The transport roller for inserting a basket filled with work into the pressure vessel is placed at the height of a person's waist. Hence, no special tool or device is required for transporting the baskets.
- (4) The entrance and exit for the baskets are separated, making it easier to prevent the mixing of processed products with unprocessed products that have a similar appearance.
- (5) The opening end of the pressure vessel is in the horizontal direction, and the pressure medium is always discharged outside after each treatment. This prevents impurities from accumulating, or from settling at the bottom, which facilitates hygiene control.

3.2.2 Light and compact

An HPP apparatus comprises a high-pressure cylinder and a press frame that supports the axial load caused by the internal pressure. The high-pressure cylinder and press frame account for most of the weight of the apparatus. In general, a high-pressure cylinder has either a single-walled structure, or a shrink-fit composite structure, whereas FOOD FRESHER employs a cylinder with a wire-wound structure (a structure strengthened by piano wire, which has a strength greater than that of forged steel, wound around the circumference of a core, constituting the cylinder) and has achieved significant space saving and apparatus weight reduction.

3.2.3 Compact intensifier with large discharge capacity

The food industry requires high productivity, and the cycle time of conventional CIP apparatuses must be at least halved. In the case of an intensifier-type apparatus, the largest portion of its cycle time is occupied by the pressurization of its intensifier. A general approach to shortening the cycle time is to increase the discharge amount by increasing the size of the intensifier. This increase in size, however, increases the weight of the components, which makes disassembly and maintenance difficult to perform at a food factory, which usually owns no facility for lifting heavy objects.

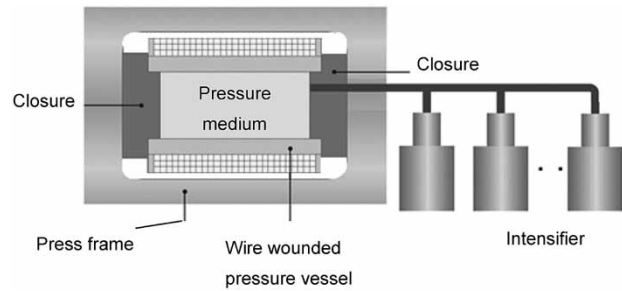


Fig. 8 Construction of high-pressure processing apparatus with several intensifiers

Hence, multiple intensifiers, each having a downsized body and increased plunger speed, were installed to increase the amount of discharge while suppressing the weight of each intensifier, which has shortened the cycle time. The construction of the high-pressure processing apparatus including the intensifier is shown in Fig. 8.

The seal portion becomes an important factor in increasing the speed of the plunger. Since food processing apparatuses use fresh water as their pressure medium, high-strength stainless steel is used for the pressure-tight parts of the pressure vessel, intensifiers and the like. Contact and sliding between the parts made of stainless steel tend to cause a seizure. The conventional CIP and WIP apparatuses use a pressure medium consisting of water with water-soluble oil added to it, which provides some lubrication effect on sliding parts and sealing parts. Fresh water, however, can provide only a minute lubricating effect. Hence, various measures, including the packing and backup-ring materials, surface treatment and shapes, were taken in order to realize high-speed motion and high-pressure sealing in such an unprecedented environment.

3.2.4 High-speed water supply

In order to shorten the cycle time, it is important to shorten not only the pressurizing step but also the water supplying step. Unlike the vertical CIP apparatus, the horizontal CIP apparatus discharges all the pressure medium at the time of work loading and unloading, and it is necessary to supply pressure medium to the empty pressure vessel for each cycle. The conventional CIP apparatus has a valve installed on its lid, and water is supplied to the pressure vessel via this valve. The water supply/discharge valve must seal the high-pressure medium, making it difficult to increase the bore diameter, and this sort of valve is not suitable for high speed water supply.

FOOD FRESHER has a water supply flange on the end surface of the pressure vessel and switches

the supply route of the pressure medium for the water supply process and pressurizing process, depending on the position of the lid, so as to supply pressure medium from the large diameter piping of the water supply flange. The water supply flange does not need to be sealed against the high-pressure medium, which allows the use of a feed path with a large bore diameter, enabling high-speed water supply.

3.2.5 Consideration for hygiene and safety

For food machinery, consideration for hygiene is important to prevent contamination of food by foreign matter and rust, for example. FOOD FRESHER uses fresh water as the pressure medium; hence, as a measure against rust, it employs many stainless-steel parts, not only for the wetted parts of the pressure vessel, intensifier, and piping, but also for peripheral devices. In addition, the pressure vessel and intensifiers are enclosed by stainless steel covers to ensure safety.

3.3 Development of 600 MPa testing apparatus and expansion of product lineup

The typical treatment pressure for bivalves such as oysters and crustaceans is approximately 200 MPa; however, there often are cases where higher pressure is required for treating other foods and beverages. In order to respond to the variety of needs, a 600 MPa apparatus (processing volume 50 liters) was developed and installed in Kobe Steel's Takasago Works. The appearance of the apparatus is shown in Fig. 9. Test apparatuses with this much processing capacity, 600 MPa, are rare in Japan. It allows customers not only to confirm the effect of high-pressure processing but also to simulate actual production, including production cost. In response to the demand for production apparatuses with various pressure capacities and processing volumes, a lineup of products has been prepared, as shown in Table 1.

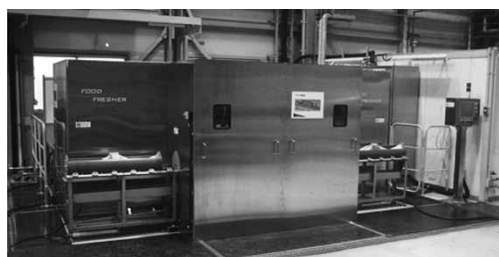


Fig. 9 FOOD FRESHER, testing apparatus (600 MPa, 50 L process volume)

Table 1 Lineup of HPP apparatuses

Application	Model	Pressure (MPa)	Process Volume (L)
Sterilization	FF6005	600	50
	FF6010		100
	FF6020		200
	FF6040	400	400
	FF4010		100
	FF4020		200
Shucking clams, crustaceans	FF4040	250	400
	FF2520		200
	FF2540		400
R&D	Dr.CHEF	700	0.6
		1,000	0.3

Conclusions

The development of a horizontal CIP apparatus, FOOD FRESHER, with advantages such as compactness and ease of operation, is believed to make the introduction of the HPP apparatus at food companies easier than it was before. For the further dissemination of high-pressure processed foods, it is important to lower their prices, and to this end, it will be necessary to improve the productivity of high-pressure apparatuses.

In high-pressure apparatuses, the equipment cost per unit volume decreases as the volume of the processing chamber increases,⁵⁾ and it is more economical to process using one larger apparatus than to process with multiple small ones. Hence, it is believed that the demand for apparatuses with vessels that are longer and have larger inner diameters will increase in the future. Large high-pressure apparatuses are capital intensive. Therefore, it is envisaged that a new management solution will be required, such as mass processing by a tolling service company, or equipment sharing between companies.

In addition, to improve productivity, it is important to ensure operational stability and to minimize downtime due to maintenance. In order to cope with such advanced operation, FOOD FRESHER can be equipped with a remote system for monitoring the state of the apparatus through IoT.

In the United States and other countries, the sterilization of beverages by high pressure processing has already been approved; however, this method, unfortunately, has not yet been approved in Japan.³⁾ The collaboration of the industry, government, and academia is indispensable in gaining approval. Kobe Steel will strive to contribute to the further development of HPP, making full use of its long-fostered technology for high-pressure apparatuses.

References

- 1) Y. Kishi. R&D Kobe Steel Engineering Report. 2008, Vol.58, No.2, pp.24-27.
- 2) K. Yamamoto. Food & Packaging. 2015, Vol.56, No.9, pp.540-549.
- 3) M. Kato. Food & Packaging. 2016, Vol.57, No.8, pp.476-480.
- 4) H. Shirakashi. THE REVIEW OF HIGH PRESSURE SCIENCE AND TECHNOLOGY. 2016, Vol.26, No.4, pp.333-335.
- 5) T. Naoi. Journal of the High Pressure Gas Safety Institute of Japan. 1988, Vol.25, No.6, pp.23-24.

High-pressure Oil-free Screw Compressor

Shugo TAKAKI*1

*1 Rotating Machinery Engineering Department, Rotating Machinery Business Unit, Compressor Division, Machinery Business

Kobe Steel's screw compressors for process gas are widely used in the fields of petrochemistry, general chemistry, oil refining, gas businesses, etc., and, more recently, are being used not only in on-land factories, but also in oceanic platforms and offshore applications such as FPSO. In recent applications that require relatively high discharge pressure, such as flare gas recovery and off-shore VRU, for which small compressors have conventionally been used, medium-sized compressors are needed to respond to the users' requirements for an increased gas flow rate. Now, Kobe Steel has lined up medium sized, high-pressure oil-free screw compressors, whose advantages and concepts are introduced in this paper.

Introduction

Kobe Steel's oil-free screw compressors for process gas are widely used in the fields of petrochemistry, general chemistry, oil refining, gas business, etc.,¹⁾ and more recently, are being used not only in on-land plants, but also in oceanic platforms and offshore applications such as floating production, storage and offloading (FPSO).

Particularly in the cases of flare-gas recovery and offshore vapor recovery units (VRUs), which require relatively high discharge pressure, medium-sized compressors are more and more often needed. This is because these applications, which have conventionally employed small-sized compressors, have recently come to require an increased gas flow rate due to customer demand. In response to such market needs, Kobe Steel has included in its lineup a series of medium-sized oil-free screw compressors for high-pressure specifications. This paper introduces the concept and advantages of these compressors.

1. Applications and applicable range of high-pressure oil-free screw compressors

Fig. 1 shows the range chart of Kobe Steel's compressors. In the cases where oil-free screw compressors are applied with a relatively high required discharge pressure, a multistage compressor of a two- or three-stage arrangement is commonly used. In those cases, a compressor specified for high-pressure is required on the side of the high-pressure stage. In flare-gas recovery, offshore VRUs, etc., a medium-sized compressor

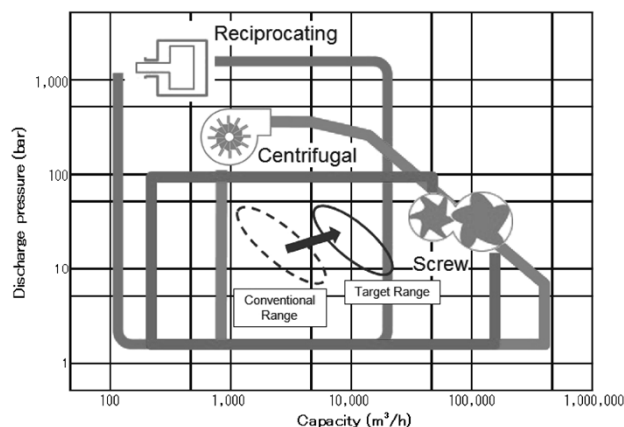


Fig. 1 Range chart for compressors

with a high-pressure and a relatively large capacity is often required. Against this backdrop, Kobe Steel has developed a medium-sized oil-free screw compressor that can cope with a maximum discharge pressure up to 40 barG, whereas the conventional machines could handle only up to approximately 20 barG.

2. Compressor structure

A typical structure of Kobe Steel's oil-free screw compressor is shown in Fig. 2, and the whole system is shown in Fig. 3. The major parts of an oil-free screw compressor include a screw rotor, casing, shaft seal, bearing and timing gear. The design specifications of some major parts such as the rotor, casing, and bearing, have been changed because the load generated by gas compression increases under high-pressure operating conditions. A high-performance silencer has also been developed in order to reduce the acoustic energy, which increases with increasing operating pressure. The following describes the features of each component for the high-pressure oil-free screw compressor.

2.1 Compressor casing

There are two types of casing structures for Kobe Steel's oil-free screw compressors, i.e., a horizontally split type and a cylindrical type, which are selected according to the compressor size. A large-size compressor, used in relatively low-pressure applications, employs a horizontally split type that emphasizes maintainability, whereas, compact to

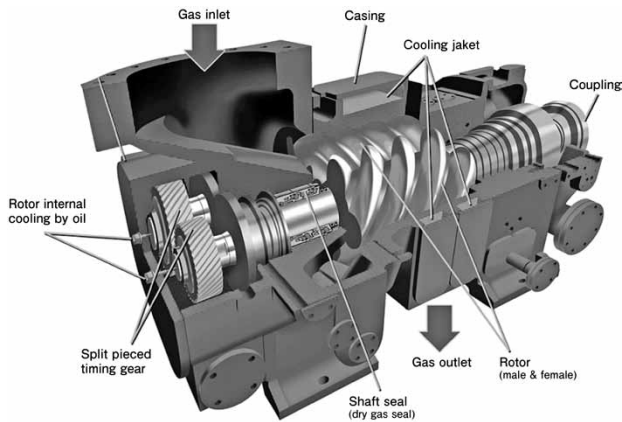


Fig. 2 Structure of oil-free screw compressor

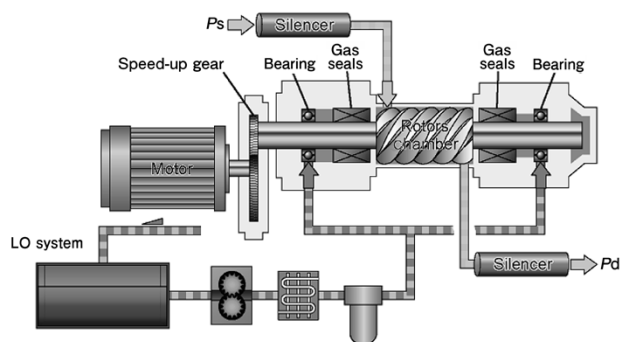


Fig. 3 Typical system of oil-free screw compressor

medium-sized compressors, which are often used in high-pressure conditions, employ cylindrical types with a view to the pressure resistance. For the high-pressure specifications, revisions have been made on the wall thickness and flange rating of the conventional casing.

The standard casings are made of cast carbon steel. For a water injection application, an option is available to improve erosion resistance by overlaying several-millimeter-thick welding of austenitic stainless steel on the inner surface of the rotor chamber of a horizontally split casing. This overlaying welding is a technology established as a result of Kobe Steel's long-standing trial and error efforts. This technology has been used in large-sized screw compressors for styrene monomer applications, in which excellent resistance against erosion has been confirmed.

More recently, casings of cast stainless steel are also being made at customer request.

2.2 Screw rotors

The profile of a screw rotor is an important factor that directly affects the performance of the screw compressor. Hence, Kobe Steel selects, from several types of profiles including proprietary types,²⁾ the optimal rotor profile for the customer's

specifications. The rotor is made of either forged carbon steel or forged stainless steel, depending on the applications or customer's requirements.

The rotor length of each Kobe Steel screw compressor is selected from the short type or the long type on the basis of the specified gas flow rate, so as to enable optimum designing for the compressor capacity. For high-pressure specifications, a shaft with an outer diameter greater than that of the conventional specifications is used to secure the rigidity of the rotor shaft.

2.3 Shaft seal system

The shaft seal system is regarded as one of the most important technologies for process-gas compressors. In the case of Kobe Steel's oil-free screw compressors, an optimum shaft-seal system can be selected from several options in accordance with the specifications, application or customer requirements. The following describes a typical shaft seal system used for Kobe Steel's oil-free screw compressors:

- (1) Dynamic type dry gas seal (tandem or double arrangement)
- (2) Hydrostatic type dry gas seal (single or tandem arrangement)
- (3) Mechanical seal
- (4) Carbon ring seal
- (5) Bearing oil film seal

Dynamic-type dry gas seals or mechanical seals are applicable to high-pressure oil-free screw compressors.

2.4 Bearing (journal bearing, thrust bearing)

Kobe Steel's oil-free screw compressors mainly employ plain bearings. Recently, a lineup of Advanced series, adopting roller bearings, is also available.

Journal bearings are mainly based on cylindrical bearings, in which the positions and shapes of oil grooves, bearing clearance, etc., are optimally designed in accordance with the lubrication conditions and operating conditions. In recent years, tilting-pad journal bearings, having a high vibration-damping effect, are also used for high rotational speed specifications to stabilize the shaft vibration. The high-pressure oil-free screw compressor, however, employs conventionally used cylindrical bearings to support relatively large bearing loads.

The thrust bearing normally adopts a highly reliable tilting-pad bearing on the active load side (Fig. 4). The lubrication type for the thrust bearing adopts the direct lubrication type, which is effective

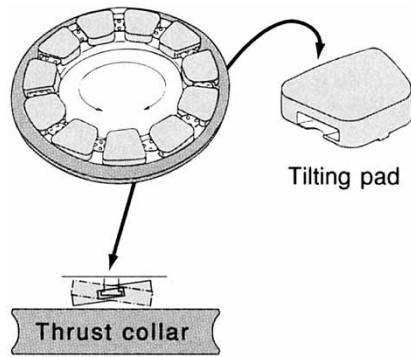


Fig. 4 Tilting pad thrust bearing

in reducing the mechanical loss during high-speed operation. In the cases of high-pressure and relatively high rotational speed conditions, a self-equalizing thrust bearing is occasionally used, due to the high thermal load on the bearings.

2.5 Balance piston

Kobe Steel's oil-flooded screw compressors normally adopt balance pistons to reduce the gas load in the thrust direction. Whereas oil-free screw compressors bear thrust loads that are relatively small and have the problem that the hydraulic oil of balance pistons, if used, generates heat during high-speed operation. Therefore, balance pistons have not been used so far. In high-pressure applications, however, oil-free screw compressors may be operated under conditions where the thrust load is high. Therefore oil-free screw compressors also need to reduce the thrust load by balance piston or some other way, if the allowable thrust-bearing load is exceeded. In general, the mechanisms for reducing thrust load include not only balance pistons, but also the utilization of the meshing reaction force of a single helical gear. Kobe Steel has developed a proprietary balance piston for high-speed operation that can be applied to an oil-free screw compressor.³⁾

2.6 Timing gear

The timing gear of a Kobe Steel's oil-free screw compressor normally has the split structure shown in Fig. 5, which makes it possible to adjust the backlash of the gear. The backlash of the gear, if made smaller than that of the rotors, prevents the rotors from contacting each other at the time of an emergency stop of the compressor, for example, and thereby helps improve the reliability of the compressor.

A high-strength material is selected for the timing gear so as to ensure that its dimension in the axial direction is just enough to secure the necessary

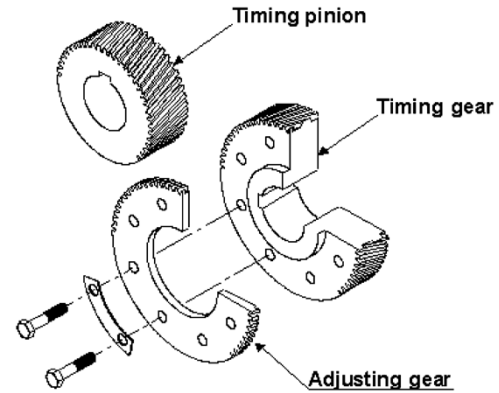


Fig. 5 Exploded view of timing gear

strength without becoming excessively large. As a result, the weight increase of the gear is suppressed, which contributes also to the stability improvement of the rotor during operation. Thanks to the improvement in the machining accuracy of gears in recent years, a precision gear without adjusting gear may be used, especially in cases where high strength is required.

2.7 Water/liquid injection system

In some Kobe Steel's oil-free screw compressors, water or liquid may be injected into the casing, depending on their applications and specifications. For this purpose, a water injection nozzle has been designed such that water is sprayed for easy evaporation. Water is also injected in the direction opposing the gas flow to ensure the homogeneous distribution of water in the process gas. Such water injection methods can significantly reduce the erosion of casings and rotors.

2.8 Silencer

For Kobe Steel's oil-free screw compressors, there are two silencer configurations to reduce acoustic energy in process gas piping, i.e., one silencer installed in the nozzle on the discharge side, and two silencers installed in the nozzles on the suction side and discharge side, respectively. In the case of screw compressors, generally, the acoustic energy on the discharge side is greater than that on the suction side due to the effect of discharge pulsation. Hence, it is important to design measures to reduce the discharge pulsation, especially the low-frequency pulsation. Kobe Steel has technologies to design optimum silencers in accordance with the type of gas and required acoustic characteristics. The company makes the arrangement and optimum design of silencers suitable for the respective applications and specifications.



Fig. 6 Appearance of developed silencer

On the other hand, the pulsation characteristics of a screw compressor may change in flare-gas recovery, which is one of the applications of high-pressure oil-free screw compressors. This is because flare-gas, i.e., the gas accompanying crude oil extraction, may change in composition and concentration over time, depending on the condition of the reserves. This occasionally affects the performance of the silencers.

Hence, in developing high-pressure oil-free screw compressors, Kobe Steel also worked on the development of a silencer that can be used for the above application (Fig. 6).

The newly developed silencer has a reducing effect on the pulsation in a wide frequency band and exerts that effect even when the frequency characteristics of pulsation change as described above. For the development of the silencer, a case study was conducted using acoustic analysis, and the performance was verified by a speaker test using a prototype silencer. In the actual machine test of the high-pressure oil-free screw compressor, as described below, the prototype silencer was installed to verify its performance.

3. Verification by actual machine operation

During the development of the high-pressure oil-free screw compressor, a high-pressure operation by closed-loop was carried out at Kobe Steel's 20 MW test bench (Table 1, Fig. 7, Fig. 8). The discharge pressure was raised to the maximum 40 barG to verify the mechanical stability of the compressor under high-pressure conditions. The following items were also checked:

- (1) The performance of the compressor was confirmed by operating with gases having different molecular weights.
- (2) The bearing temperature, the shaft vibration, etc., at the maximum load operation, were confirmed to be within the allowable limits

Table 1 Specifications and test conditions of developed compressor

Model	KS40SNZ
Test gas media	N ₂ , CO ₂
Discharge pressure (barG)	Max. 40
Rotational speed (rpm)	Max. 4,700
Suction volume (m ³ /h)	Max. 10,000

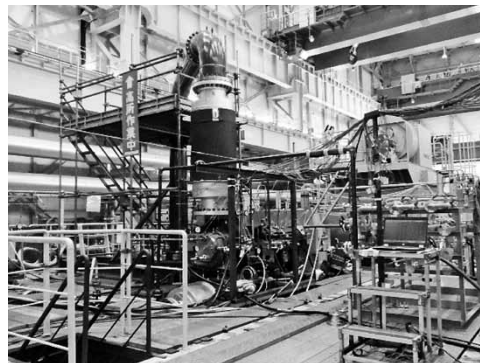


Fig. 7 View of test bench

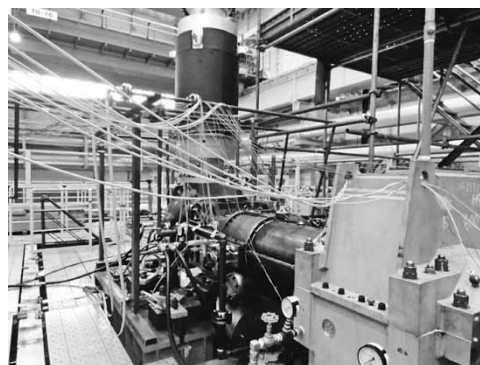


Fig. 8 Prototype model of developed high-pressure screw compressor

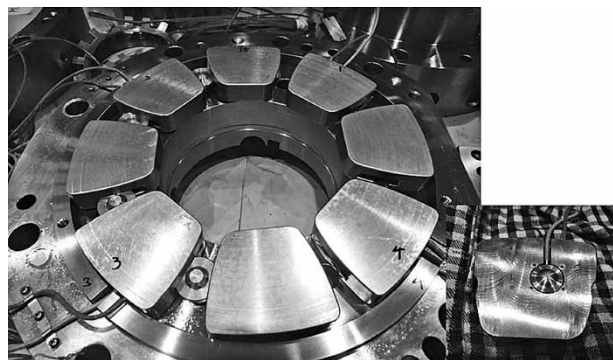


Fig. 9 Thrust bearing with embedded load cell

specified by Kobe Steel's design standard and the API standard.

- (3) The load acting on the thrust bearing was monitored by a load cell embedded in the thrust bearing pad (Fig. 9).
- (4) The change value of the thrust load with the use of the balance piston was checked

to confirm that the balance piston was functioning normally.

- (5) The sound pressure inside the silencer was measured to confirm that the acoustic energy in the silencer was reduced.
- (6) Disassembly inspections after high pressure operation confirmed that there were no abnormalities in the internal parts of the compressor.

4. Future perspectives

Kobe Steel is capable of designing not only the oil-free screw compressor for high-pressure specifications, introduced in this paper, but also oil-free screw compressors for high-speed specifications and for high/low temperature applications.

The company not only supplies customers with bare screw compressors, but also with compressor units as shown in Fig.10.

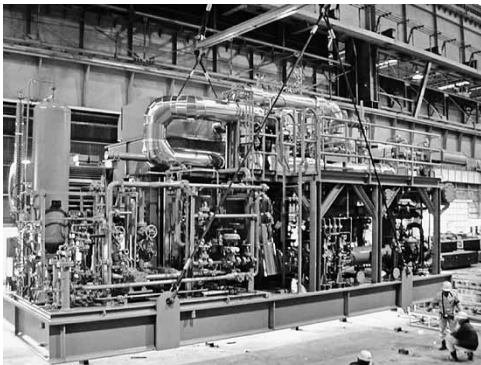


Fig.10 Oil-free screw compressor unit

Kobe Steel will continue to produce cutting-edge screw compressors in accordance with the market needs.

Conclusions

Kobe Steel has designed and manufactured oil-free screw compressors for more than 60 years and has many deliveries on record. Exploiting the experience it has gained so far, the company will continue to expand the scope of its oil-free screw compressors by developing new technologies and new models that are adapted to market needs, as well as improving existing models. In addition, it will focus on developing new fields and new applications and thus contribute to the development of the industry through its oil-free screw compressors.

References

- 1) S. Takaki et al. R&D Kobe Steel Engineering Reports. 2009, Vol.59, No.3, p.21.
- 2) E. Fujita et al. R&D Kobe Steel Engineering Reports. 1999, Vol.49, No.1, p.36.
- 3) Kobe Steel, Ltd. COMPRESSOR. Japanese Patent No. 6019003. 2 Nov. 2016.

Large Integrally-gear Centrifugal Compressor

Keiichi SAEKI*1, Yasuhisa YAMASHIRO*1, Toshihisa SHIBATA*2, Atsushi SANO*2

*1 Rotating Machinery Engineering Department, Rotating Machinery Business Unit, Compressor Division, Machinery Business

*2 SHINKO TECHNO ENGINEERING CO., LTD

A newly developed centrifugal compressor has a large capacity and incorporates a gear unit. An attempt was made to downsize the compressor, and the cost has been reduced by revising the procurement method of the gear unit, etc. A full load test has been carried out on a prototype machine in the company's proprietary facility to confirm its performance and mechanical stability. As a result of this development, the application range of integrally-gear centrifugal compressors has been doubled, enabling a response to the demands of the expanding market.

Introduction

Integrally-gear centrifugal compressors are being increasingly used, thanks to their energy-saving and space-saving features. In recent years, the demand for compressors with greater capacity has been increasing as plants become larger.

So far, Kobe Steel has delivered integrally-gear centrifugal compressors with processing flow rates up to approximately 160,000 Nm³/h. On the basis of these achievements and with the aim of greatly expanding their applicability, the company has recently developed an integrally-gear centrifugal compressor that meets the market needs for a greater processing flow rate of up to 400,000 Nm³/h. **Fig. 1** shows the standard range chart of Kobe Steel products.

A large prototype compressor was built, and

operational demonstration testing was conducted under actual load conditions. This paper reports the outline.

1. Construction of prototype compressor

An integrally-gear centrifugal compressor comprises a speed-increasing gear device having a pinion shaft, at least one end of which is overhung for attaching at least one impeller. Increasing capacity accompanies the upsizing of the impellers and whole compressor, exerting a significant influence on the footprint area, etc.

This prototype compressor has achieved downsizing with, among other things, a newly developed high-specific-speed impeller designed to minimize the increase in compressor size associated with an increased process volume. In addition, a cost reduction plan was adopted, which included changing the method of procuring principal components such as the large speed-increasing device.

First, an operational test was carried out using a prototype three-stage compressor (model: VG 683) with a processing flow rate of approximately 300,000 Nm³/h, to confirm the mechanical stability and power performance of the compressor. Then, the prototype machine was modified to establish a design guideline for further upsizing, and an operation test was carried out with a single-stage

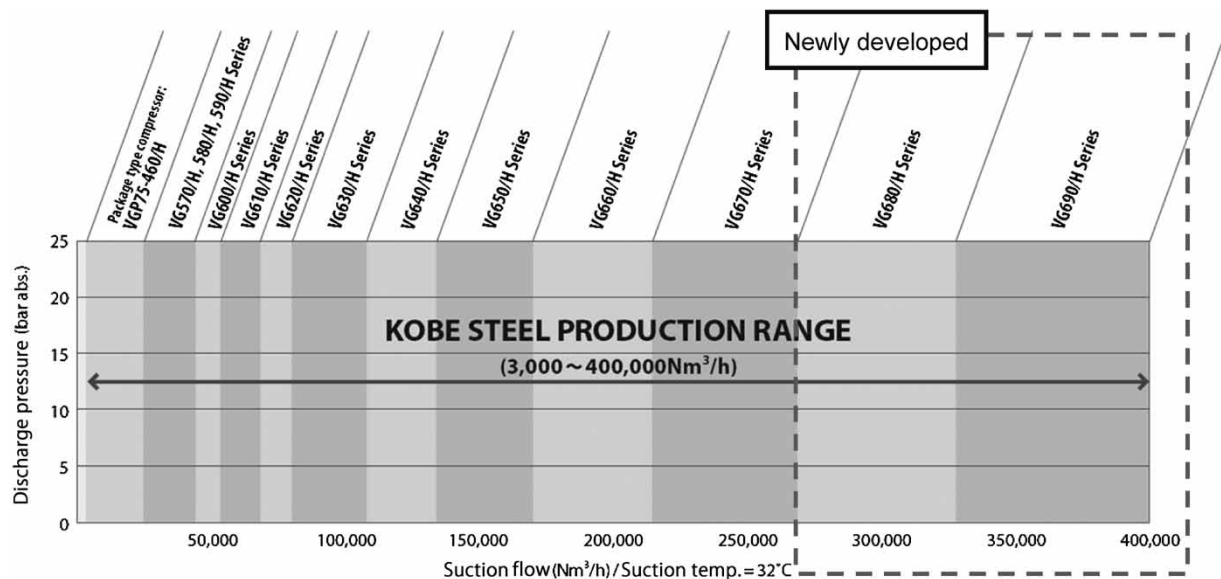


Fig. 1 Standard range chart

machine (model: VG691), which comprises a one-stage impeller having the maximum diameter for a hypothetical model with a processing flow rate of approximately 400,000 Nm³/h. The appearance, cut model, and specification of the prototype compressor (VG 683) are shown in Fig. 2, Fig. 3, and Table 1, respectively.

1.1 Impeller / casing

A newly developed high-specific-speed impeller was adopted for the downsizing of the compressor. This allowed a 20 to 25% reduction of the impeller, as compared with that of the conventional design guideline. Fig. 4 compares the meridian shapes of the conventional impeller and new impeller. As for the scroll casing, its cross-sectional distribution

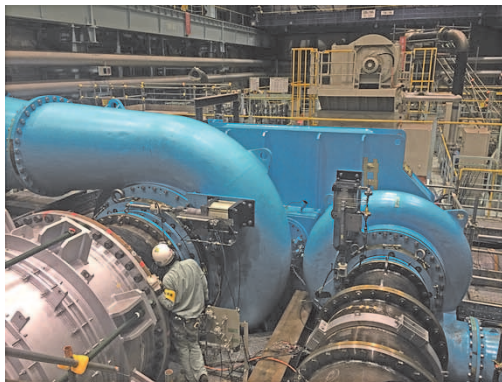


Fig. 2 Appearance of newly developed compressor (VG683)

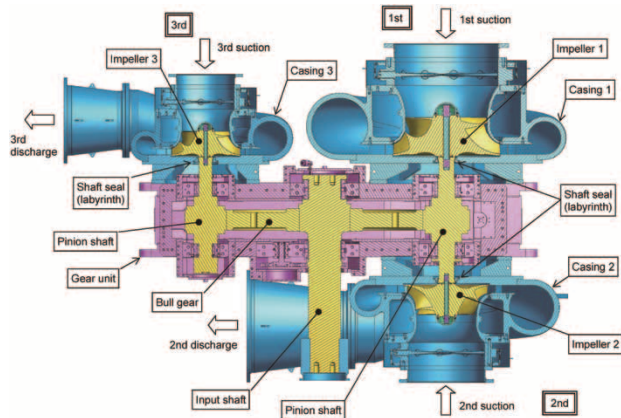


Fig. 3 Cut model of prototype compressor (VG683)

Table 1 Specifications of prototype compressor

Type	VG683	VG691 ^{*1}
Application	Main air compressor	← (same as VG683)
Gas	Wet air	← (same as VG683)
Number of stage	3	1 ^{*1}
Standard flow	300,000 Nm ³ /h	400,000 Nm ³ /h
Suction pressure	-1.5 kPaG	-1.5 kPaG
Discharge pressure	0.49 MPaG	0.12 MPaG ^{*1}
Rotating speed (pinion shaft)	1st piston: 4,992 rpm 2nd piston: 5,673 rpm	Pinion: 4,357 rpm
BHP	23,000 kW	approx. 14,500 kW
Shaft seal	Labrynth seal (step seal)	← (same as VG683)

^{*1} Single stage compressor as prototype for VG690 series (modified from VG683)

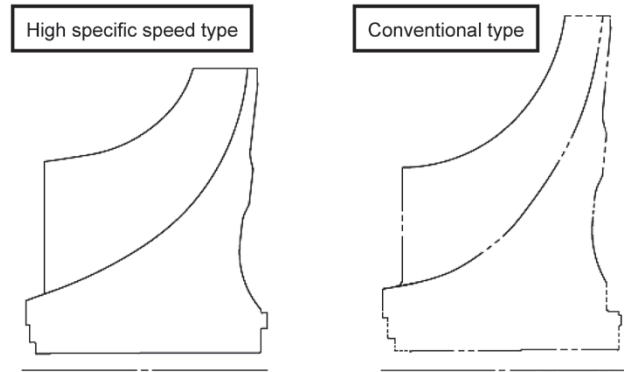


Fig. 4 Comparison of meridian section shapes of impellers

of the flow passages was optimized for the large capacity machine, which led to a weight reduction of approximately 10% compared with that of the product based on the conventional Kobe Steel design.

These efforts have suppressed the size and weight of the compressor body while improving the workability of the assembly.

1.2 Speed-increasing device

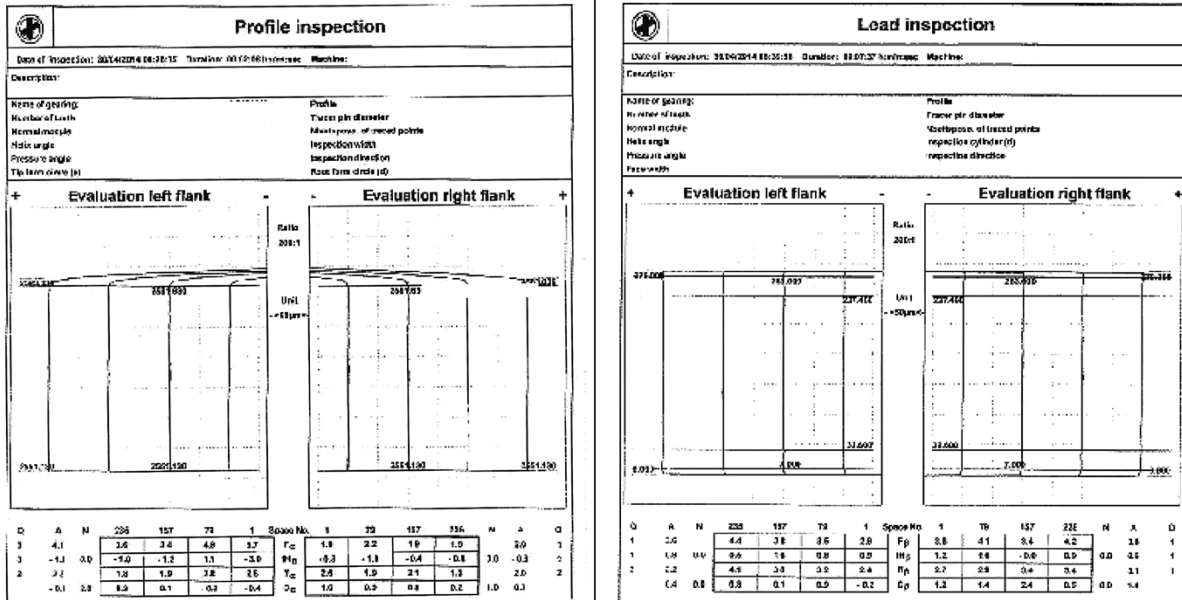
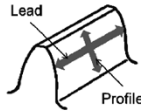
The speed-increasing device is one of the principal components of the compressor, and a gear with a large diameter of ϕ 2,500 to 3,100 mm is required for the target specification range of this development. Such a large speed-increasing device for high speed operation requires high quality and can only be fabricated by a limited number of manufacturers.

Hence, a supplier having equipment capable of manufacturing large diameter gears has been selected to expand Kobe Steel's previous policy of in-company designing and outsourced-processing, the policy for the small-to-medium sized speed-increasing device. Furthermore, the prototyping and demonstration testing of large diameter gears was carried out while studies were repeated to optimize the processing conditions of the equipment.

Among the standards for the design and production of centrifugal compressors, the American Petroleum Institute (API) standard^{1), 2)} is widely recognized and applied globally. As shown in Fig. 5, the gear flank tolerance satisfies the gear accuracy requirements specified by the API standard, ISO 1328 Grade 4.³⁾ Moreover, as shown in Fig. 6, the static tooth contact between the bull gear and pinion gears was also confirmed to satisfy the standard required by API.

1.3 Other accessories

The shaft seal device employs a step-type



Satisfied: ISO1328 Grade 4

Fig. 5 Gear flank tolerances

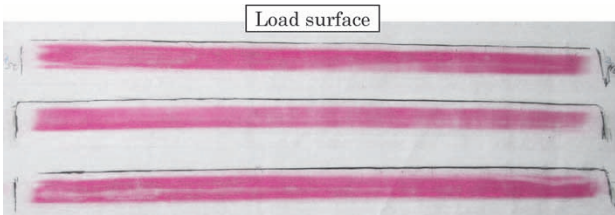


Fig. 6 Static gear contact result

2. Operational test

2.1 Operational test results for speed-increasing device alone

The peripheral speeds of gears were specified to exceed Kobe Steel's conventional standard design criteria. Hence, an operational test was carried out on the speed-increasing device alone, and it was confirmed that both its vibration and bearing-temperature characteristics were favorable, without any problems. Fig. 7 shows the measurement results for the speed-increasing device operating alone. The mechanical loss was also measured using a torque meter to verify Kobe Steel's method of loss calculation for large high-speed gears.

2.2 Actual-load test of compressor

Following the operational test on the speed-increasing device alone, an actual-load test of the compressor was carried out using the company's proprietary test-run apparatus to confirm its mechanical stability and to evaluate the power performance.

2.2.1 Mechanical stability

Table 2 shows the measurement results for the bearing temperature and bearing vibration during

labyrinth seal, which is simple and capable of suppressing leakage loss.

The rotating shaft of a compressor receives the thrust load caused by gas and the thrust load caused by the meshing of gears, as well. Adopting rider rings in large compressors can cause a problem in that the axial movement of the pinion shaft becomes excessive, due to the inclination of the bull gear in the speed increasing device. In order to avoid this, a method of individually mounting a thrust bearing on each pinion shaft was adopted to improve the reliability of the machine. In addition, assuming a turbine drive and to reduce resistance torque at the start-up, a hydrostatic bearing was used for the journal bearing of the low-speed shaft to ensure reliability at low speed operation, and the effect was verified.

As for the intermediate cooler, which accounts for a large proportion of the cost of the peripheral devices of compressors, a new vendor was selected, and their quality and capability were confirmed.

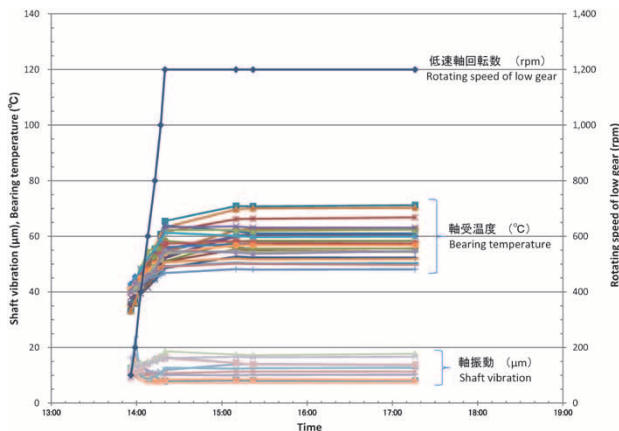


Fig. 7 Test operation results for speed-increasing device alone

Table 2 Records of running test

KOBELCO						
RECORDS OF SHOP RUNNING TEST						
Mechanical Running Test of Centrifugal Compressor						
Model VG683						
Item	Time Unit	11:50	12:15	12:52	13:40	14:30
		BEARING TEMPERATURE				
High speed, 1st stage	°C	69.7	70.3	71.8	72.3	72.0
High speed, 2nd stage	°C	79.1	80.2	80.9	81.1	79.5
Thrust1-2, sideA	°C	51.8	52.0	52.5	52.8	52.7
Thrust1-2, sideB	°C	65.6	64.2	63.7	63.7	62.7
High speed, 3rd stage	°C	79.4	79.8	80.7	81.3	81.2
High speed, Anti-3rd stage	°C	66.2	65.6	67.0	67.2	66.7
Thrust3, sideA	°C	77.5	71.6	78.5	79.6	80.3
Thrust3, sideB	°C	58.1	58.3	58.6	58.4	58.4
SHAFT VIBRATION						
H. pinion, 1st stage	μ	21.74	21.23	20.05	20.09	19.64
V. " " "	μ	20.82	21.76	19.87	19.23	19.11
H. pinion, 2nd stage	μ	17.24	16.71	16.50	16.29	16.21
V. " " "	μ	19.24	18.82	18.95	18.47	18.12
H. pinion, 3rd stage	μ	16.26	16.26	16.43	16.36	15.70
V. " " "	μ	14.38	14.28	14.52	14.08	13.87
H. pinion, Anti-3rd stage	μ	14.67	14.67	15.11	15.62	15.39
V. " " "	μ	10.91	10.50	10.95	11.07	11.13

the actual load test of the compressor. The bearing temperature was within approximately 80°C for all the bearings, confirming that there are sufficient margins against the Kobe Steel's criteria values. Also, the shaft vibration was within approximately 20 μm (p-p) for the compressor in fully-loaded conditions, and the results were favorable, satisfying the requirements of the API standard.

The above results confirm that the prototype compressor has sufficient mechanical stability. Also, through disassembly and inspection after operation, such parts as the impeller, shaft-seal device, and bearings, as well as the dynamic tooth contact of the speed-increasing device were checked to confirm that they are all satisfactory.

2.2.2 Power performance

The API standard cites ASME PTC-10 (Performance Test Code on Compressors and Exhausters)⁴⁾ as a method of evaluating the performance of the compressor. The power performance of the compressor was confirmed on

the basis of this test standard.

The results of the power performance measurement indicate that the polytropic efficiency is improved by 1.5 to 2.0 points over that of the conventional Kobe Steel impellers. The working performance of the new impeller with a large diameter for high specific speed has been confirmed to achieve the target efficiency.

2.2.3 Ancillary equipment

Through the prototyping, the intermediate cooler has been confirmed to have sufficient quality. Furthermore, in terms of capacity, the upper limit value for the increase of cooling water temperature was successfully raised, and it was confirmed that the water consumption could be reduced. The future plan includes efficiency improvement through optimizing the internal fin shape and further cost reduction.

Conclusions

An integrally-gear centrifugal compressor for applications ranging from 300,000 to 400,000 Nm³/h has been developed, and its manufacturability and compressor performance have been demonstrated. In addition, the applicability of integrally-gear centrifugal compressors, which excel in space saving and energy-saving performance, has been greatly expanded.

Customers, including manufacturers of air-separation-units, engineering companies, and end users, witnessed the actual load tests through which Kobe Steel's capacity for producing large machines has been confirmed. It should be noted that the prototype compressor was subsequently delivered to a customer and has been running smoothly to date.

In the future, a newly introduced 40-MW test-run apparatus will be used to further expand the applicability of integrally-gear centrifugal compressors. Kobe Steel will also strive to develop element technologies and products, taking into consideration the fields of higher pressure, such as carbon dioxide storage applications.

References

- 1) API STANDARD 617 EIGHTH EDITION, SEPTEMBER 2014.
- 2) API STANDARD 672 FOURTH EDITION, MARCH 2004.
- 3) ISO 1328-1 CYLINDRICAL GEARS - ISO SYSTEM OF ACCURACY.
- 4) ASME Performance Test Codes (PTCs) 10-1997.

Vertical Type Reciprocating Compressor for LNG Boil Off Gas (BOG) Injection

Katsuhiro SEYAMA*1, Satoshi TEZUKA*1, Takashi OKUNO*1, Kenji NAGURA*1, Naoki AKAMO*1

*1 Rotating Machinery Engineering Department, Rotating Machinery Business Unit, Compressor Division, Machinery Business

As the shipbuilding industry is enforcing environmental regulations, low-speed dual-fuel engines, such as ME-GI, are attracting rising attention. Such an engine requires a gas-injection compressor (GIC) to supply LNG boil off gas (BOG), and the demand for GICs is expected to grow. Hence, KOBE Steel has developed a vertical type LNG BOG reciprocating compressor suitable for GIC for ME-GI engines. In developing the compressor, we have utilized proven technologies, such as low temperature suction, high pressure discharge, and a high-performance oil-separation system. A vertical type suited to the installation space on a ship has been adopted, and ease of maintenance has been ensured. This paper describes its development.

Introduction

The environmental regulations set by the International Maritime Organization (IMO) were strengthened. As a result, new low-speed, dual-fuel engines fueled by heavy oil and natural gas for direct propulsion are attracting attention in the shipping industry; they have begun to be adopted on LNG carriers. In the case of a low-speed, dual-fuel, electronically controlled, gas-injection diesel engine (hereinafter referred to as an "ME-GI engine"¹⁾, fuel must be supplied into its combustion chamber at a pressure as high as approximately 30 MPa; hence, a gas-injection compressor (hereinafter referred to as a "GIC") is required to pressurize the gas.

There also is a prospect that more than 150 LNG carriers will be newly constructed between 2017 and 2021,²⁾ and the demand for compressors for LNG carriers is expected to grow correspondingly. Hence, Kobe Steel has been promoting the development of compressors for ships to expand the applications in the compressor business. This paper describes the product development of GICs for ME-GI engines.

1. Gas supply system for LNG carrier equipped with ME-GI engine

Fig. 1 shows a gas supply system for an LNG carrier equipped with an ME-GI engine. The amount of boil-off gas (hereinafter referred to as "BOG") generated from an LNG tank varies depending on the capacity and thermal insulation performance of the tank and usually falls in the range of approximately 3.0 to 5.0 t/h. The generated BOG is

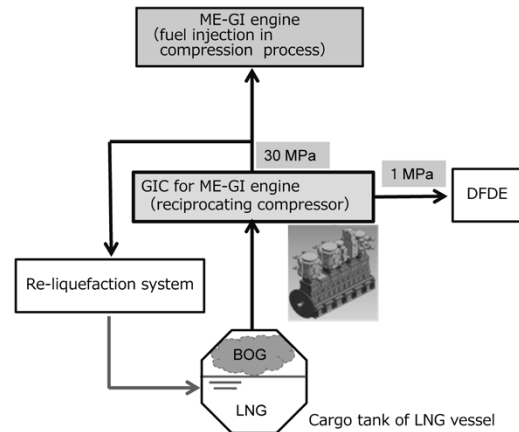


Fig. 1 Gas supply unit of ME-GI engine for LNG carrier

pressurized up to 30 MPa and supplied to the ME-GI engine for propelling the LNG carrier, with a portion of the gas being pressurized up to about 1 MPa to be supplied to a dual-fuel diesel engine (DFDE)³⁾ to power the on-board auxiliary machinery.

A carrier may be equipped with a re-liquefaction unit for collecting and liquefying surplus BOG and returning it to the tank when the fuel gas consumption of the engine is less than the amount of BOG generated from the LNG tank, or when the carrier is stopped. The efficiency of such a re-liquefaction unit increases as the pressure of the supplied gas increases. When a re-liquefaction unit is installed with an ME-GI engine, BOG at a pressure of approximately 30 MPa is supplied to the re-liquefaction unit. This increases the efficiency of re-liquefaction, improves the fuel efficiency and demonstrates excellent economy.

A compressor unit for supplying BOG to an ME-GI engine must be reasonably compact, since it is installed in a limited space onboard. The unit also is required to be capable of directly suctioning BOG at about -160°C and raising it from atmospheric pressure to 30 MPa. Thus, various other technologies are also required: e.g., a technology to extract gas from an intermediate portion and a technology to efficiently respond to the amount generated and to the amount of BOG supplied, the amounts changing depending on the engine load. The re-liquefaction unit requires an oil-separation unit for supplying gas with the oil appropriately removed.

The following describes the features of a reciprocating compressor, which Kobe Steel developed for ME-GI engines.

2. Compressors for ME-GI engines

2.1 Compressor specifications (vertical compressor)

Kobe Steel has delivered a number of high-pressure LNG BOG compressors to LNG-receiving terminals. They adopt vertical GICs while exploiting the technologies for producing high-pressure gas from the low-temperature BOG.

Each GIC consists of a 5-stage compressor for pressurization up to 30 MPa and includes an intermediate portion at the second stage to extract the gas for a DFDE. The compressor unit comprises a BOG compressor, a main electric motor, a gas cooler, an interconnect piping between the stages, an oil supplying device, and a drum for preventing pulsation, all mounted on a common skid. The dimensions of the unit for a process volume of 5 t/h is 7 m x 10 m x 6.5 m. **Table 1** compares the size (including the maintenance space) of vertical and horizontal compressor units with equivalent function and performance.

In general, a vertical compressor tends to be subjected to an unbalanced force caused by the reciprocation of pistons, a force greater than that experienced by a horizontal compressor. In a vertical machine with a crankshaft with 6 throws, the unbalanced force can be cancelled out by a 120° angular phase shift between each pair of throws, i.e., (i) #1 & #6 throws, (ii) #2 & #5 throws, and (iii) #3 & #4 throws. This concept has been adapted for the 5-stage compressor for ME-GI engines, in which a balancing throw without a cylinder is provided to maintain the balance of the compressor and minimize the unbalanced force exerted on the foundation on the ship.

Another advantage of vertical compressors exists in their rider rings. In the case of a reciprocating compressor with piston rings, rider rings are provided to prevent each piston from contacting the corresponding cylinder liner during the reciprocating motion of the piston.

Unlike the case of horizontal machines, rider rings in a vertical compressor need not support the weight of the pistons and wear significantly less.

Table 1 Unit size of vertical- and horizontal-type compressors (including maintenance space)

Compressor type	Vertical type	Horizontal type
Width (m)	7	10
Length (m)	10	10
Height (m)	6.5	5
Foot print [W×L] (m ²)	70	100

For this reason, the replacement frequency of rider rings can be greatly reduced compared with that for a horizontal machine. There is also no damage, such as seizure, due to the contact between a piston and cylinder liner, which improves not only the economic efficiency but also the reliability.

2.2 Gas volume control

The suction gas temperature of a compressor can be cryogenic (approximately -160°C) when the BOG generated in an LNG tank is directly suctioned, or the temperature can rise to near room temperature when the gas is re-liquefied utilizing the cold energy of the suction gas. When a compressor that has been shut down for a long period of time is restarted, room temperature gas is suctioned immediately after the restart, and the temperature lowers with the passage of time.

Such a significant change in the suction gas temperature changes the amount of gas processed by each cylinder of the corresponding stage and also affects the pressure balance. These are phenomena characteristic of low-temperature compressors. In addition, as described above, the balance between the amount of BOG generated from the LNG tank and the amount of gas being consumed by the engine changes constantly, and the operation conditions of the compressor change at the same time. Stable operation in such an environment calls for various measures including control methods and appropriate design margins. In this regard, Kobe Steel fully exploits its technology backed up by its abundant operational experiences with low-temperature compressors for LNG-receiving terminals. In addition, the GIC is provided with a volume adjustment device including a suction-valve unloader and a clearance pocket, while each stage is provided with a spillback line, so as to cope with any rapid fluctuations of the engine load.

2.3 Oil separation unit

Fig. 2 depicts a flow diagram of a GIC system for an ME-GI engine. The BOG generated from an LNG tank is pressurized to 30 MPa by the compressors and supplied to the engine. Each compressor includes plastic sliding parts, such as piston rings, rider rings, and piston-seal packings. In order to ensure their durability and reliability, lubrication oil is supplied inside the cylinder of the high-pressure stage. This has enabled long-term continuous operation.

Meanwhile, the oil contamination in the gas supplied to an ME-GI engine must be minimized. To

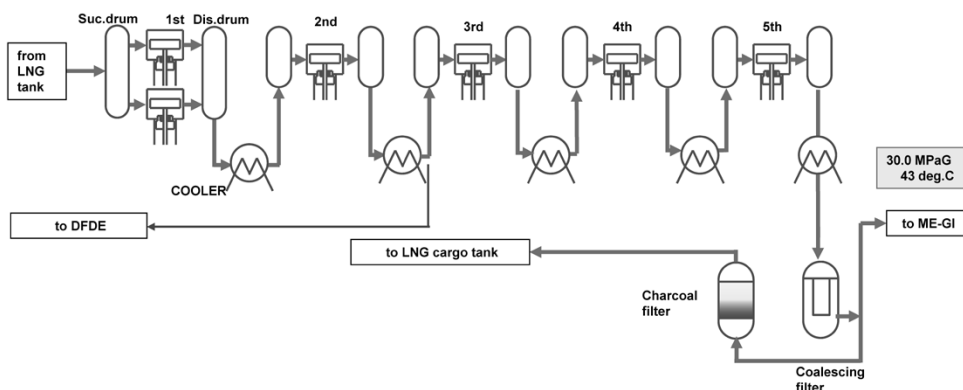


Fig. 2 ME-GI GIC flow diagram

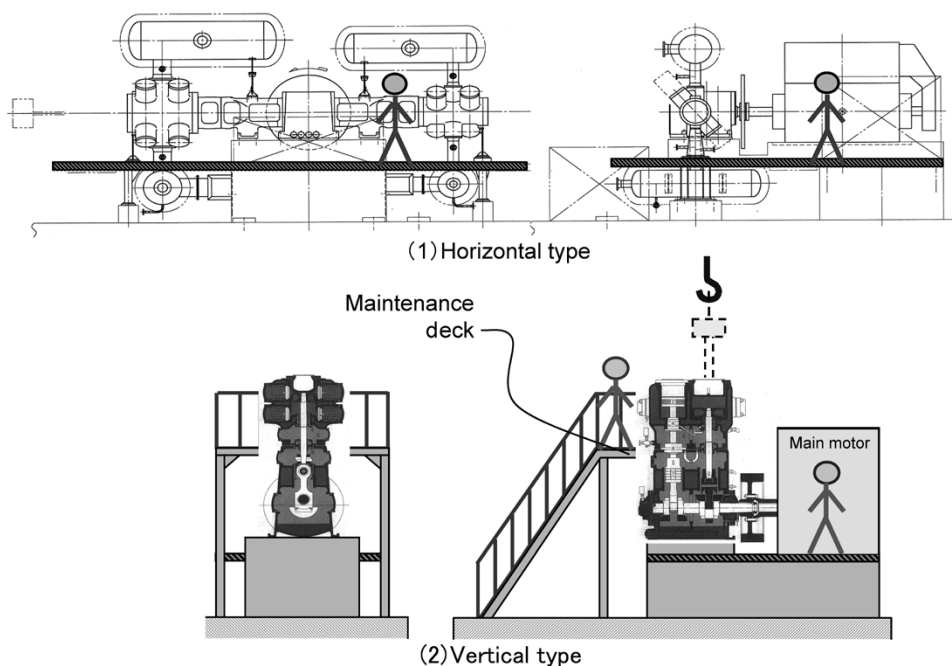


Fig. 3 Horizontal- and vertical-type reciprocating compressor units

this end, a high-performance filter for oil separation is installed in the downstream of the compressor exit to remove the lubricant oil contained in the gas.

Furthermore, in the case where a re-liquefaction unit is installed, the gas supplied at a high pressure rapidly expands, liquefying the oil dissolved in the gas. The oil content must also be removed. Hence, this system has an additional activated carbon filter in the downstream of the above-described high performance filter to further strengthen the oil removal performance.

Kobe Steel has introduced an advanced oil-separation unit as described above and has delivered a number of oil-flooded screw compressors, each involving a large amount of oil flooded during the compression process, for applications such as LNG-receiving terminals and helium liquefaction apparatuses, applications requiring processing without oil contamination. All these oil-flooded screw compressors are operating without any

problems.

The compressors for ME-GI engines also exploit these technologies to suppress the influence of oil on the engine and re-liquefaction unit. Maximum consideration was given so as not to deteriorate the durability or the reliability of the sliding parts of the compressors.

2.4 Maintainability (maintenance requiring 24 hours or less)

Fig. 3 shows the reciprocating compressors of the horizontal type and vertical type. A horizontal-type compressor comprises a crank case and cylinder that are fixed to the foundation and is less likely to cause vibration. However, it has a drawback: a large installation area must be secured, including a space for pulling out the pistons in the horizontal direction during maintenance.

A vertical-type compressor, on the other hand,

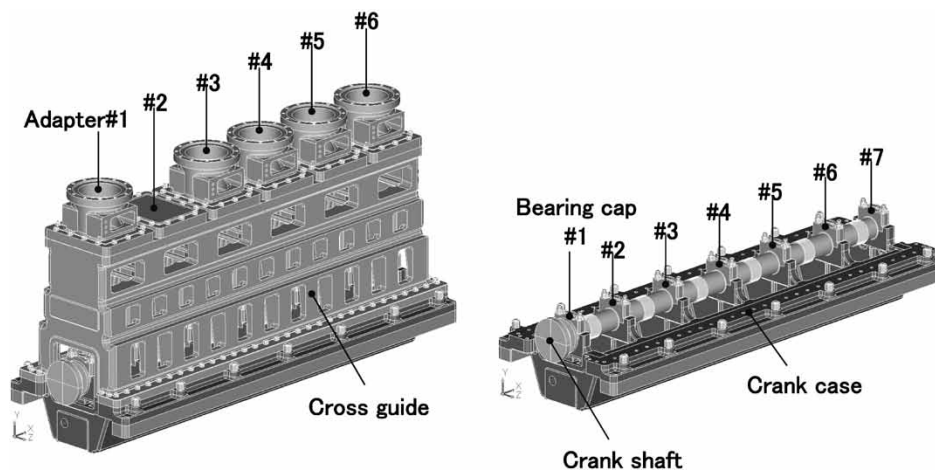


Fig. 4 3D-CAD model for FE analysis

only requires installation space for the crank case, and the installation area can be small. In addition, each piston is pulled out in the vertical direction during maintenance, so it therefore has the advantage of effectively utilizing the limited space on board and allowing, for example, the installation of other apparatuses adjacent to the compressor unit.

Maintenance work on compressors is presumed to be conducted while the ship is in dock. For any maintenance that should be performed on board, a structure that allows the replacement of a cylinder and piston as a set was adopted so as to recover the compressor during a short period of time in the berth. In other words, the structure allows a cylinder to be separated from the cross guide with a piston inserted in it. Short-term maintenance could not be realized with the conventional method, which requires the separate tasks of removing cylinder valves, the main expendable parts of a reciprocating compressor, from the cylinders, removing replacement parts such as piston rings, rider rings, piston-seal packings after pulling out the pistons, and so on. The newly developed compressor system has a structure that allows collective replacement, by means of which the maintenance work period for all the cylinders is expected to be shortened to approximately 24 hours.

2.5 Verification using prototype machine

In this development, a three-dimensional analysis model combining the principal components of a compressor, including the crank case, was prepared to ensure strength reliability; and a stress analysis by the finite element method (FEM) was carried out under the analysis conditions based on operating states, including the actual gas pressure during operation and the inertia force (i.e., load generated by the reciprocating motion of pistons, etc.) The

amount of deformation and strength were confirmed for each principal component.³⁾ Fig. 4 shows the 3-D CAD model used for the analysis.

In addition, a load test using a prototype machine was conducted to quantify the stress generated in each principal component and to verify whether sufficient rigidity was secured. The natural frequency of the compressor was also confirmed by the analysis. It was measured using the prototype machine (a compressor having the size of the actual machine), and the vibration phenomena with changing RPM were confirmed to make sure that the natural frequencies of the compressor and the RPM component do not coincide (or resonate).

2.6 Class authentication

Vessel equipment can be mounted on ships only after authentication by ship classification societies. A compressor cannot be installed on a ship unless it is approved by the classification organization and has passed the inspections required for class certification.

To develop a compressor to be installed on a ship, a type approval was obtained from a classification agency, DNV-GL, in June 2016. Fig. 5 shows the certificate.

3. Other applications related to LNG carriers

An X-DF⁴⁾ engine is another type of low-speed dual-fuel engine of a new direct propulsion system adapted for LNG carriers. From the aspect of compressor specifications, the pressure of the BOG to be supplied to this engine is about 2 MPa: the main feature of the engine is a pressure lower than that for ME-GI engines, while its other characteristics, such as processing volume, are almost the same. It should be noted,

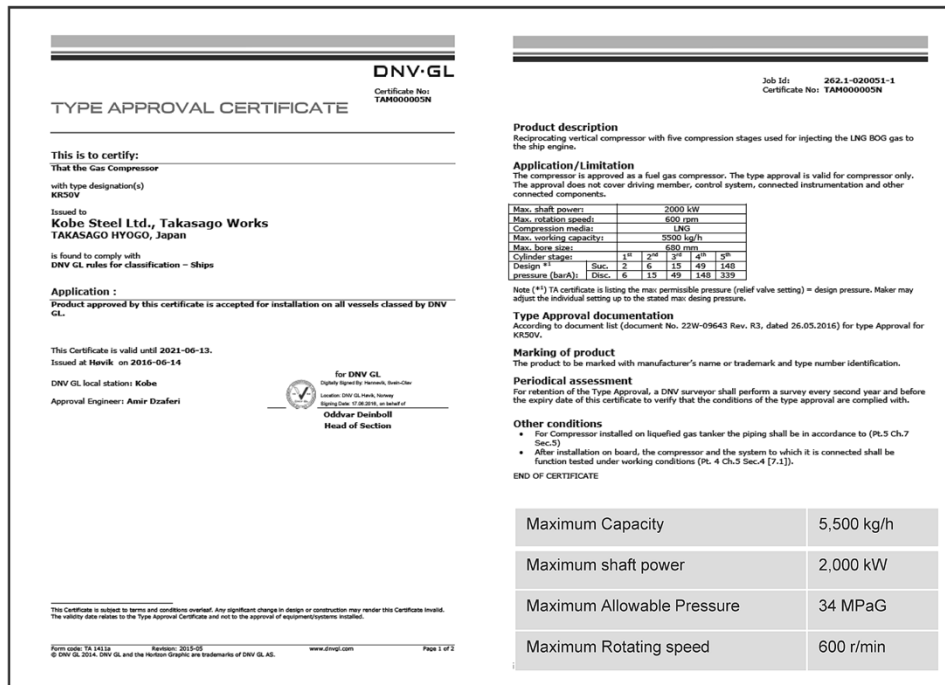


Fig. 5 Type approval certificate from DNV-GL

however, that the pressure of 2 MPa is not high enough to re-liquefy BOG, and there also is a need for a compressor to perform re-liquefaction in addition to GICs. Many of the requirements for these compressors are held in common with the compressor for the ME-GI engine, mentioned above. Fig. 6 is the overview of the fuel supply system for an X-DF engine. In this case, a system combining a Kobe Steel's screw compressor for GIC and a reciprocating compressor for re-liquefaction was adopted, and the company received the order for the first machine in 2016.

As in the case of the gas supply system for an ME-GI engine, this gas supply system for an X-DF engine is also required to have a compressor control system that ensures a stable fuel supply and optimum re-liquefaction for the amount of BOG generated and for a load that varies with the load of the engine. The system, which couples the screw compressor and reciprocating compressor to control the flow rate, could only be developed with Kobe Steel's unique technology and know-how that work on both types of compressors.

Conclusions

Under increasingly stringent environmental regulations, LNG carriers are inclined to employ new propulsion engines using natural gas as their fuel. Kobe Steel has developed a vertical reciprocating compressor used for the fuel

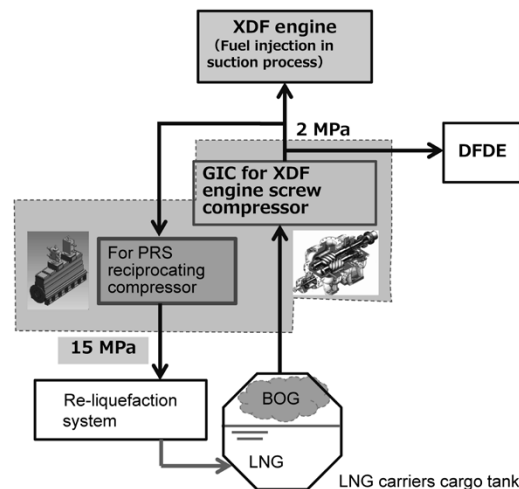


Fig. 6 Gas supply system for X-DF engine of LNG carrier

supply system of these new propulsion engines. In developing this compressor, the company's proprietary technologies, involving low temperature, high-pressure oil separation, are used to realize improved maintainability. In addition, the company has received an order for the compressor for a re-liquefaction unit attached to the fuel supply system and are building a control system combined with the screw compressor for GIC.

Kobe Steel will strive to further refine these compressor units, continue development so as to respond flexibly to the need for compressors required for the various gas supply systems of ships, and contribute to the field of LNG carriers.

References

- 1) MAN Diesel SE. LNG Carrier Power: Total Fuel Flexibility & Maintainability with 51/60DF Electric Propulsion. <http://marine.man.eu/docs/librariesprovider6/technical-papers/lng-carrier-power> (reference made on 2017-07-07).
- 2) Douglas Westwood. DW Monday: A Sea Change In LNG. 19th September 2016. <http://www.douglas-westwood.com/dw-monday-a-sea-change-in-lng/>, (reference made on 2017-07-07).
- 3) N. AKAMO. R&D Kobe Steel Engineering Reports. 2009, Vol. 59, No. 3, p. 55.
- 4) Marcel Ott. WinGD, 2015-09-08, X-DF dual-fuel engines -Technology Review/Marcel Ott. https://www.wingd.com/media/1445/marcelott_x-df_technology-review.pdf, (reference made on 2017-07-07).